Detailed Results of Monte Carlo Simulation of Neoclassical Transport in Stellarators

W. DOMMASCHK
W. LOTZ
J. NÜHRENBERG

IPP 0/48 May 1984

MAX-PLANCK-INSTITUT FÜR PLASMAPHYSIK
8046 GARCHING BEI MÜNCHEN

MAX-PLANCK-INSTITUT FÜR PLASMAPHYSIK

GARCHING BEI MÜNCHEN

Detailed Results of Monte Carlo Simulation of Neoclassical Transport in Stellarators

W. DOMMASCHK
W. LOTZ
J. NÜHRENBERG

IPP 0/48 May 1984

IPP 0/48 May 1984

Detailed Results of Monte Carlo Simulation of Neoclassical Transport in Stellarators

W. DOMMASCHK
W. LOTZ
J. NÜHRENBERG

Abstract.

Neoclassical transport coefficients are computed by Monte Carlo simulation over a wide range of mean free paths in the approximation of small gyroradius, monoenergetic particle distribution, and vanishing electric field for several stellarator fields. Pfirsch-Schlüter, plateau, and ripple transport coefficients are obtained. The transport coefficients for $\ell = 2$ stellarators in the ripple regime can be described as a single function of the aspect ratio, the rotational transform, and the number of periods. We present here stellarator configurations in which transport is reduced by a factor of 2 to 4 in all three regimes as compared with a tokamak with equal aspect ratio and effective ripple and by a factor of up to 8 as compared with an equivalent $\ell = 2$ stellarator. Transport in actual stellarators (ATF-1, Heliotron-E, W VII-AS) is moderately worse than in the equivalent $\ell = 2$ stellarator.

1.Introduction.

A Monte Carlo code which was previously described and applied to axisymmetric and ripple tokamaks [1] is used to study neoclassical transport in stellarators. Transport coefficients are obtained over a wide range of mean free paths in the approximation of small gyroradius, so that a local transport coefficient associated with a given magnetic surface can be determined. A monoenergetic particle distribution which is only subject to pitch angle scattering and a vanishing electric field are used.

In this work magnetic fields are represented by their components in a Cartesian coordinate system. Only vacuum field stellarator configurations are considered (with one exception in Sec.3), so that the three field components and five of their derivatives suffice to evaluate the guiding-center drift equations. Details of the numerical procedure have already been published [1].

The results are presented in a normalized way which turned out to be adequate for describing axisymmetric and rippled tokamak cases and which is briefly repeated here for convenience. A dimensionless mean free path L^* is used:

$$L^* = \Lambda / L_c, \tag{1}$$

where Λ is the mean free path and L_c half the connection length $L_c = \pi R_o / \iota$, R_o the torus radius, ι the rotational transform (or twist) of the magnetic surface considered. A dimensionless transport coefficient D^* is introduced by

$$D^* = D / D_P, \quad D_P^* = 1, \tag{2}$$

where D_P is the plateau value

$$D_P = 0.64 \, \frac{\rho^2}{\iota^2} \frac{v}{L_c}, \tag{3}$$

v being the particle velocity ($v = \sqrt{2E/m}$) and ρ the formal gyroradius ($\rho = mv/eB_o$, B_o main magnetic field at R_o). Here, compared with [1], we changed the numerical value by a factor of 2 to conform to the standard definition $D =< x^2 > /2t$. With these normalizations the Pfirsch-Schlüter regime and the tokamak banana regime are given by [1]

$$D^*_{PS} = 1/L^*, \quad D^*_B \approx A^{\frac{3}{2}}/L^*, \tag{4}$$

where A is the aspect ratio of the magnetic surface considered.

In Sec.2, the results obtained for $\ell = 2$ stellarators are described. Since toroidal stellarators are necessarily three-dimensional configurations, their transport behaviour in the long-mean-free-path (lmfp) regime, in which the transport is proportional to the mean free path [2], is of particular interest. It is useful to compare the results obtained in this regime with those obtained for a rippled tokamak which can be described by the formula [1]

$$D^*_R = 1.65 \; \delta_e^{\frac{3}{2}} \, L^*, \tag{5}$$

where δ_e is the effective ripple defined by

$$\delta_e^{\frac{3}{2}} = \int \delta^{\frac{3}{2}}(\theta) \; \sin\theta \, d\theta \Bigg/ \int \sin\theta \, d\theta, \tag{6}$$

θ being the poloidal angle and $\delta(\theta)$ the local ripple depth evaluated along a field line, and with the integration extended between $\theta = 0$ and $\theta = \pi$. As an example we take Fig.1 which gives the magnitude of the magnetic field along a field line. A distinct value of the poloidal coordinate θ and a local ripple depth $\delta(\theta) = (B_{max} - B_{min})/(B_{max} + B_{min})$ can be assigned to each field minimum. (For each field minimum there are two adjacent field maxima, the smaller one is taken for B_{max}.) Thus, we get Fig.2 with the ripple depth δ versus poloidal angle θ. For the integration in eq.(6) we take the curve of Fig.2.

In Sec.3, results for stellarator configurations obtained by an optimization procedure are described [3, 4]. Various quantities of merit, e.g. reduced parallel current density, deepness of magnetic well, low aspect ratio, and reduced deviation from the condition for isodynamic particle drifts [5, 6], were used in the merit function during optimization. It is therefore useful to assess the actual transport properties for such configurations.

In Sec.4, $D^*(L^*)$ is computed for actual devices or designs, namely ATF-1, Heliotron-E, and W VII-AS. Section 5 presents conclusions.

A total of 25 different stellarator configurations will be considered. Obviously, this poses the problem to find a way to discuss these configurations in a concise way. Each of these

configurations is uniquely defined by data sets available in the IPP computing system. These data sets can be located by their names which consist of three mnemonic letters (in most cases the user's identification; WAD, DOM = Dommaschk, ASC = Schlüter, MYN = Mynick, CHU = Chu) plus some additional characters. While the use of these "code names" may appear puzzling at first sight, it proved to be quite helpful in avoiding misunderstandings.

2.Results for $\ell = 2$ Stellarators.

Stellarators of the $\ell = 2$ type are the simplest toroidal stellarators and we have therefore studied many cases which serve as a reference basis. Here, they are represented by the appropriate Dommaschk potentials (see Ref.[4] and Appendix). Parameters of such $\ell = 2$ stellarators are the number of periods N, the aspect ratio A, and the twist ι. Although these parameters are of course not completely independent of each other, they can be varied over a substantial range. Table I shows the cases which have been treated. Figure 3 shows $D^*(L^*)$ for a representative case together with the corresponding axisymmetric and ripple tokamak cases. The results clearly verify the so-called $1/\nu$ transport behaviour (in the notation used here this means transport proportional to L^*) [2, 7, 8]. Table II gives a more complete description of these $\ell = 2$ configurations including the magnetic well (or hill), the effective ripple δ_e, $D^*(1000)$, and D^*/D^*_R. Figures 4-6, 14-16, 22, and 27-46 give more details of these configurations. There are only small numerical factors (≈ 2) between corresponding ripple tokamak and $\ell = 2$ stellarator cases, the values for the latter being systematically larger. For $L^* = 1000$ (a typical value characterizing the lmfp regime), D^* varies by two orders of magnitude. The $\delta_e^{\frac{3}{2}}$ scaling describes $\ell = 2$ stellarators quite adequately. An even more precise representation of the results can be obtained as follows. The transport coefficient $D^*(10^3)$ is found to be proportional to N and ι. With the help of the additional scaling parameter aspect ratio A, the results can be reproduced by

$$D^*_o = 2.33\, A^{-2.35}\, \iota N L^* \tag{7}$$

to within an accuracy of 10 % for $10 \leq A \leq 40$, $0.25 \leq \iota \leq 1.0$, $5 \leq N \leq 19$.

An $\ell = 3$ stellarator [9] was treated as a test case (DOM3, Table II). As has to be expected, it is quite close to the corresponding ripple tokamak case. More surprisingly, this undisturbed $\ell = 3$ stellarator conforms to eq.(7). When the $\ell = 3$ stellarator configuration is disturbed by a homogeneous vertical field, thus shifting the magnetic axis outward, $D^*(10^3)$ can increase considerably (DOM3B with axis at $R = 101.0$ cm, DOM3A with axis at $R = 102.1$ cm). The same will be true for an $\ell = 3$ stellarator with shifted axis due to finite plasma β. For $\ell = 3$ stellarators see Figs.17 and 47-55.

3.Results for Optimized Stellarators.

Here, $D^*(L^*)$ is described for configurations which were obtained by optimizations with various measures of merit.

A group of related configurations is given by WAD514, WAD384, WAD428A [3, 10]. Table III shows details of these configurations. Figure 7 shows the results $D^*(L^*)$. We used representative magnetic surfaces not far away from the "last closed outer surface". For these configurations the main optimization objective was to reduce the parallel current density, with side conditions on A and ι, and, in the case of WAD384 and WAD428A, on the magnetic well. While WAD514 indeed verifies that a factor of 4-5 can be gained in the PS regime, it demonstrates on the other hand that the local curvatures associated with the reduction of the parallel current density lead to large field ripple and very unfavourable transport behaviour in the lmfp regime. The side condition that at least a shallow magnetic well exist (WAD384, WAD428A), which was introduced to yield at least low-β MHD stability, on the one hand limits the reduction of the parallel current density obtainable but, on the other, also reduces the ripple and the transport in the lmfp regime. The improvement is such that the ripple transport is not worse than that of an $\ell = 2$ stellarator with correspondingly lower aspect ratio (such as to allow a comparable equilibrium-β value). For more details see Figs.19, 24, 62, 63, 69, 70, 74, and 75.

A second group of related configurations is given by ASC742 [3], CHU2 (a configuration close to one of the configurations of [11]) and MYN2, WAD454, and WAD421. For these configurations, the optimization directly included the trapped particle behaviour. While ASC742 was obtained with the side condition that the minimum of $B = |\vec{B}|$ on a magnetic surface decreases as little as possible with decreasing aspect ratio [3], the configuration of [11] was designed to avoid a local field ripple on the outer side of the torus and to keep the minima of B encountered along a field line independent of the position along the field line. WAD454 and WAD421 were obtained by including the deviation of B on a magnetic surface from the functional form $B = B(U)$ in the merit function, where U is the vacuum potential. Since $B(U)$ leads to isodynamic particle drifts, minimizing the deviation from the functional form and weighting it with the ripple [12] should improve the trapped particle transport. Table III shows details of these configurations; Figs.8 and 9 contain the results $D^*(L^*)$. For more details of these configurations see Figs.18, 20, 23, 25, 56-61, 66-68, 71-73.

The results show that an improvement in the lmfp regime is indeed possible. ASC742 shows a reduction factor of about 2 in the PS and plateau regimes together with a reduction factor of about 3 as compared with the ripple tokamak in the lmfp regime. This improvement comes about because the ripple occurs in the low-curvature region [13]; the ripple is so large, however, that the transport is still worse by a factor of 6 than that of an $\ell = 2$ stellarator with equal N, A, and ι (see eq.(7)). The CHU2 configuration shows about the same reduction factor of 3 if compared with the equivalent ripple tokamak and is still worse by a factor of 2.5 than the equivalent $\ell = 2$ stellarator. The underlying optimization idea [14] is, however, correct. The configuration MYN2, which is a special ripple tokamak (see Fig.1) realizing the attempted ripple structure ($\sigma = +1$ in the notation of Ref.[14]), shows an improvement factor of about 7 as compared with the standard ripple tokamak of equal effective ripple.

The WAD454 configuration was optimized towards $B = B(U)$ without side conditions on the magnetic well, and in fact it has a significant magnetic hill (Table III). On the other hand, it shows a reduction factor of up to about 8 compared with the equivalent $\ell = 2$ stellarator. This appears to be the best result hitherto achieved in this respect. It shows that the search for configurations with small ripple transport is at least worthwhile in principle. The ripple of 2.5 % is the smallest out of all the configurations considered here with equal ι and A. This, however, is only one cause of the favourable result, which is mainly due to a reduction factor of about 2.4 as compared with the equivalent ripple tokamak, while the equivalent $\ell = 2$ stellarator is a factor of 2.4 worse than the ripple tokamak.

Figures 72 and 73 show the ripple structure of WAD454. Since there is a substantial ripple on the outside of the torus, we conclude that the favourable result cannot be explained by the concept of Ref.[14]. The ripple structure is more complicated than assumed in Ref.[14], so that the definition of σ does not apply. Generalizing the definition to be $\sigma = (\delta_{in} - \delta_{out})/(\delta_{in} + \delta_{out})$ where $_{in}$ and $_{out}$ refer to the toroidally inner and outer side of a magnetic surface, we can attribute $\sigma = +0.1$ to this configuration. The ripple structure shows that the fraction of deeply trapped (localized) particles is small.

The WAD421 configuration was optimized in the same way but with the side condition of a shallow magnetic well. It shows a slight improvement as compared with the equivalent ripple tokamak. The ripple is so small that the improvement as compared with the $\ell = 2$ stellarator is still about 3. This appears to be the best value hitherto known for a stellarator with approximately marginal magnetic well. Figures 67 and 68 show the ripple structure of WAD421.

Finally, a configuration with a deep magnetic well is considered, WAD409 [15]; details thereof are shown in Table III. Here, ripple transport is a factor of 3 larger than the equivalent ripple tokamak and a factor of 5 larger than the equivalent stellarator. See also Figs. 20, 25, 64, 65.

4.Results for ATF-1, Heliotron-E, and W VII-AS.

Table III shows details of three actual devices or designs, namely ATF-1, Heliotron-E, and W VII-AS, and Fig.10 containes the results $D^*(L^*)$.

The ATF-1 configuration [16] shows a $D^*(L^*)$ curve which is quite close to that of the equivalent $\ell = 2$ stellarator, except in the lmfp regime in which $D^*(L^*)$ is a factor of about 2.5 larger. This configuration has the deepest magnetic well (2.2 % at the aspect ratio of 10, which is considered in the Monte Carlo simulation) encountered together with this value of ripple transport. For more details see Figs.21, 26, 76, and 77.

The configuration representing Heliotron-E [17] shows somewhat larger transport for all values of L^* than the equivalent $\ell = 2$ stellarator, e.g. a factor of approximately 4 in the lmfp regime. On the other hand, the absolute value of $D = D^* D_P$ is not actually high as compared with other devices since the twist is so strong. For more details see Figs.21, 26, and 78-80.

Optimization studies observing the existing structure of the W VII device had led to the W VII-AS design [18]. It shows an improvement factor of about 1.5 in the PS regime, of about 2 in the plateau regime, and a transport coefficient which is a factor of approximately 2 larger in the lmfp regime compared with the equivalent $\ell = 2$ stellarator. For more details see Figs.21, 26, and 81-83.

5.Conclusion.

A synopsis of some of the results obtained in the previous sections is given in Fig.11. These show that different stellarators may indeed have quite different lmfp transport behaviour as obtained from D^*. Here, we do not claim that differences corresponding to the factors in D^* occurring in the various configurations will actually be observed, since the assumptions of the calculations performed here (mainly large r_o/ρ_i and vanishing electric field) will not be true in actual devices. Configurations with substantially different values of D^* should, however, exhibit significantly different transport behaviour when subjected to more refined and self-consistent neoclassical transport studies.

Figure 11 also shows an increasing transport coefficient with deepening of the magnetic well; no configuration has been found as yet with a magnetic well of several per cent and a small transport coefficient. This is another example of the general tendency that any measure improving the MHD properties will increase local ripple depths.

In order to demonstrate the range of validity of the results as far as the value of r_o/ρ is concerned, we consider the simple $\ell = 2$ stellarator DOM2A at $L^* \approx 32$, so that D^* is substantially larger than unity, $D^* \approx 4$. Figure 12 shows that for $r_o/\rho > 5 \cdot 10^2$ (e.g. corresponding to approximately 8 keV deuterons at a radius r_o of 1 m and a main field of 6 T) the local transport coefficient determined here is valid. This is in accordance with our previous result [1], $r_o/\rho > \pi D^*/\iota\, \delta_e^{\frac{1}{2}}$. Since this limitation is obtained due to the fact that a loss cone in velocity space develops for larger ρ (i.e. larger drift velocity) this is really a limit on ρ for fixed plasma radius. No difficulty arises if surfaces with larger aspect ratio (i.e. smaller r_o) are considered for fixed ρ. We can adapt the usual argument [8] to determine the validity of our assumption of vanishing electric field. The assumption $\tau_\delta < \tau_{\nabla U}$ where τ_δ is the detrapping time $\delta_e \Lambda/v$ and $\tau_{\nabla U}$ the poloidal transit time associated with the $\nabla U \times B$ drift, together with $eU \approx E$, leads to

$$L^* < \frac{r_o\, \iota}{\rho\, \delta_e\, A}$$

as the limitation on L^* for the results presented here to be valid. Since trapped particles play an essential role only for $L^* > \delta_e^{\frac{-3}{2}}$, a minimum value of r_o/ρ

$$\frac{r_o}{\rho} > A/\delta_e^{\frac{1}{2}}\, \iota$$

is required for our results to be meaningful in the ripple regime.

Our results for Heliotron-E (considered without electric field) are in accordance with Wakatani's [19] results. In particular: i) the minimum value of D^* is about 3.5; ii) significantly larger values for D^* ($D^* \approx 8$) than the plateau level can be calculated in the framework of a local transport coefficient; iii) the corresponding ratio of r_o/ρ is as low as 60 in his work, which is significantly less conservative than the estimate obtained above. This adds significance to results obtained for large r_o/ρ. It is difficult to obtain a closer comparison with Wakatani's work since the model case $d = 0$ is in principle inconsistent in stellarators if d is interpreted as ellipticity of the flux surfaces. Therefore, such a case never occurs among ours, since we do not use field models but actual 3D vacuum magnetic fields. Supporting evidence for the above estimates concerning the neglect of the electric field can also be found in Ref.[19].

Finally, we mention that the configurations considered here had smooth magnetic surfaces in the sense that magnetic field lines can be followed $> 10^2$ times around the torus, yielding well closed surfaces like the inner ones shown in Fig.37. This figure also shows an island chain at $\iota = \frac{1}{2}$. The formal calculation of a local transport coefficient near a magnetic surface with a rotational transform so that an island chain can develop will show an increase in the transport when the particles reach the islands. An example is given in Fig.13.

A concise version of this paper has been published elsewhere [20]. In this IPP-report a few minor corrections to the published paper have been made.

Acknowledgement.

The authors would like to thank Karin Klug for composing this report with TEX.

Appendix.

DOMMASCHK POTENTIALS. Earlier papers [4] can be summarized as follows: The magnetic field B is given by its scalar potential V (R, φ, z cylindrical coordinates):

$$\vec{B} = \nabla V, \ \Delta V = 0$$

$$V = \varphi + \sum_{m,\ell} V_{m,\ell} \qquad m = 0, N, 2N \ldots \qquad \ell = 0, 1, 2 \ldots$$

N = number of periods; m is the toroidal index (corresponding to the number of periods), ℓ is the poloidal index (corresponding to the helical number), φ corresponds to the main field. The $V_{m,\ell}$ are separate solutions of the Laplace equation; with the usual symmetry $V_{m,\ell}(R, \varphi, z) = -V_{m,\ell}(R, -\varphi, -z)$, they are given by:

(A1)

a) $m = 0; \ \ell = 0 \qquad V_{o,o} = 0$

b) $m = 0; \ \ell = 1, 3, 5 \ldots \qquad V_{o,\ell} = A^1_{o,\ell} \cdot D_{o,\ell}$

c) $m = 0; \ \ell = 2, 4, 6 \ldots \qquad V_{o,\ell} = A^2_{o,\ell} \cdot N_{o,\ell-1}$

d) $m \neq 0; \ \ell = 0 \qquad V_{m,o} = A^1_{m,o} \cdot D_{m,o}$

e) $m \neq 0; \ \ell = 1, 3, 5 \ldots \qquad V_{m,\ell} = A^1_{m,\ell} \cdot D_{m,\ell} \cdot \cos m\varphi + A^2_{m,\ell} \cdot N_{m,\ell-1} \cdot \sin m\varphi$

f) $m \neq 0; \ \ell = 2, 4, 6 \ldots \qquad V_{m,\ell} = A^1_{m,\ell} \cdot D_{m,\ell} \cdot \sin m\varphi + A^2_{m,\ell} \cdot N_{m,\ell-1} \cdot \cos m\varphi$

$D_{m,\ell}$ and $N_{m,\ell-1}$ are the ”Dirichlet” and the ”Neumann” type Fourier coefficients of the scalar potential in the notation of reference [4].

The constant coefficients $A^{IDN}_{m,\ell}, IDN = 1, 2$ have to be chosen separately for each configuration. A homogeneous vertical field B_{zo} is given by

$$V_{o,1} = A^1_{o,1} \cdot D_{o,1} = B_{zo} \cdot z\,.$$

Examples of $D_{m,\ell}$ and $N_{m,\ell-1}$ are as follows:

$$D_{o,1} = z$$

$$D_{o,3} = z^3/3! + (-R^2 + 2\ln(R) + 1) \cdot z/4$$

$$N_{o,1} = \ln(R) \cdot z$$

$$N_{o,3} = \ln(R) \cdot z^3/3! + [R^2(-\ln(R) + 1) - \ln(R) - 1] \cdot z/4$$

and for $m \geq 3$ (since configurations with less than 3 periods are not considered in this paper) with the following abbreviations:

$$C^D_{m,o} = (R^m + R^{-m})/2$$

$$C^D_{m,1} = [-m(m-1)R^{m+2} + (m+1)(m-2)R^m + m(m+1)R^{-m+2} - (m+2)(m-1)R^{-m}] \,/\, 8m(m^2-1)$$

$$C^D_{m,2} = [m(m-1)(m-2)R^{m+4} - 2(m+2)(m-2)^2R^{m+2} + (m+2)(m+1)(m-4)R^m + m(m+1)(m+2)R^{-m+4} - 2(m+2)^2(m-2)R^{-m+2} + (m+4)(m-1)(m-2)R^{-m}] \,/\, 64m(m^2-1)(m^2-4)$$

$$C^N_{m,o} = (R^m - R^{-m}) \,/\, 2m$$

$$C^N_{m,1} = [-(m-1)R^{m+2} + (m+1)R^m - (m+1)R^{-m+2} + (m-1)R^{-m}] \,/\, 8m(m^2-1)$$

$$C^N_{m,2} = [(m-1)(m-2)R^{m+4} - 2(m^2-4)R^{m+2} + (m+1)(m+2)R^m - (m+1)(m+2)R^{-m+4} + 2(m^2-4)R^{-m+2} - (m-1)(m-2)R^{-m}] \,/\, 64m(m^2-1)(m^2-4)$$

the $D_{m,\ell}$ and $N_{m,\ell-1}$ are given by

$$D_{m,o} = C^D_{m,o}$$

$$D_{m,1} = C^D_{m,o} \cdot z$$

$$D_{m,2} = C^D_{m,o} \cdot z^2 \,/\, 2 + C^D_{m,1}$$

$$D_{m,3} = C^D_{m,o} \cdot z^3 \,/\, 3! + C^D_{m,1} \cdot z$$

$$D_{m,4} = C^D_{m,o} \cdot z^4 \,/\, 4! + C^D_{m,1} \cdot z^2 \,/\, 2 + C^D_{m,2}$$

$$D_{m,5} = C^D_{m,o} \cdot z^5 \,/\, 5! + C^D_{m,1} \cdot z^3 \,/\, 3! + C^D_{m,2} \cdot z$$

$$N_{m,o} = C^N_{m,o}$$

$$N_{m,1} = C^N_{m,o} \cdot z$$

$$N_{m,2} = C^N_{m,o} \cdot z^2 \,/\, 2 + C^N_{m,1}$$

$$N_{m,3} = C^N_{m,o} \cdot z^3 \,/\, 3! + C^N_{m,1} \cdot z$$

$$N_{m,4} = C^N_{m,o} \cdot z^4 \,/\, 4! + C^N_{m,1} \cdot z^2 \,/\, 2 + C^N_{m,2}$$

$$N_{m,5} = C^N_{m,o} \cdot z^5 \,/\, 5! + C^N_{m,1} \cdot z^3 \,/\, 3! + C^N_{m,2} \cdot z$$

Thus, the center point of the potentials $V_{m,\ell}$ with $\ell \geq 2$, is $R = 1$, $z = 0$, and $B_\varphi(R = 1) \equiv B_{\varphi 0} = 1$.

For the $\ell = 2$ stellarators of Table II only $D_{m,2}$, $D_{m,4}$, $N_{m,1}$ and $N_{m,3}$ are used. The corresponding coefficients $A^{IDN}_{m,\ell}$ are given in Table IV; these $\ell = 2$ stellarators are dominated by $D_{m,2}$ and $N_{m,1}$.

Other configurations used in this paper are much more complicated. In Tables IV to XV we give coefficients $A^{IDN}_{m,\ell}$ for all configurations where Dommaschk potentials have been used.

References.

1. W. Lotz, J. Nührenberg, *Z.Naturforsch.* **37a** (1982) 899.
2. E.A. Frieman, *Phys.Fluids* **13** (1970) 490.
3. R. Chodura, W. Dommaschk, F. Herrnegger, W. Lotz, J. Nührenberg, A. Schlüter, *IEEE Transaction on Plasma Science* **PS-9** (1981) 221.
4. W. Dommaschk, *Z.Naturforsch.* **37a** (1982) 867; *Z.Naturforsch.* **36a** (1981) 251; *IPP-Report* **0/38** (1978).
5. D. Palumbo, *Il Nuovo Cimento* **53B** (1968) 507.
6. D. Lortz, J. Nührenberg, *in Theoretical Aspects of Controlled Thermonuclear Research (Proc.Ann. Meeting Austin, 1981)* 3B48.
7. W. Lotz, J. Nührenberg, *in Theoretical Aspects of Controlled Thermonuclear Research (Proc.Ann. Meeting Austin, 1981)* 3B41.
8. R.E. Mynick, *Phys.Fluids* **25** (1982) 325.
9. R.E. Potok, P.A. Politzer, L.M. Lidsky, *Phys.Review Letters* **45** (1980) 1328.
10. R. Chodura, W. Dommaschk, F. Herrnegger, W. Lotz, J. Nührenberg, A. Schlüter, *Proc.US-Japan Theory Workshop on 3D MHD Studies for Toroidal Devices, Oak Ridge, Tenn.* (1981).
11. T.K. Chu, H.P. Furth, J.L. Johnson, C. Ludescher, K. Weimer, *IEEE Transactions on Plasma Science,* **PS-9** (1981) 228.
12. Max-Planck-Institut fürPlasmaphysik, *Annual Report* (1982) 98.
13. A. Schlüter, *Nuclear Instruments and Methods in Phys.Research* **207** (1983) 139.
14. H.E. Mynick, T.K. Chu, A.H. Boozer, *Phys.Review Letters* **48** (1982) 322.
15. Max-Planck-Institut für Plasmaphysik, *Annual Report* (1982) 97.
16. J.F. Lyon et al., *in Plasma Physics and Controlled Nuclear Fusion Research (Proc.9th Int.Conf. Baltimore, 1982) IAEA, Vienna,* **3** (1983) 115.
17. K. Uo et al., *in Plasma Physics and Controlled Nuclear Fusion Research (Proc.8th Int. Conf. Brussels, 1980) IAEA, Vienna,* **1** (1981) 217.

18. U. Brossmann, W. Dommaschk, F. Herrnegger, G. Grieger, J. Kisslinger, W. Lotz, J. Nührenberg, F. Rau, H. Renner, H. Ringler, J. Sapper, A. Schlüter, H. Wobig, *in Plasma Physics and Controlled Nuclear Fusion Research (Proc.9th Int.Conf.Baltimore, 1982) IAEA, Vienna,* **3** (1983) 141.

19. M. Wakatani, *Nucl.Fusion* **23** (1983) 817.

20. W. Dommaschk, W. Lotz, J. Nührenberg, *Nucl.Fusion* **24** (1984) 794.

N	A	ι
5	10, 20, 40	0.50
10	10, 20, 40	0.25, 0.50, 0.96
19	10, 20	0.50

Table I: Range of parameters of $\ell = 2$ stellarators for which $D^*(L^*)$ was computed. (For explanations of N, A, ι see Table II.)

NAME	N	A_o	A	ι	W	δ_e	σ	$D^*(10^3)$	D^*/D^*_o	D^*/D^*_R
DOM2A	10	7.4	10	0.50	+1.98	8.4	0.0	52	1.00	1.25
DOM2C	10	9.0	20	0.50	+0.20	2.4	-0.3	10.2	1.00	1.63
DOM2B	10	11.7	40	0.50	+0.03	0.7	-0.7	2.0	1.00	2.0
DOM2D	10	5.9	10	0.25	-0.26	6.4	-0.1	27.5	1.06	1.00
DOM2E	10	9.1	10	0.96	+6.7	11.0	-0.1	102	1.02	2.1
DOM25	5	8.9	10	0.51	-1.68	3.5	-0.6	26.5	1.00	2.4
DOM25A	5	9.7	20	0.50	-0.63	1.2	-0.5	4.8	0.94	2.2
DOM25B	5	10.8	40	0.50	-0.17	0.6	-0.3	1.02	1.02	1.5
DOM19	19	8.4	10	0.52	+7.0	18.4	+0.1	106	1.03	0.82
DOM19A	19	11.1	20	0.50	+1.48	6.0	0.0	19	0.98	0.78
DOM3	32	23.	27	1.21	+2.4	5.6	0.0	28.	0.72	1.3
			50	0.25	+0.08	0.8	-0.1	1.95	1.03	1.55
DOM3B	32	23.	27	1.15	+0.1	5.3	-0.1	42.	1.13	2.1
			50	0.25	-2.0	0.8	-0.4	2.1	1.11	1.6
DOM3A	32	25.	30	0.91	-3.2	4.6	-0.6	110.	4.8	6.5
			50	0.48	-2.4	2.2	-1.0	29.	8.0	5.3

Table II: Parameters and results for various $\ell = 2$ stellarators (Table I) and one $\ell = 3$ stellarator (DOM3). N = number of periods; A_o = mean aspect ratio of the "last" closed magnetic surface; A = mean aspect ratio of magnetic surface considered; ι = rotational transform or twist on this surface; $W = (Q - Q_o)/Q_o$ = magnetic well depth at the magnetic axis with respect to this surface (in %); δ_e = effective ripple depth (eq.6 in %); $\sigma = (\delta_{in} - \delta_{out})/(\delta_{in} + \delta_{out})$, Ref.[14]; $D^*(10^3)$ = normalized diffusion coefficient at $L^* = 1000$; $D^*_o = 2.33 \cdot A^{-2.35}\, \iota N L^*$ = reduced diffusion coefficient (eq.7); D^*/D^*_o = ratio of diffusion coefficient to reduced diffusion coefficient for $L^* = 1000$ and the pertinent values of A, ι, and N; $D^*_R = 1.65\, \delta_e^{3/2}\, L^*$ (eq.5); D^*/D^*_R = ratio of diffusion coefficients in the ripple regime for stellarator and tokamak of equal effective ripple.

NAME	N	A_o	A	ι	W	δ_e	σ	$D^*(10^3)$	D^*/D^*_o	D^*/D^*_R	D^*/D^*_{PS}
ASC742	5	14	20	0.54	-0.08	12.4	+0.2	31	5.6	0.35	0.48
CHU2	6	9.4	14	0.15	-5.5	6.8	+1.0	10.2	2.4	0.36	1.00
MYN2	16	7.1	15	0.50	+0.10	6.0	+1.0	3.7	-	0.15	1.00
WAD384	10	25	40	0.99	-0.24	6.7	0.0	23	5.8	0.81	0.33
WAD428A	10	19	33	0.61	+0.11	7.3	+0.1	48	12.5	1.42	0.38
WAD514	10	19	40	0.79	+1.8	16.6	+0.3	1750	550	16	0.19
WAD421	5	8.1	10	0.45	-0.63	3.6	0.0	8.5	0.36	0.75	0.77
			20	0.34	-0.27	2.4	0.0	2.7	0.78	0.45	0.49
WAD454	5	6.6	10	0.44	+5.0	2.5	+0.1	2.8	0.12	0.42	0.63
			20	0.35	+1.15	2.5	+0.1	1.6	0.46	0.26	0.50
WAD409	12	6.8	10	0.35	-9.3	12.9	-0.9	220	5.0	3.1	1.55
ATF-1	12	7.3	10	0.54	-2.2	12.2	-0.3	170	2.5	2.3	1.55
HELIOTRON-E	19	11	17	1.06	+4.6	12.6	-0.1	220	3.7	2.9	1.50
			33	0.63	+0.49	3.2	-0.5	26.5	3.5	2.8	1.00
W VII-AS	5	8.5	12	0.39	-1.55	5.8	+0.2	25	1.9	1.05	0.63
			20	0.39	-0.66	3.7	+0.3	9.3	2.3	0.81	0.77

Table III: Parameters and results for various configurations. Symbols are the same as in Table II with the following exceptions: D^*/D^*_o = ratio of $D^*(10^3)$ to that of an equivalent $\ell = 2$ stellarator; $D^*_{PS} = 1/L^*$ (eq.4); D^*/D^*_{PS} = ratio of the diffusion coefficient in the Pfirsch-Schlüter regime to that of a tokamak.

NAME	m	$A^1_{m,2}$	$A^2_{m,2}$	$A^1_{m,4}$	$A^2_{m,4}$
DOM2A	10	-1.65	-1.65	-120.	-120.
DOM2C	10	-2.02	-2.02	-147.	-147.
DOM2B	10	-2.132	-2.132	0.0	0.0
DOM2D	10	-1.22	-1.22	-108.3	- 45.6
DOM2E	10	-2.08	-2.08	-184.8	- 77.6
DOM25	5	-1.40	-1.40	- 19.25	0.0
DOM25A	5	-1.47	-1.47	- 20.21	0.0
DOM25B	5	-1.489	-1.489	0.0	0.0
DOM19	19	-1.45	-1.45	-507.14	-243.42
DOM19A	19	-2.40	-2.40	-839.40	-402.90

Table IV: Coefficients $A^{IDN}_{m,\ell}$ of eq.(A 1) for the $\ell = 2$ stellarators of Table II;
IDN = 1, 2; m = 5, 10, 19; $\ell = 2, 4$; $B_{\varphi o} = 1$.

DOM3 (1982)

0	1	0	1	0.0
1	1	32	3	-1.90000E+02
2	2	32	3	1.90000E+02

DOM3A (1984)

0	1	0	1	-5.65000E-03
1	1	32	3	-1.90000E+02
2	2	32	3	1.90000E+02

DOM3B (1984)

0	1	0	1	-6.00000E-04
1	1	32	3	-1.90000E+02
2	2	32	3	1.90000E+02

Table V: Coefficients $A^{IDN}_{m,\ell}$ of eq.(A 1) for the configurations DOM3, DOM3A, and DOM3B of Table II.
IDN = 1, 2; $m = 32$, $\ell = 3$; $B_{\varphi o} = 1$.

```
          ASC742    (14.02.81)

 C    1    0    1     1.99856E-02
 1    2    0    2     3.87523E-01
 2    1    0    3     3.14099E-01
 3    1    5    0    -4.40130E-02
 4    1    5    1    -5.21119E-02
 5    2    5    1     2.96569E-01
 6    1    5    2     1.00687E+00
 7    2    5    2     1.35942E+00
 8    1    5    3    -1.01939E+01
 9    2    5    3    -1.53868E+00
10    1   1C    0     5.33649E-03
11    1   10    1     4.54419E-02
12    2   10    1    -5.12103E-02
```

Table VI: The 13 coefficients $A^{IDN}_{m,\ell}$ of eq.(A 1) for the configuration ASC742.
IDN = 1, 2; m = 0, 5, 10;
$\ell = 0, 1, 2, 3$; $B_{\varphi o} = 1$.

WAD384 (02.05.80)

0	1	0	1	8.58372E-02
1	2	0	2	4.49044E-01
2	1	0	3	7.00605E+00
3	1	10	0	1.79780E-03
4	1	10	1	2.64064E-01
5	2	10	1	-2.29912E-01
6	1	10	2	-5.06773E+00
7	2	10	2	-4.40950E+00
8	1	10	3	2.69700E+01
9	2	10	3	-2.04575E+01
10	1	20	0	-1.30617E-03
11	1	20	1	2.36318E-02
12	2	20	1	-1.91692E-02
13	1	20	2	-4.58949E-01
14	2	20	2	-2.26627E-01
15	1	20	3	-1.12294E+02
16	2	20	3	8.75384E+01

Table VII: The 17 coefficients $A_{m,\ell}^{IDN}$ of eq.(A 1) for the configuration WAD384.
IDN = 1, 2; m = 0, 10, 20;
ℓ = 0, 1, 2, 3; $B_{\varphi o}$ = 1.

```
          WAD 409    (07.12.82)

 0    1    0    1    -1.59095 E-02
 1    2    0    2     4.32068 E-03
 2    1    0    3    -1.07717E-01
 3    2    0    4    -8.44101E+00
 4    1    0    5     2.34797 E+01
 5    2    0    6    -1.73090E+03
 6    1   12    0    -3.50048E-04
 7    1   12    1    -3.97819 E-02
 8    2   12    1     3.13005 E-02
 9    1   12    2    -1.44553E+00
10    2   12    2    -1.41520 E+00
11    1   12    3     1.13582 E+00
12    2   12    3    -3.85657E+00
13    1   12    4    -1.95204E+02
14    2   12    4    -8.12254 E+01
15    1   12    5     1.18361 E+02
16    2   12    5    -4.95834E+02
17    1   12    6    -1.32120 E+04
18    2   12    6    -3.86677 E+03
19    1   24    0    -1.43277E-05
20    1   24    1     1.50232 E-04
21    2   24    1     2.81715 E-04
22    1   24    2    -2.43331E-02
23    2   24    2    -1.93066E-02
24    1   24    3     1.42775 E+00
25    2   24    3    -8.83756 E-01
26    1   24    4     2.80301E+01
27    2   24    4     3.87209 E+01
28    1   24    5     4.79048E+02
29    2   24    5     5.38171E+02
30    1   24    6     3.76233 E+03
31    2   24    6     1.72329E+04
32    1   36    0    -5.41494E-08
33    1   36    1    -5.14309 E-05
34    2   36    1    -2.58741 E-05
35    1   36    2     2.48616E-04
36    2   36    2    -1.83714E-04
37    1   36    3    -7.72539 E-02
38    2   36    3    -7.55118E-02
39    1   36    4     5.17409 E+00
40    2   36    4    -4.75668 E-01
41    1   36    5    -1.48088E+02
42    2   36    5     1.62423E+02
43    1   36    6     3.39021 E+02
44    2   36    6    -5.21346 E+03
```

Table VIII: The 45 coefficients $A^{IDN}_{m,\ell}$ of eq.(A 1)
for the configuration WAD409.
IDN = 1, 2; m = 0, 12, 24, 36;
ℓ = 0, 1, 2, 3, 4, 5, 6; $B_{\varphi o}$ = 1.

```
                WAD421    (16.02.82)
 0    1    0    1      1.67772 E-02
 1    2    0    2      2.84908E-01
 2    1    0    3      1.20079E+00
 3    1    5    0     -8.85632 E-03
 4    1    5    1     -3.64842E-02
 5    2    5    1      8.18686E-02
 6    1    5    2      1.27591 E+00
 7    2    5    2      1.54010E+00
 8    1    5    3     -2.29426E+00
 9    2    5    3     -2.77811 E-01
10    1    5    4      4.20127E+01
11    2    5    4      4.12018E+01
12    1    5    5      2.02835 E+01
13    2    5    5     -7.92812 E+01
14    1   10    0     -3.73473E-04
15    1   10    1      7.38098 E-03
16    2   10    1     -1.58853E-02
17    1   10    2     -1.32762E-01
18    2   10    2     -7.28573 E-02
19    1   10    3     -3.70148 E+00
20    2   10    3      3.12630E+00
21    1   10    4      6.38264E+00
22    2   10    4      2.27100 E+01
23    1   10    5     -3.25758E+02
24    2   10    5      1.04696E+02
```

Table IX: The 25 coefficients $A_{m,\ell}^{IDN}$ of eq.(A 1) for the configuration WAD421.
IDN = 1, 2; m = 0, 5, 10;
ℓ = 0, 1, 2, 3, 4, 5; $B_{\varphi o}$ = 1.

```
          WAD 428A   (04.02.81)

 0   1    0   1      4.59139E-02
 1   2    0   2      1.15790E-01
 2   1    0   3     -7.52862E+00
 3   2    0   4      3.72016E+01
 4   1   10   0      3.09075E-03
 5   1   10   1      2.15233E-01
 6   2   10   1     -2.04892E-01
 7   1   10   2     -3.11650E+00
 8   2   10   2     -3.07562E+00
 9   1   10   3      1.87864E+01
10   2   10   3     -5.42467E+00
11   1   10   4      3.89045E+02
12   2   10   4      2.23298E+02
13   1   20   0     -3.05897E-04
14   1   20   1      4.61211E-02
15   2   20   1     -4.37743E-03
16   1   20   2     -4.24032E-01
17   2   20   2     -4.46720E-01
18   1   20   3     -7.46711E+01
19   2   20   3      6.17702E+01
20   1   20   4     -2.83494E+02
21   2   20   4     -8.50432E+01
22   1   30   0     -7.32629E-05
23   1   30   1      1.91084E-03
24   2   30   1      6.06129E-03
25   1   30   2     -1.71917E-01
26   2   30   2     -1.63470E-01
27   1   30   3     -5.04110E-01
28   2   30   3     -1.17863E+00
29   1   30   4      1.09406E+03
30   2   30   4      6.27937E+02
```

Table X: The 31 coefficients $A_{m,\ell}^{IDN}$ of eq.(A 1)
for the configuration WAD428A.
IDN, 1, 2; m = 0, 10, 20, 30;
ℓ = 0, 1, 2, 3, 4; $B_{\varphi o}$ = 1.

WAD454 (18.02.82)

0	1	0	1	2.07149E-02
1	2	0	2	1.60974E-01
2	1	0	3	1.86858E-01
3	1	5	0	-1.10102E-02
4	1	5	1	-1.09603E-01
5	2	5	1	1.10140E-01
6	1	5	2	1.24083E+00
7	2	5	2	1.50452E+00
8	1	5	3	2.26491E+00
9	2	5	3	-3.70857E+00
10	1	5	4	1.98336E+01
11	2	5	4	3.76240E+00
12	1	5	5	-1.43178E+01
13	2	5	5	-9.00436E+00
14	1	10	1	8.13945E-05
15	2	10	1	-9.36619E-05
16	1	10	2	-1.52926E-02
17	2	10	2	-4.28017E-05
18	1	10	3	6.21456E-03
19	2	10	3	4.83179E-02
20	1	10	4	-1.37902E+00
21	2	10	4	-1.20160E-02
22	1	10	5	4.21286E-01
23	2	10	5	-1.60514E-01

Table XI: The 24 coefficients $A_{m,\ell}^{IDN}$ of eq.(A 1) for the configuration WAD454.
IDN = 1, 2; m = 0, 5, 10;
ℓ = 0, 1, 2, 3, 4, 5; $B_{\varphi o}$ = 1.

```
      WAD514     (10.12.79)

0    1    0     1        4.96979E-02
1    2    0     2        5.89940E-02
2    1   10     1        3.71486E-01
3    2   10     1       -1.30392E-01
4    1   10     2       -1.84119E+00
5    2   10     2       -2.34096E+00
```

Table XII: The 6 coefficients $A_{m,\ell}^{IDN}$ of eq.(A 1) for the configuration WAD514. IDN = 1, 2; m = 0, 10; ℓ = 1, 2; $B_{\varphi o}$ = 1.

ATF-1 (03.12.82)

0	1	0	1	-7.83443E-03
1	2	0	2	1.86970E-02
2	1	0	3	7.32563E-01
3	2	0	4	-1.87997E+00
4	1	0	5	3.29415E+01
5	2	0	6	-1.44147E+03
6	1	12	0	1.35796E-04
7	1	12	1	-2.17459E-02
8	2	12	1	2.33319E-02
9	1	12	2	-1.88104E+00
10	2	12	2	-1.83583E+00
11	1	12	3	2.13727E+00
12	2	12	3	-3.33275E+00
13	1	12	4	-2.47056E+02
14	2	12	4	-1.08535E+02
15	1	12	5	-3.17583E+01
16	2	12	5	1.14177E+02
17	1	12	6	-8.07612E+03
18	2	12	6	7.30988E+03
19	1	24	0	-3.33191E-06
20	1	24	1	2.92759E-04
21	2	24	1	2.10988E-04
22	1	24	2	-9.57518E-03
23	2	24	2	-5.84367E-03
24	1	24	3	1.03515E+00
25	2	24	3	-5.91305E-01
26	1	24	4	7.01115E+01
27	2	24	4	8.01116E+01
28	1	24	5	-8.52508E+01
29	2	24	5	6.37730E+02
30	1	24	6	3.53969E+04
31	2	24	6	2.78846E+04
32	1	36	0	2.50357E-07
33	1	36	1	-5.84776E-05
34	2	36	1	-3.15962E-05
35	1	36	2	1.71885E-03
36	2	36	2	-2.80067E-04
37	1	36	3	-8.30183E-02
38	2	36	3	-2.81728E-02
39	1	36	4	4.87544E+00
40	2	36	4	-4.06821E-01
41	1	36	5	-1.47090E+02
42	2	36	5	9.02410E+01
43	1	36	6	1.01984E+03
44	2	36	6	-7.11266E+03

Table XIII: The 45 coefficients $A^{IDN}_{m,\ell}$ of eq.(A 1) for the configuration ATF-1. IDN = 1, 2; m = 0, 12, 24, 36; ℓ = 0, 1, 2, 3, 4, 5, 6; $B_{\varphi o}$ = 1.

HELIOTRON-E (02.07.81)

0	1	0	1	-2.58094E-03
1	2	0	2	1.75404E-01
2	1	0	3	1.16127E-01
3	2	0	4	7.19467E-01
4	1	19	0	5.43151E-06
5	1	19	1	-1.31397E-02
6	2	19	1	1.31234E-02
7	1	19	2	-3.17242E+00
8	2	19	2	-3.16694E+00
9	1	19	3	2.95964E+00
10	2	19	3	-3.76385E+00
11	1	19	4	-1.14361E+03
12	2	19	4	-5.73630E+02
13	2	19	6	-1.30972E+05
14	1	38	2	-1.94499E-03
15	2	38	2	-5.56524E-04
16	1	38	3	8.61880E-01
17	2	38	3	-8.76125E-01
18	1	38	4	2.54137E+02
19	2	38	4	2.71752E+02
20	2	38	6	3.86664E+05

Table XIV: The 21 coefficients $A_{m,\ell}^{IDN}$ of eq.(A 1) for the configuration Heliotron-E.
IDN = 1, 2; m = 0, 19, 38;
ℓ = 0, 1, 2, 3, 4, 6; $B_{\varphi o}$ = 1.

WVII-AS (28.04.83)

0	1	0	1	9.43240E-03
1	2	0	2	2.55341E-01
2	1	0	3	4.10242E-02
3	2	0	4	-1.40220E+01
4	1	0	5	-2.99792E+01
5	2	0	6	-3.87726E+03
6	1	5	0	-1.21413E-02
7	1	5	1	1.12792E-02
8	2	5	1	1.90922E-01
9	1	5	2	1.25878E+00
10	2	5	2	1.35643E+00
11	1	5	3	-4.15263E+00
12	2	5	3	1.63836E-01
13	1	5	4	4.06992E+00
14	2	5	4	-9.04059E+00
15	1	5	5	-1.35852E+02
16	2	5	5	1.20441E+02
17	1	5	6	-3.19222E+03
18	2	5	6	-1.75839E+04
19	1	10	0	4.71873E-04
20	1	10	1	1.47238E-02
21	2	10	1	-1.05725E-02
22	1	10	2	2.37015E-01
23	2	10	2	3.51854E-01
24	1	10	3	-3.33006E+00
25	2	10	3	1.60217E+00
26	1	10	4	3.81763E+01
27	2	10	4	4.07500E+01
28	1	10	5	6.01416E+01
29	2	10	5	3.44756E+02
30	1	10	6	3.76945E+02
31	2	10	6	-2.09760E+04
32	1	15	0	4.58071E-05
33	1	15	1	-1.00904E-03
34	2	15	1	3.35741E-03
35	1	15	2	-4.03158E-02
36	2	15	2	1.65178E-02
37	1	15	3	3.59866E-02
38	2	15	3	-1.36241E-01
39	1	15	4	1.50701E+01
40	2	15	4	5.76041E+00
41	1	15	5	-2.15314E+02
42	2	15	5	1.93934E+02
43	1	15	6	2.62102E+03
44	2	15	6	9.37200E+02

Table XV: The 45 coefficients $A^{IDN}_{m,\ell}$ of eq.(A 1) for the configuration W VII-AS.
IDN = 1, 2; m = 0, 5, 10, 15;
ℓ = 0, 1, 2, 3, 4, 5, 6; $B_{\varphi o}$ = 1.

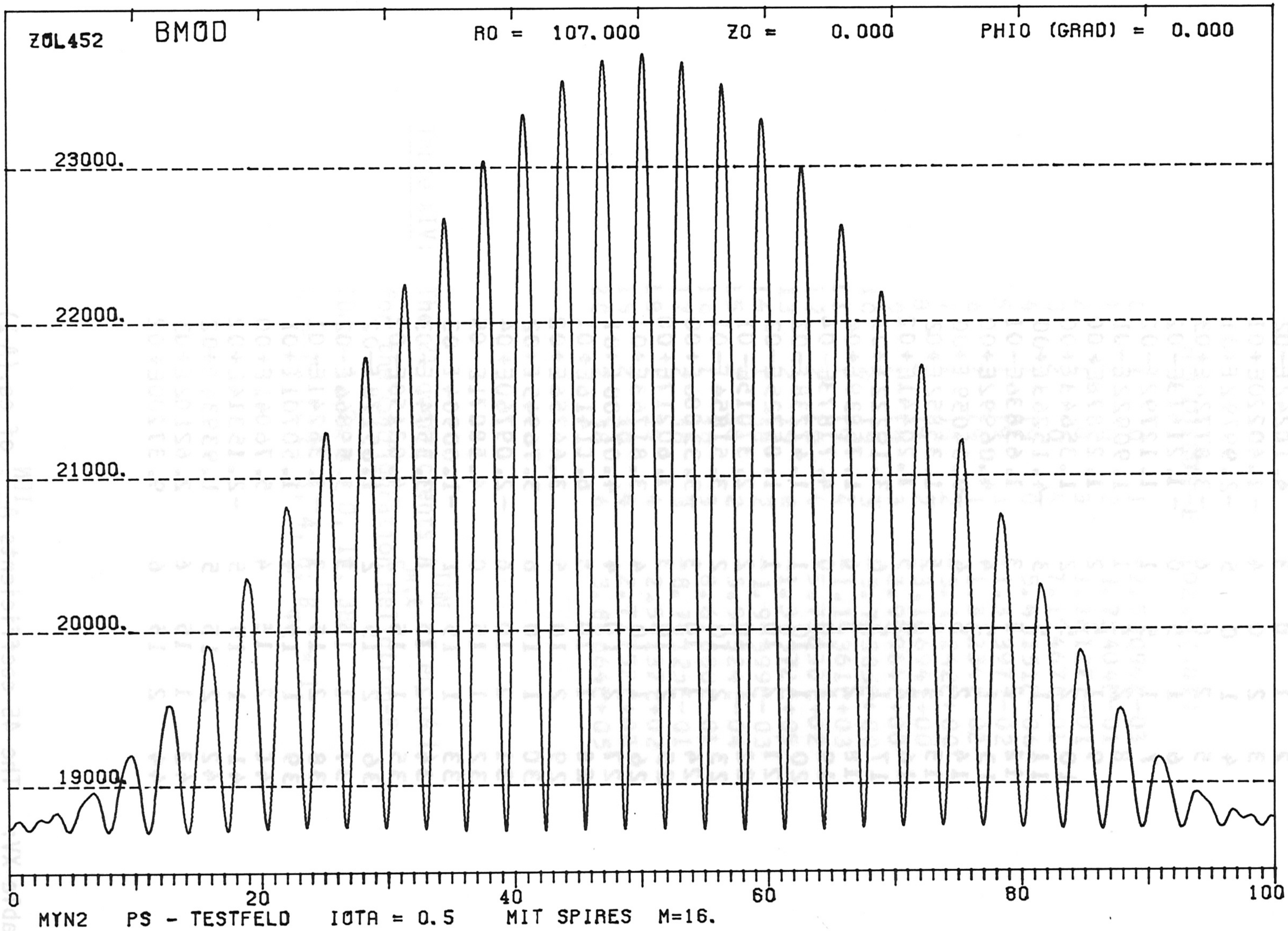

Fig.1: Magnitude of magnetic field along a field line of configuration MYN2, $N = 16$, $A = 15$, $\iota = 0.50$, $\sigma = +1.0$.

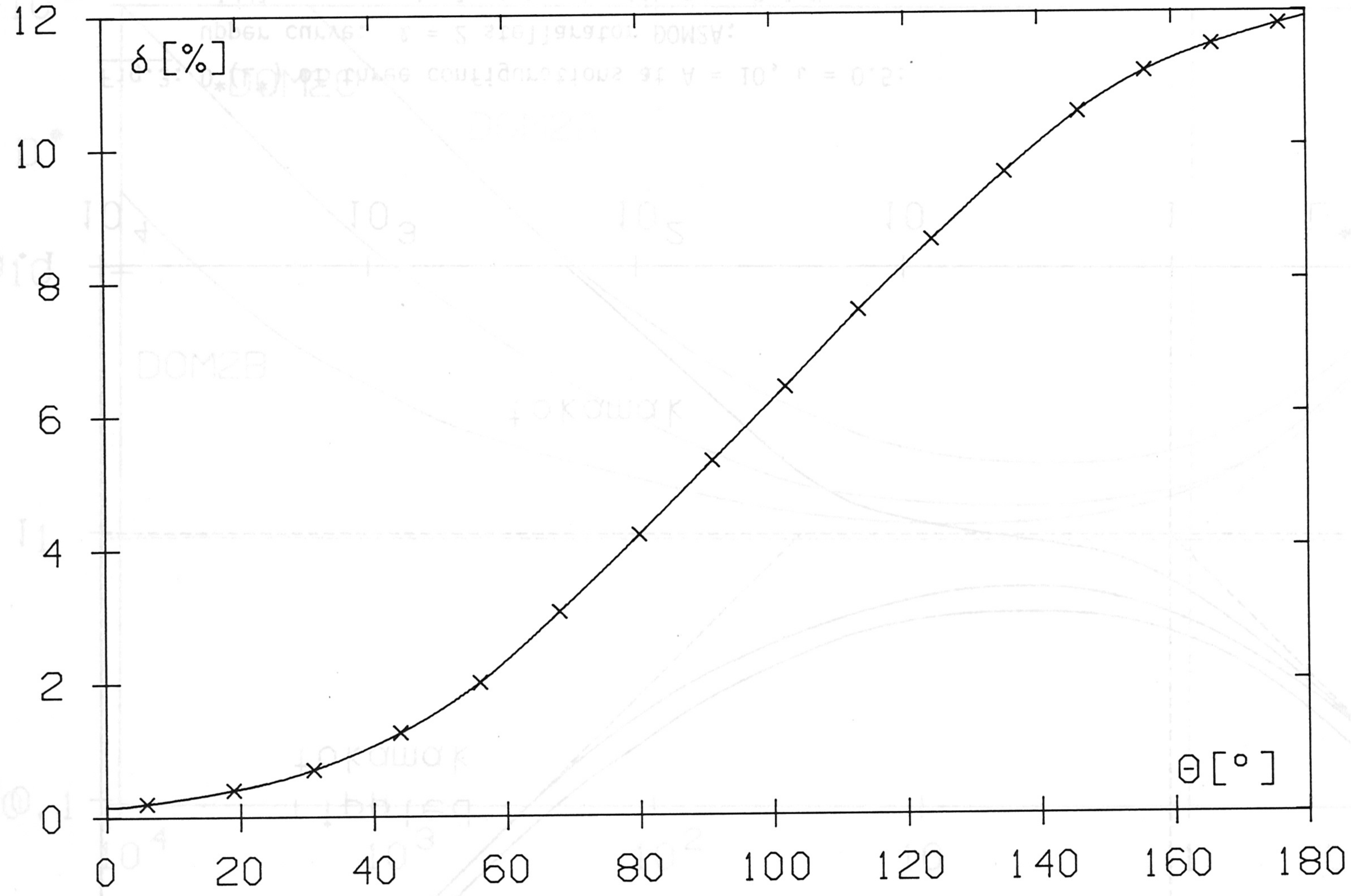

<u>Fig.2</u>: Ripple depth $\delta = (B_{max} - B_{min})/(B_{max} + B_{min})$ versus poloidal angle Θ for configuration MYN2 evaluated from Fig.1.
Field minima are at Θ = 6, 19, 31, 44, 56, 68, 80, 91, 102, 113, 124, 135, 146, 156, 166, and 176^0. This δ(Θ) is used in eq.(6).

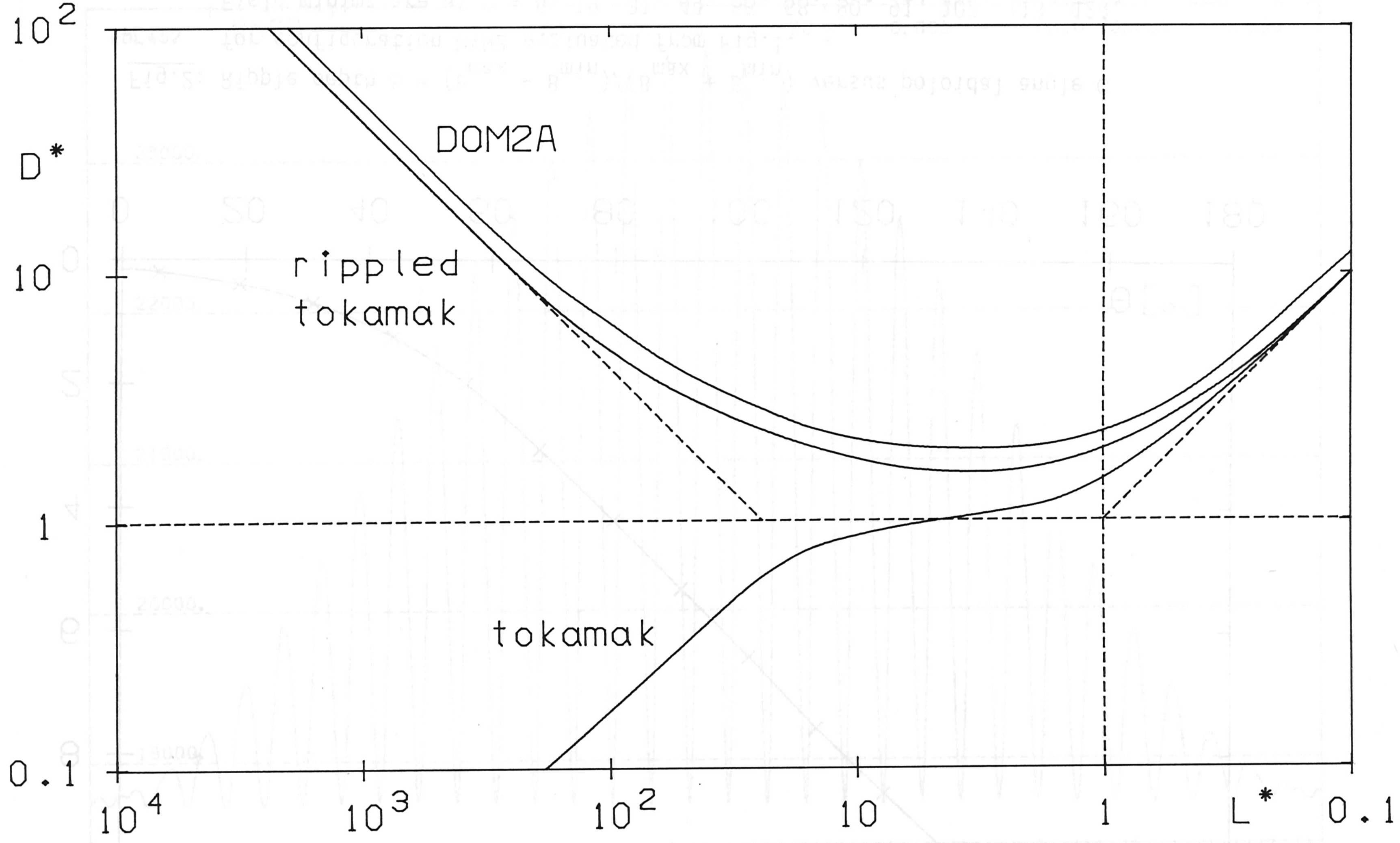

Fig.3: $D^*(L^*)$ of three configurations at $A = 10$, $\iota = 0.5$:

upper curve: $\ell = 2$ stellarator DOM2A;

middle curve: ripple tokamak with $\delta_e = 8.4$ %;

lower curve: tokamak without ripple.

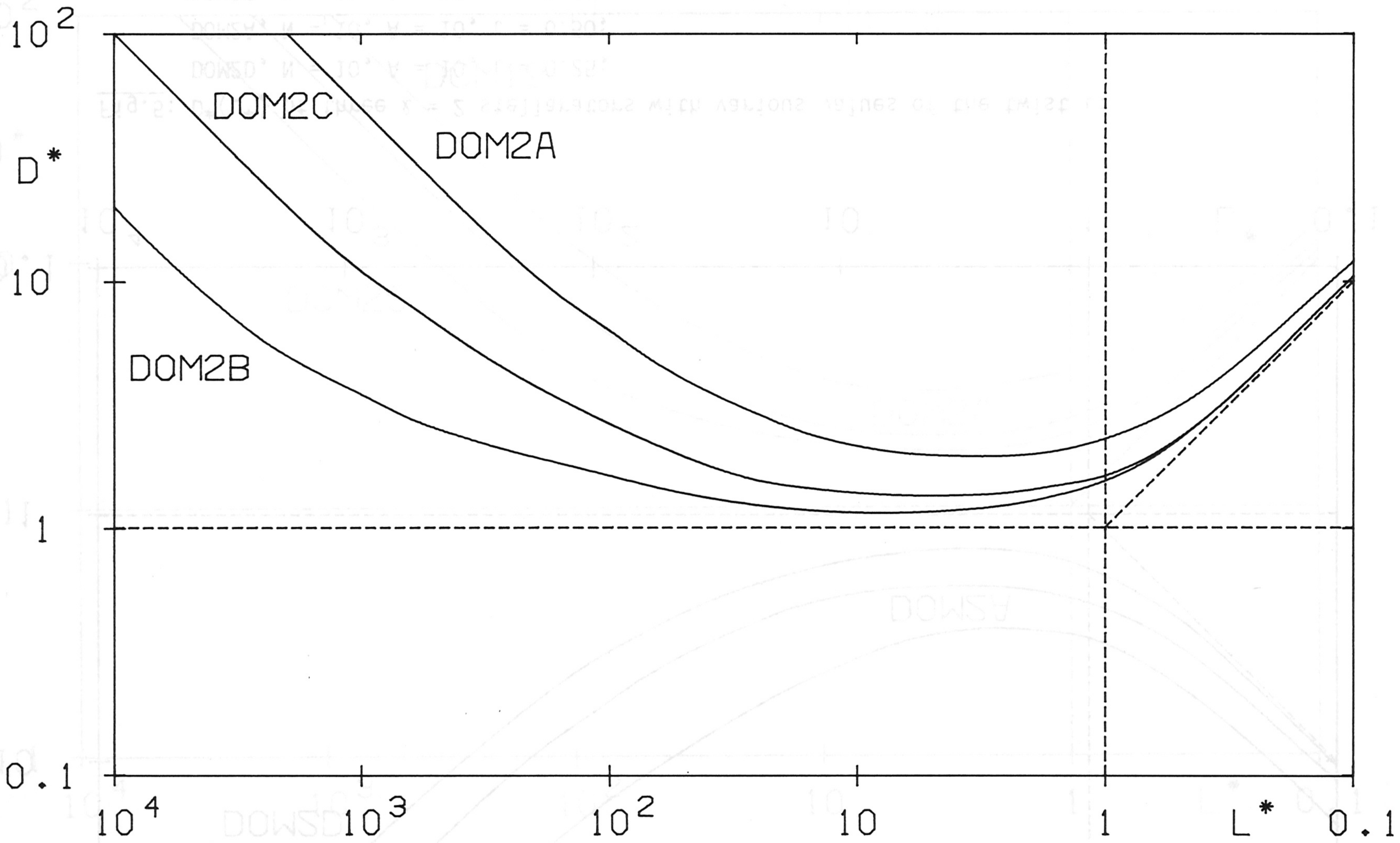

Fig.4: $D^*(L^*)$ of three $\ell = 2$ stellarators with various values of aspect ratio A:

DOM2A, $N = 10$, $A = 10$, $\iota = 0.50$;

DOM2C, $N = 10$, $A = 20$, $\iota = 0.50$;

DOM2B, $N = 10$, $A = 40$, $\iota = 0.50$.

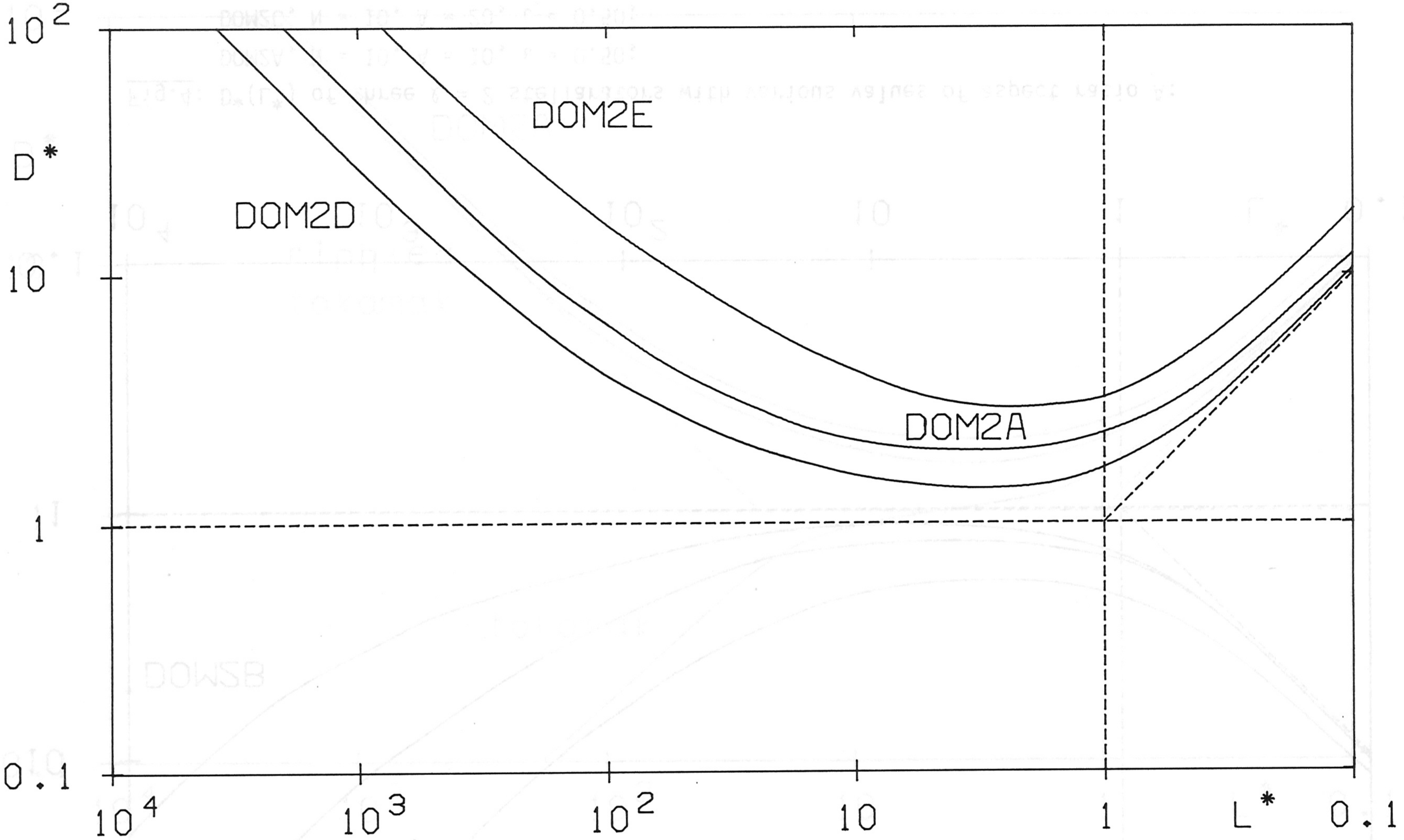

Fig.5: D*(L*) of three ℓ = 2 stellarators with various values of the twist ι:
DOM2D, N = 10, A = 10, ι = 0.25;
DOM2A, N = 10, A = 10, ι = 0.50;
DOM2E, N = 10, A = 10, ι = 0.96.

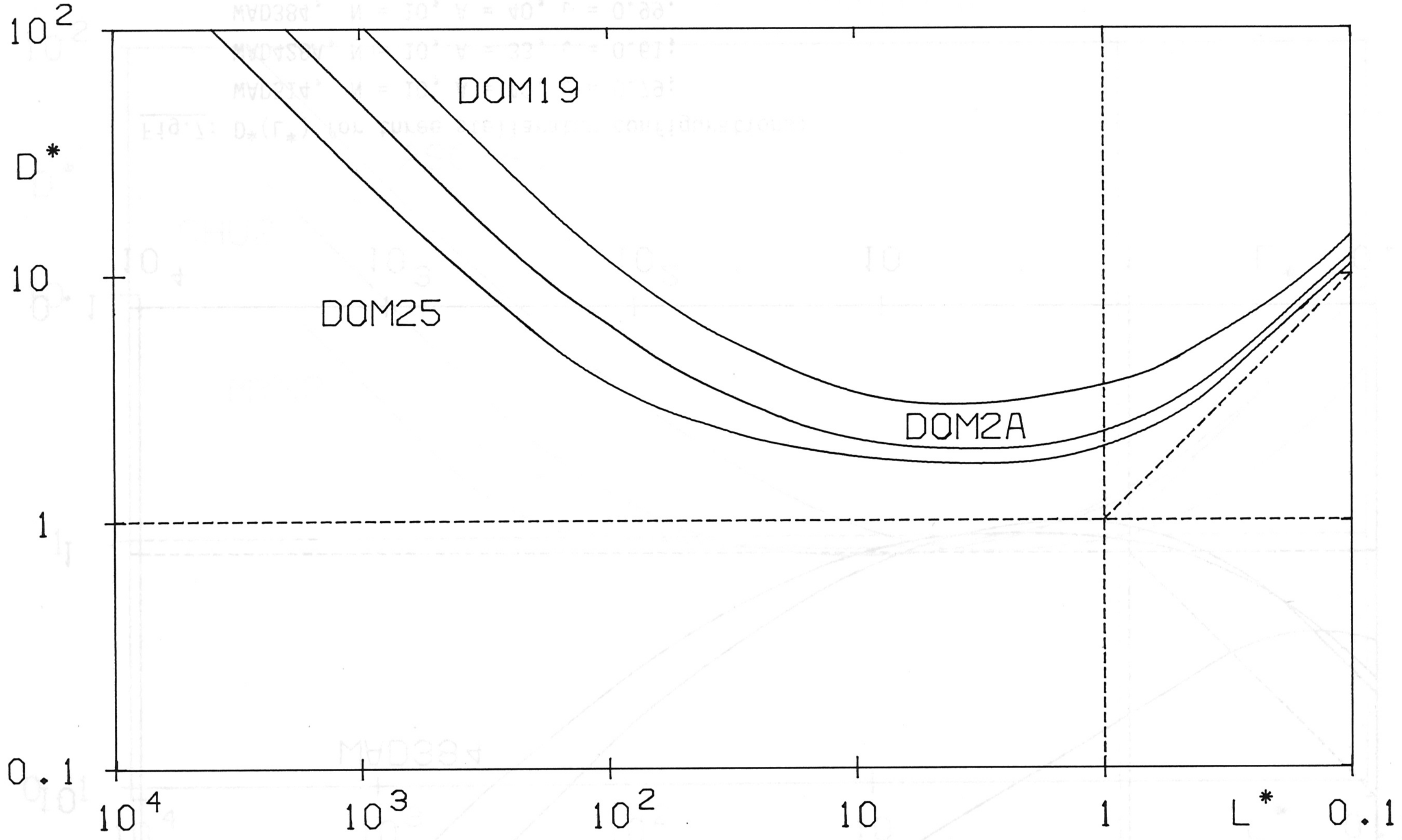

<u>Fig.6</u>: D*(L*) of three ℓ = 2 stellarators with various numbers of periods N:

DOM25, N = 5, A = 10, ι = 0.51;

DOM2A, N = 10, A = 10, ι = 0.50;

DOM19, N = 19, A = 10, ι = 0.52.

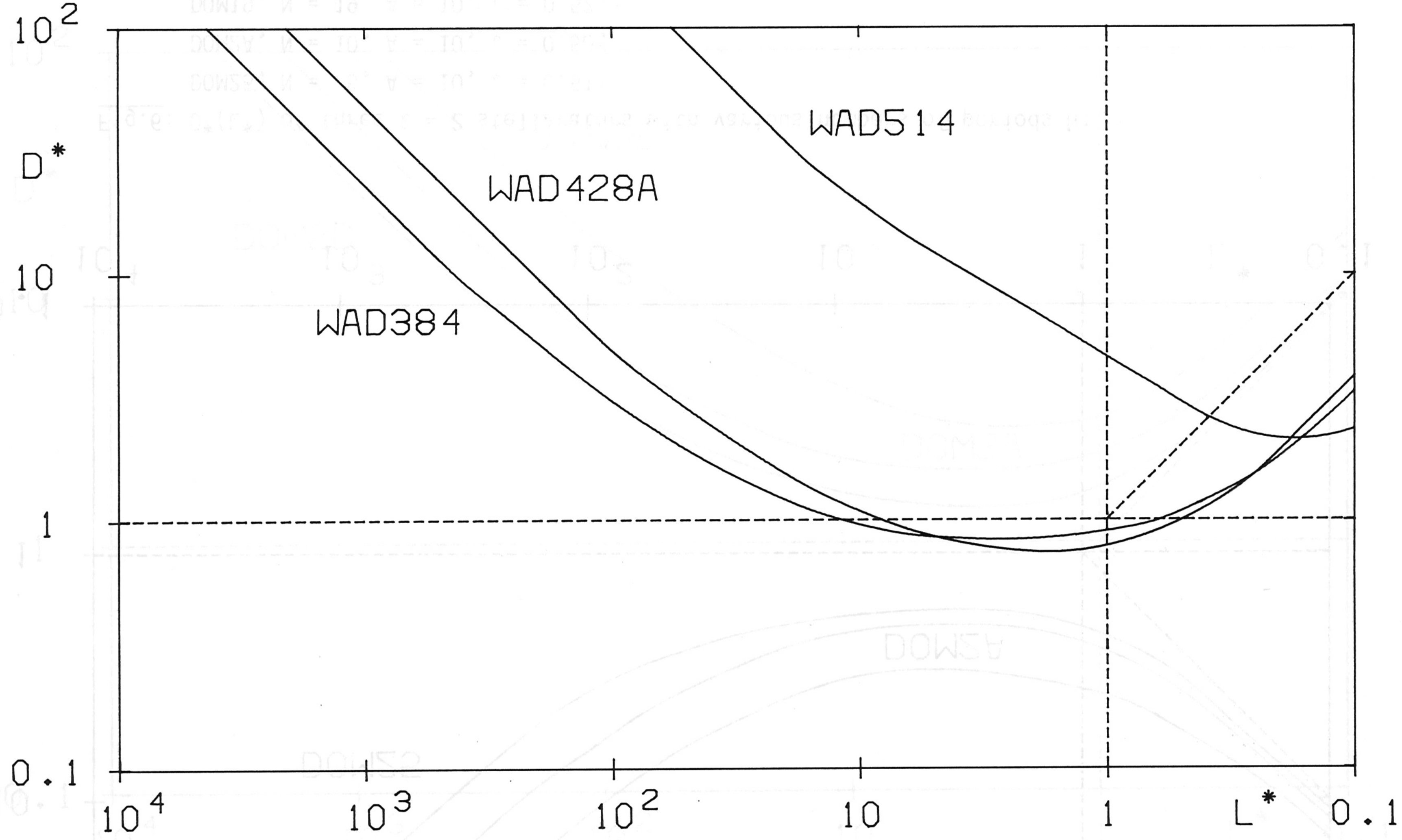

Fig.7: $D^*(L^*)$ for three stellarator configurations:
WAD514, $N = 10$, $A = 40$, $\iota = 0.79$;
WAD428A, $N = 10$, $A = 33$, $\iota = 0.61$;
WAD384, $N = 10$, $A = 40$, $\iota = 0.99$.

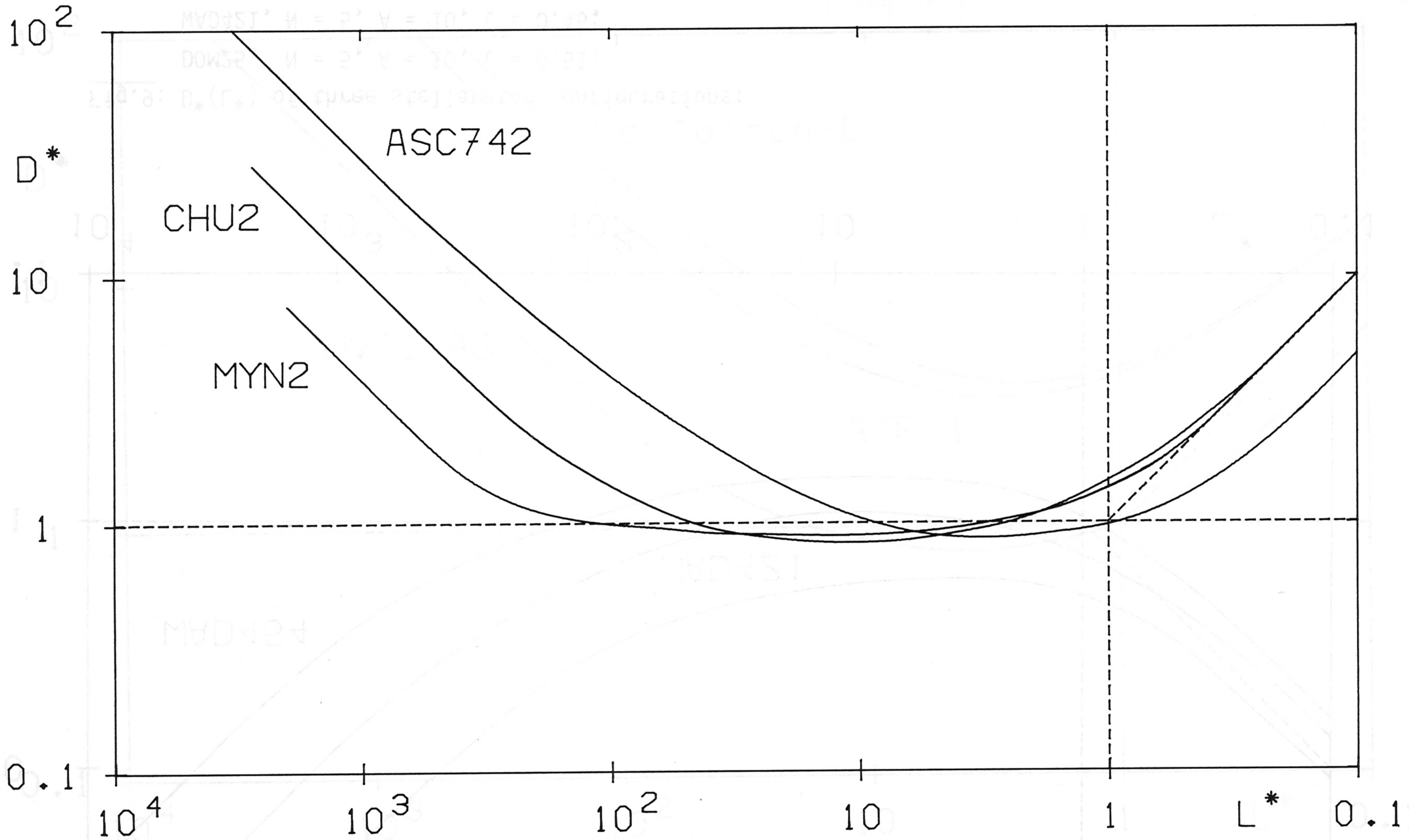

Fig.8: $D^*(L^*)$ of three configurations:

ASC742, $N = 5$, $A = 20$, $\iota = 0.54$;

CHU2, $N = 6$, $A = 14$, $\iota = 0.15$;

MYN2, $N = 16$, $A = 15$, $\iota = 0.50$.

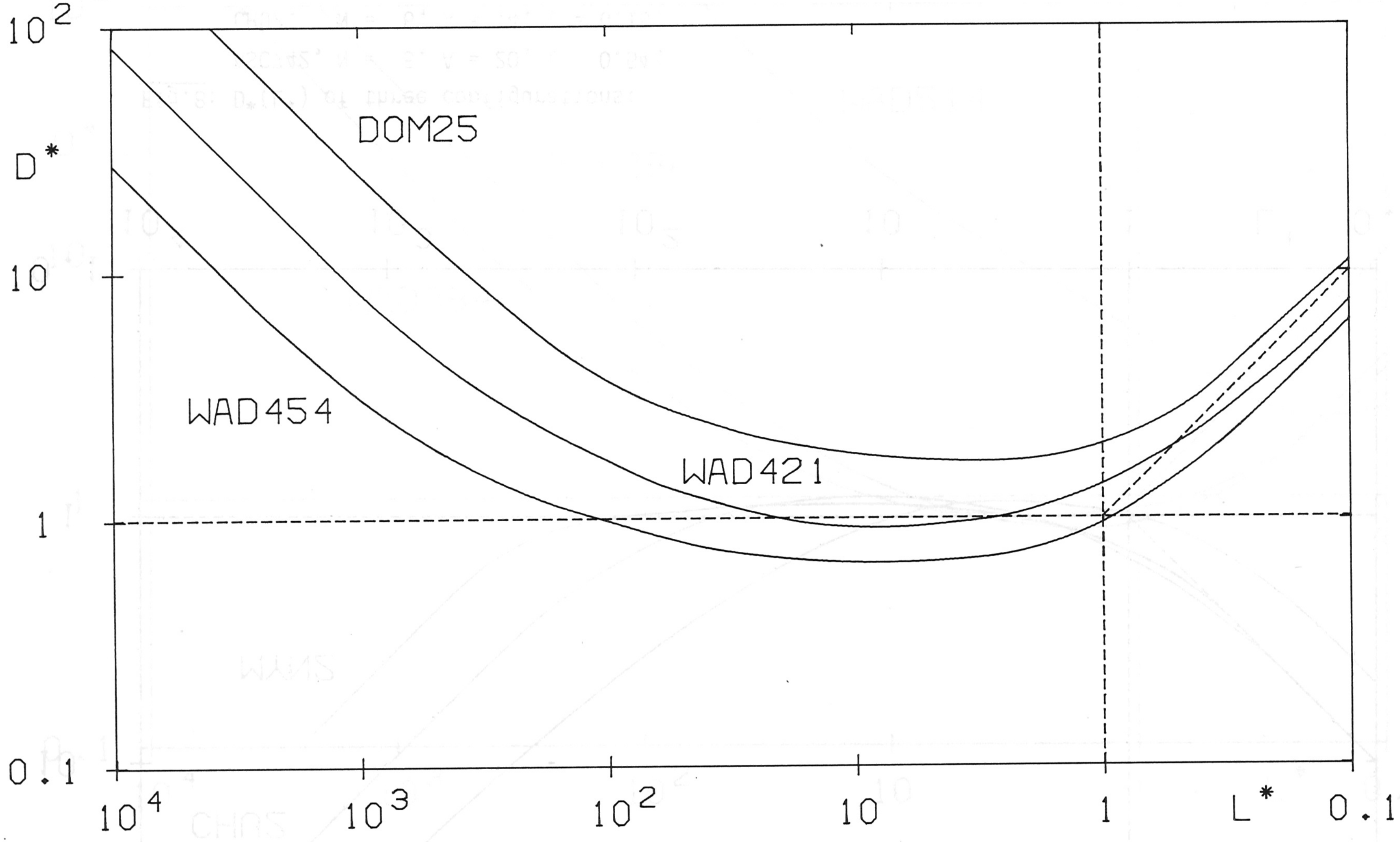

Fig.9: $D^*(L^*)$ of three stellarator configurations:

DOM25, $N = 5$, $A = 10$, $\iota = 0.51$;

WAD421, $N = 5$, $A = 10$, $\iota = 0.45$;

WAD454, $N = 5$, $A = 10$, $\iota = 0.44$.

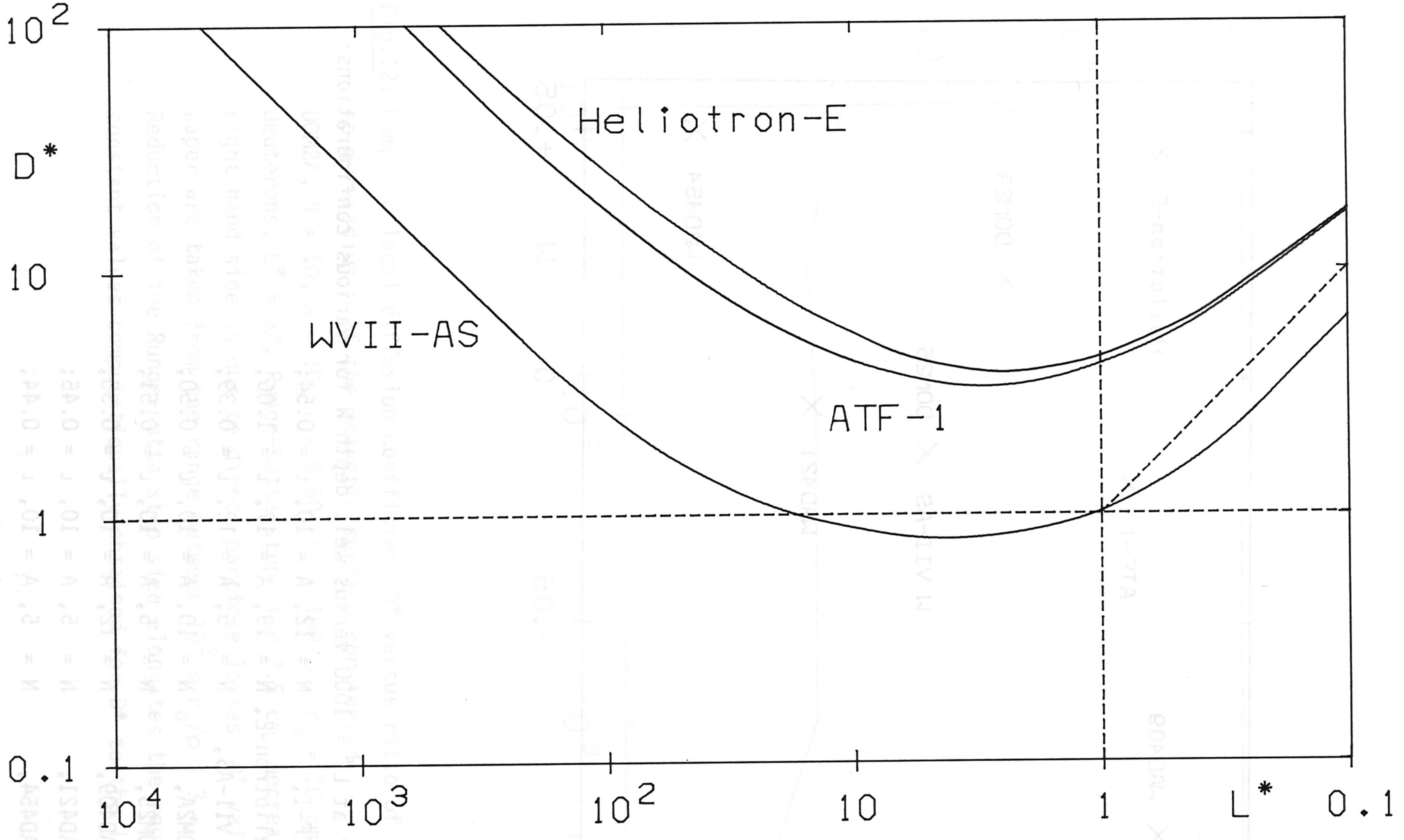

Fig.10: $D^*(L^*)$ of three actual devices:
Heliotron-E, $N = 19$, $A = 17$, $\iota = 1.06$;
ATF-1, $N = 12$, $A = 10$, $\iota = 0.54$;
W VII-AS, $N = 5$, $A = 12$, $\iota = 0.39$.

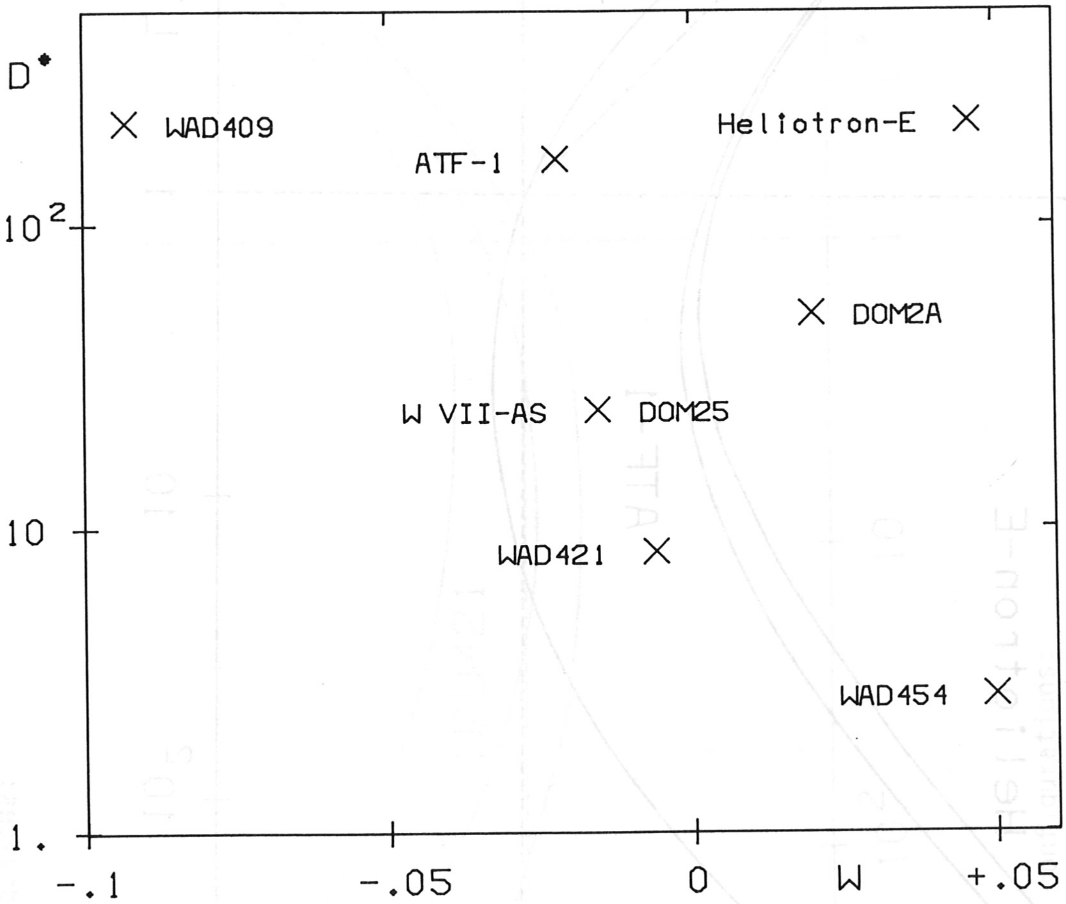

Fig.11: D* at L* = 1000 versus well depth W for various configurations:

ATF-1, N = 12, A = 10, ι = 0.54;
Heliotron-E, N = 19, A = 17, ι = 1.06;
W VII-AS, N = 5, A = 12, ι = 0.39;
DOM2A, N = 10, A = 10, ι = 0.50;
DOM25, N = 5, A = 10, ι = 0.51;
WAD409, N = 12, A = 10, ι = 0.35;
WAD421, N = 5, A = 10, ι = 0.45;
WAD454, N = 5, A = 10, ι = 0.44;
W VII-AS and DOM25 coincide.

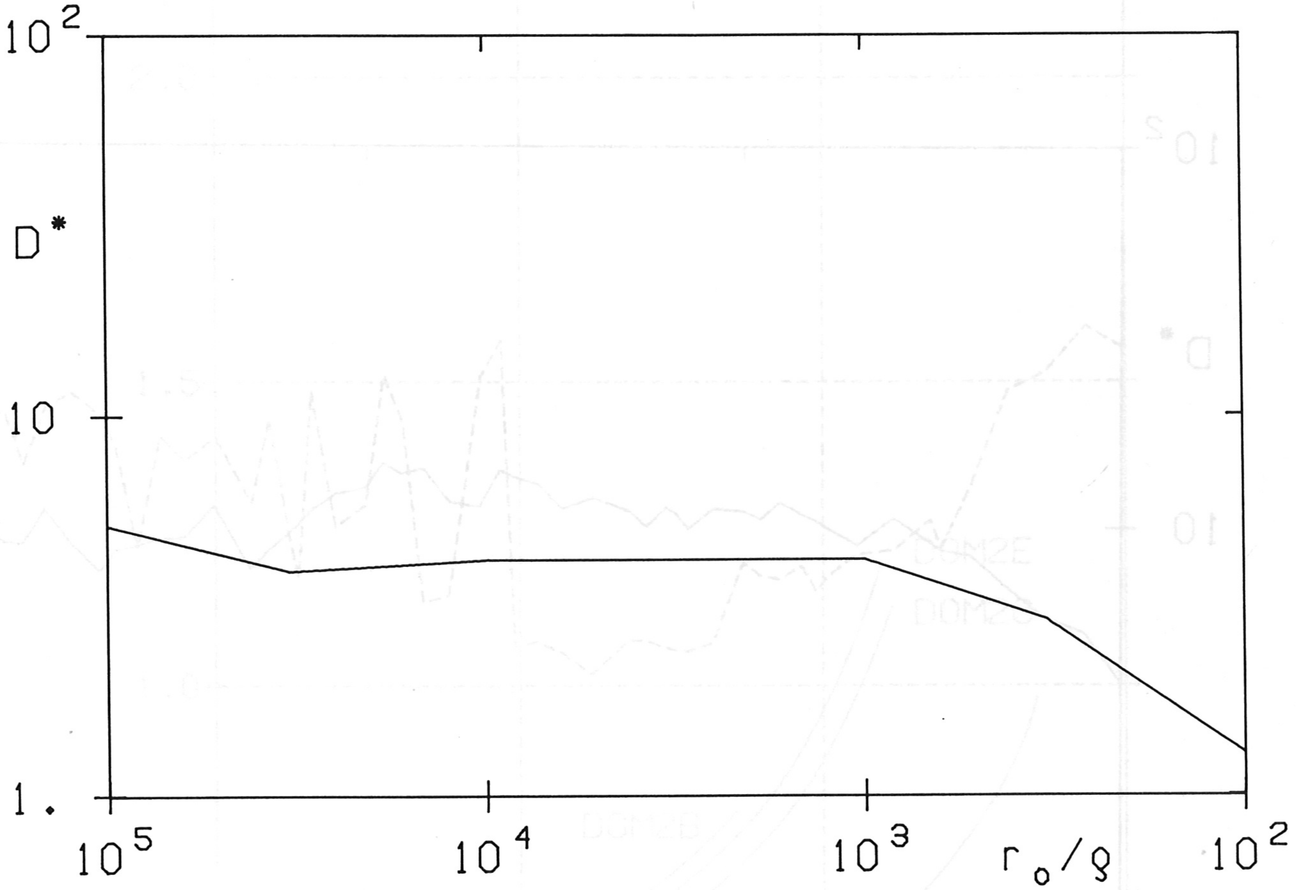

Fig.12: Computed local diffusion coefficient D^* versus ratio of radius r_o to gyroradius ρ of the magnetic surface considered. DOM2A, $N = 10$, $A = 10$, $\iota = 0.50$, $R_o = 100$ cm, $r_o = 10$ cm, $B_o = 2$ T, deuterons, $L^* = 32$, Runge-Kutta step size 2.5 cm. Decreasing D^* at right hand side is due to direct particle losses. D^* values of this paper are taken from the range between $10^3 \leq r_o/\rho \leq 3 \cdot 10^4$. Reduction of the Runge-Kutta step size elongates the region of constant values computationally obtained for D^* to the left.

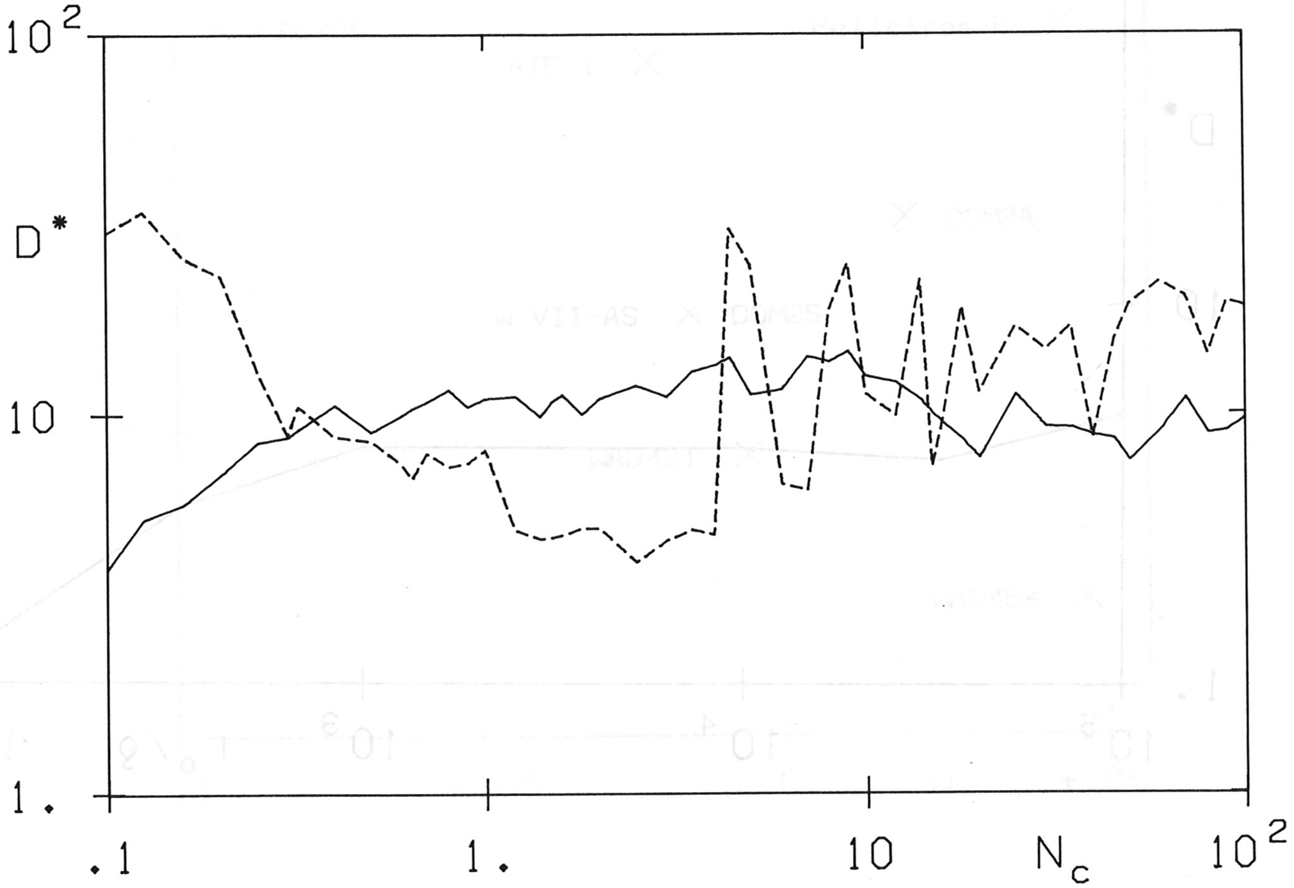

Fig.13: D^* at $L^* = 160$ versus number N_c of 90° collisions, $r_o/\rho = 3 \cdot 10^4$.
Solid curve: DOM2A, $N = 10$, $A = 10$, $\iota = 0.50$;
dashed curve: DOM25, $N = 5$, $A = 10$, $\iota = 0.51$;
magnetic surface close to chain of islands shown in Fig.37.
At $N_c \approx 5$ one particle reaches the chain of islands;
20 out of 64 particles have reached the chain of islands by $N_c = 100$.

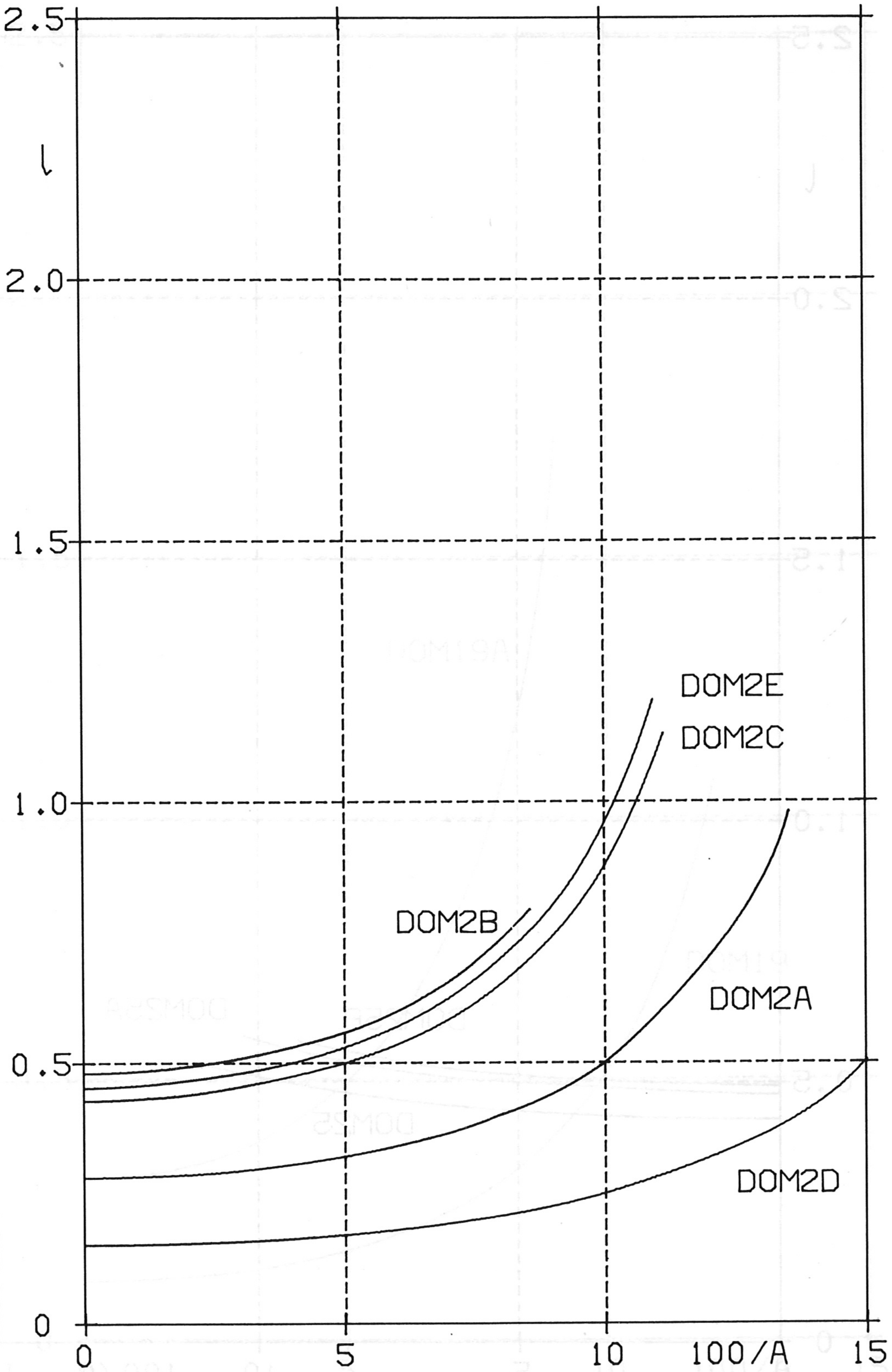

Fig.14: Twist ι versus 100/A for the ℓ = 2 stellarators of Table II with N = 10.

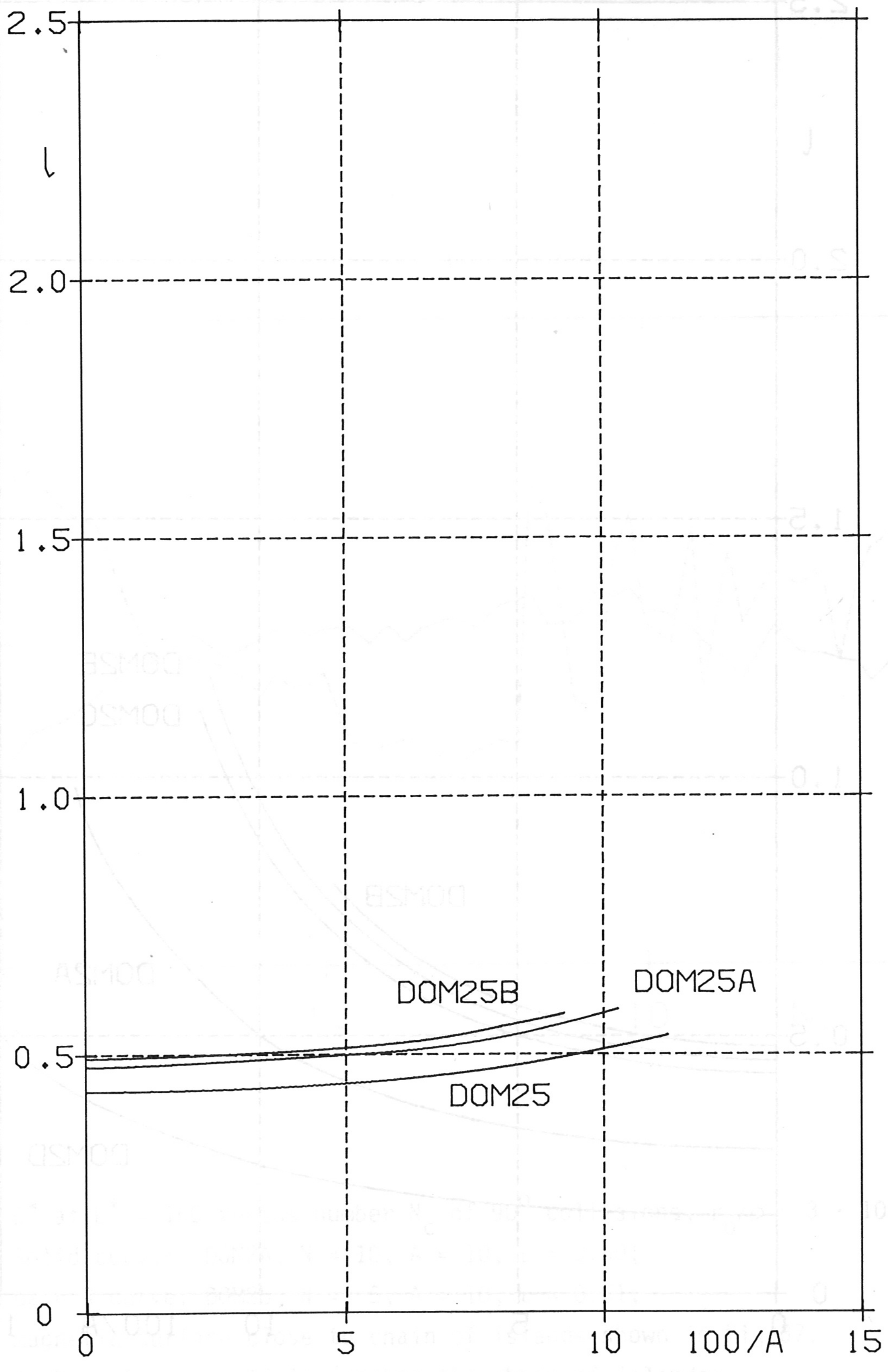

Fig.15: Twist ι versus 100/A for the ℓ = 2 stellarators of Table II with N = 5.

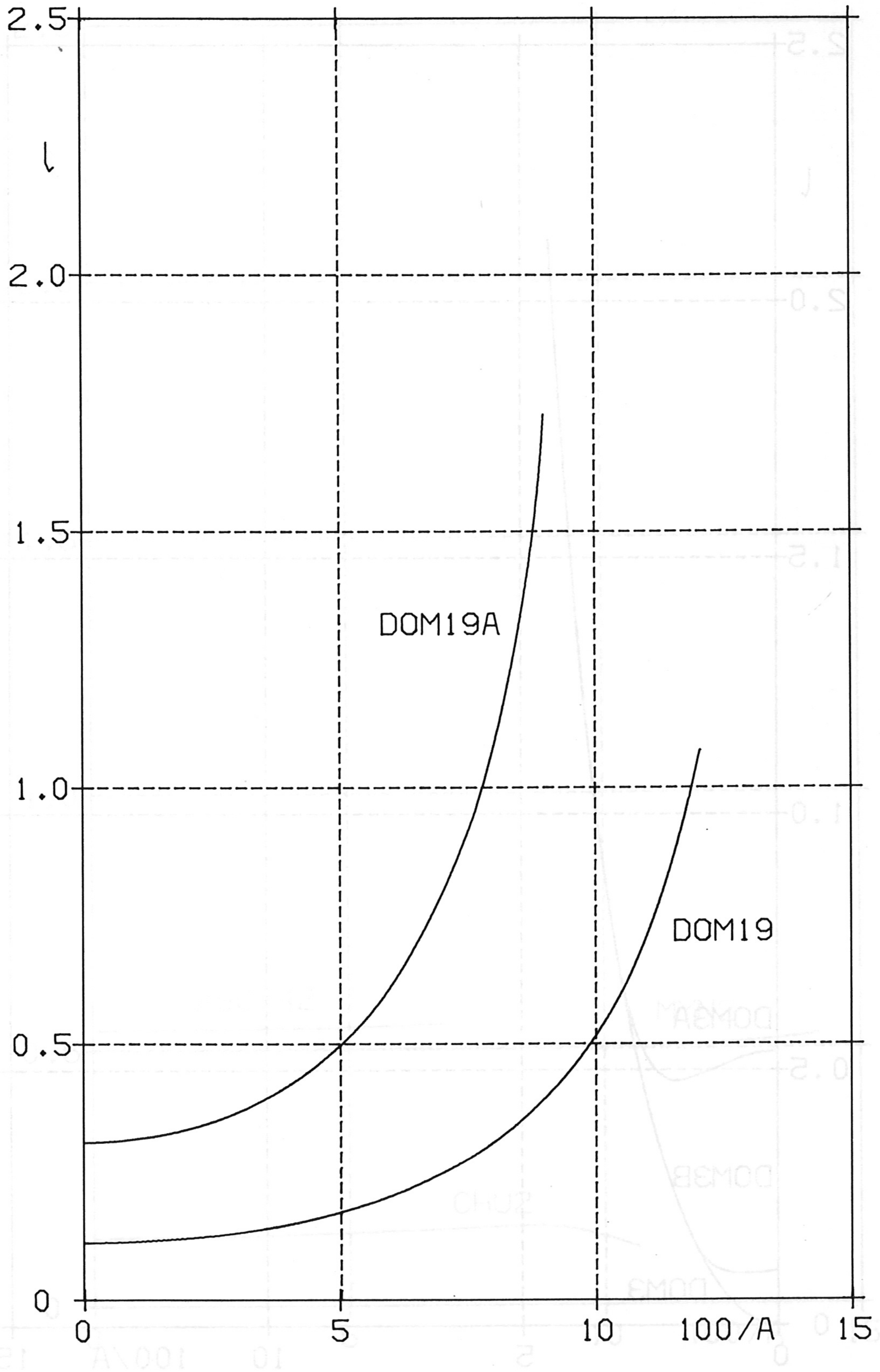

Fig.16: Twist ι versus 100/A for the ℓ = 2 stellarators of Table II with N = 19.

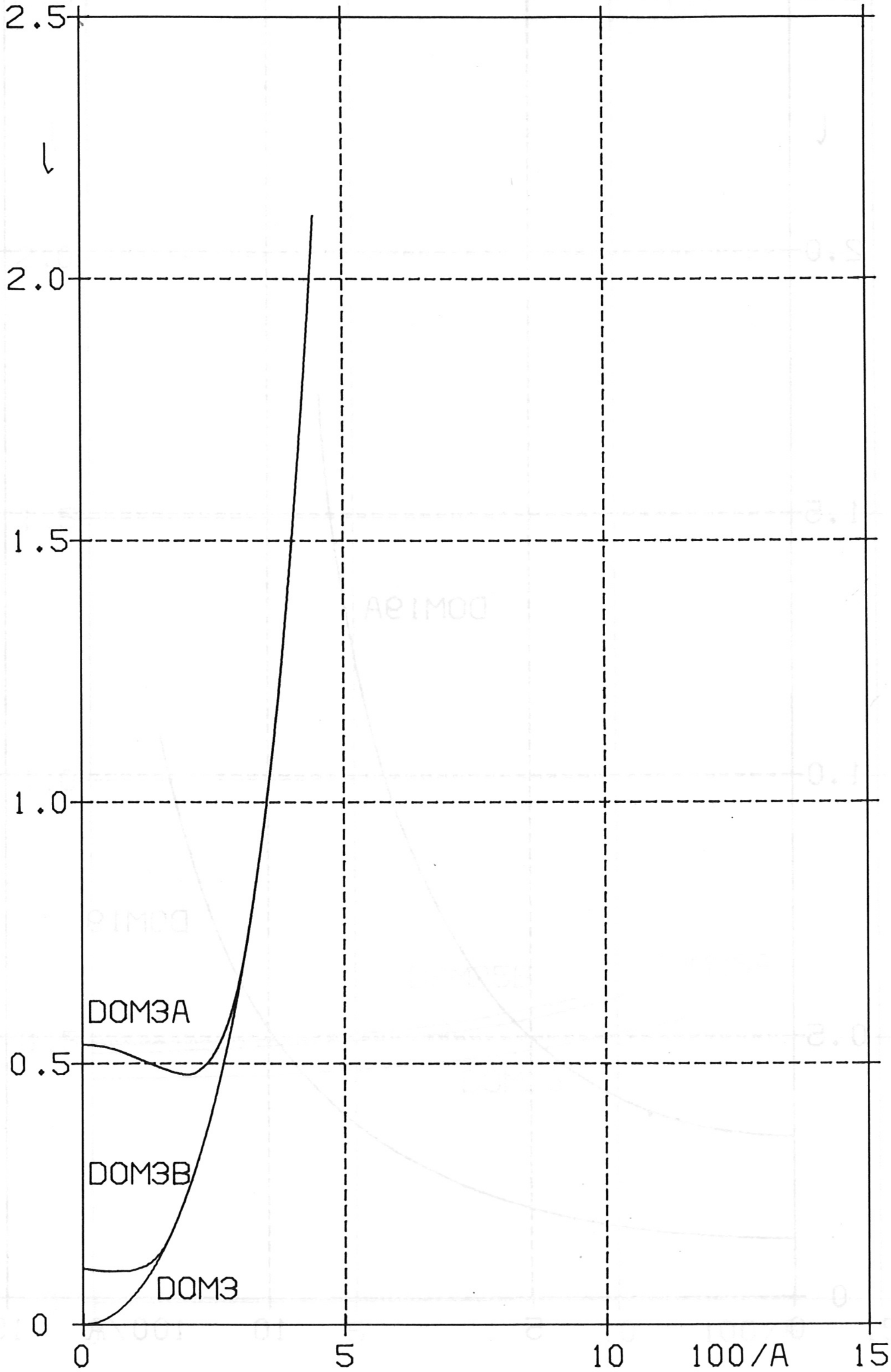

Fig.17: Twist ι versus 100/A for the ℓ = 3 stellarators of Table II (N = 32).

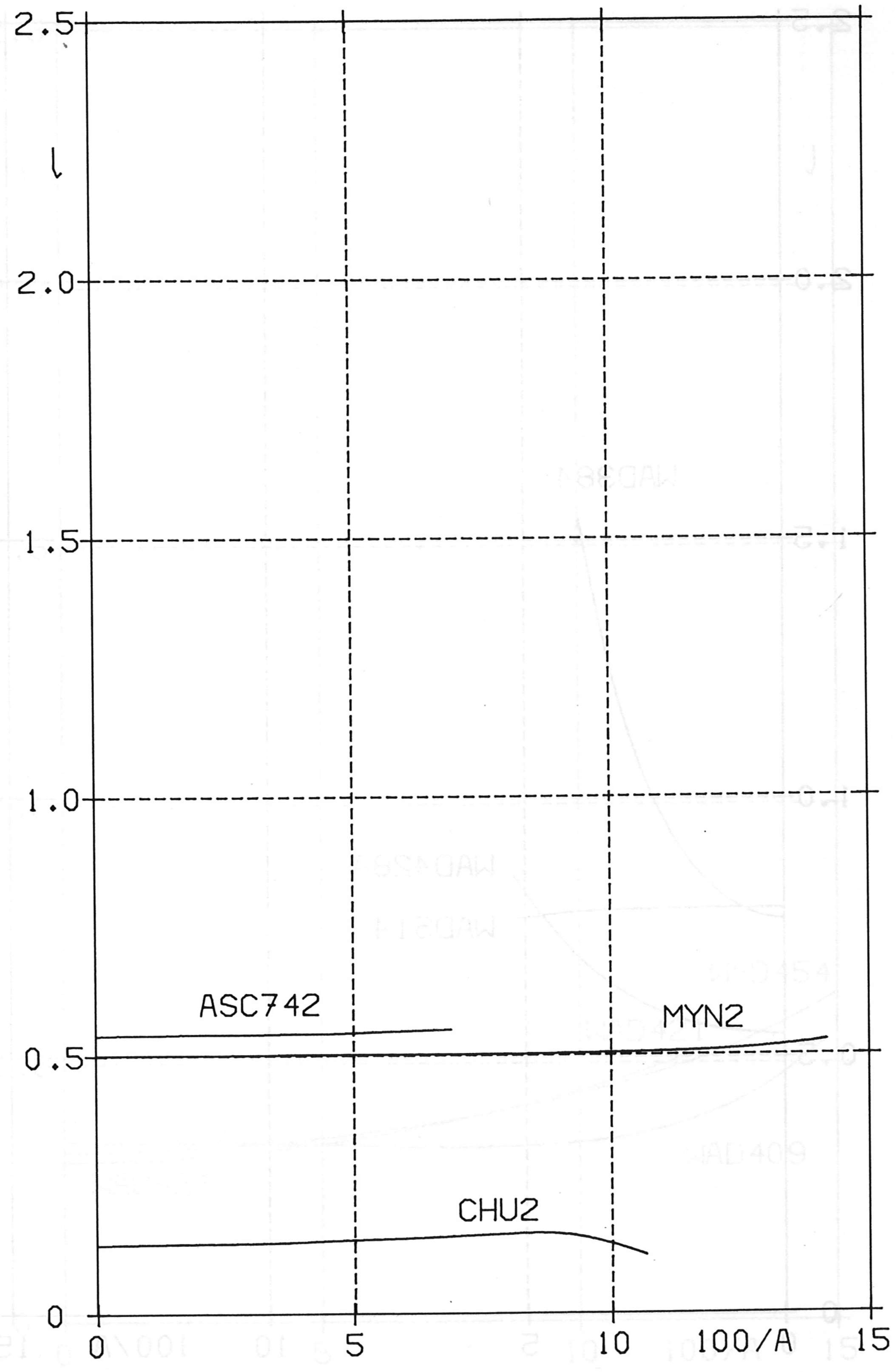

Fig.18: Twist ι versus 100/A for the configurations ASC742, CHU2, and MYN2 of Table III.

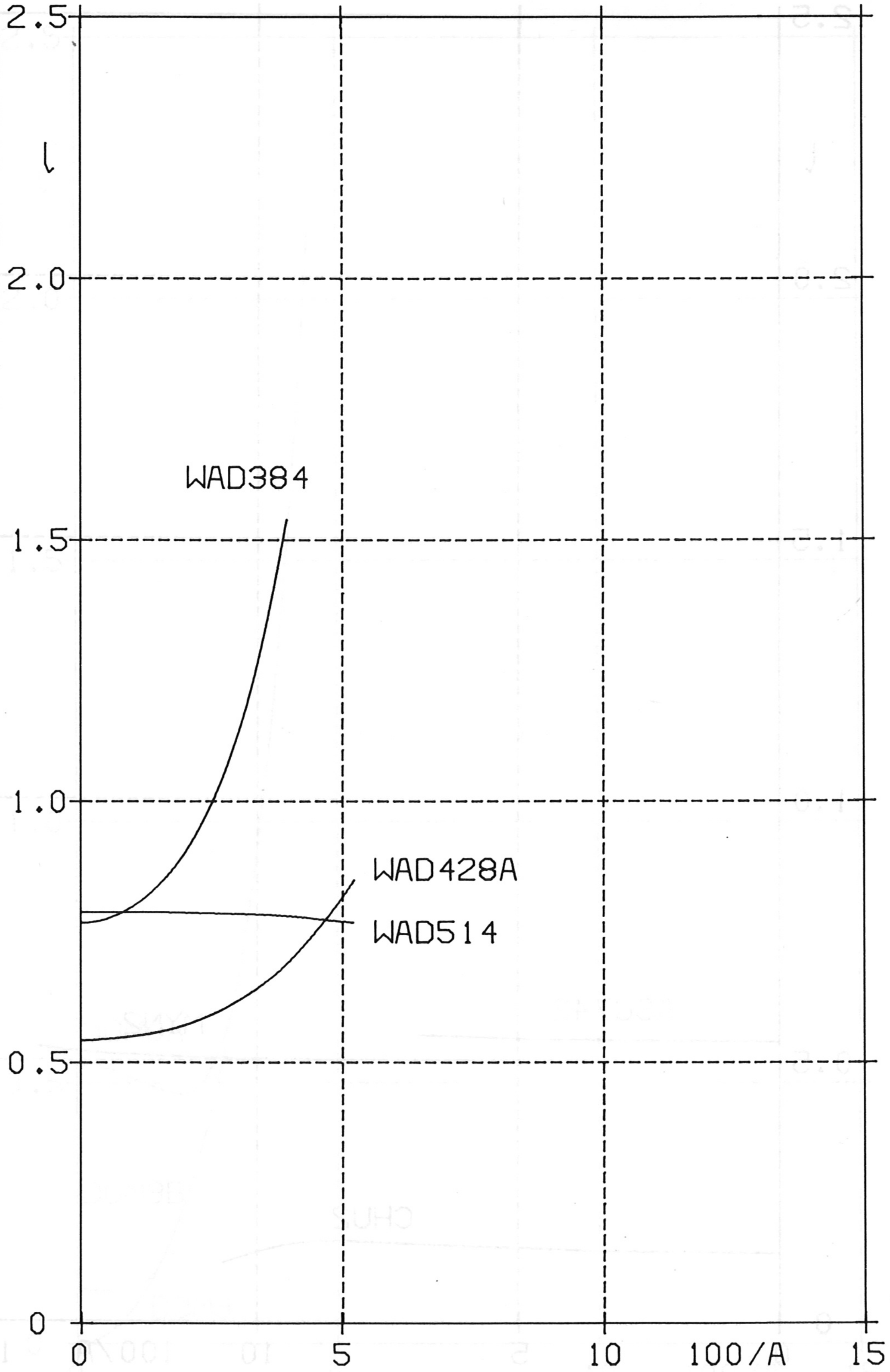

<u>Fig.19</u>: Twist ι versus 100/A for the configurations WAD384, WAD428A, and WAD514 of Table III.

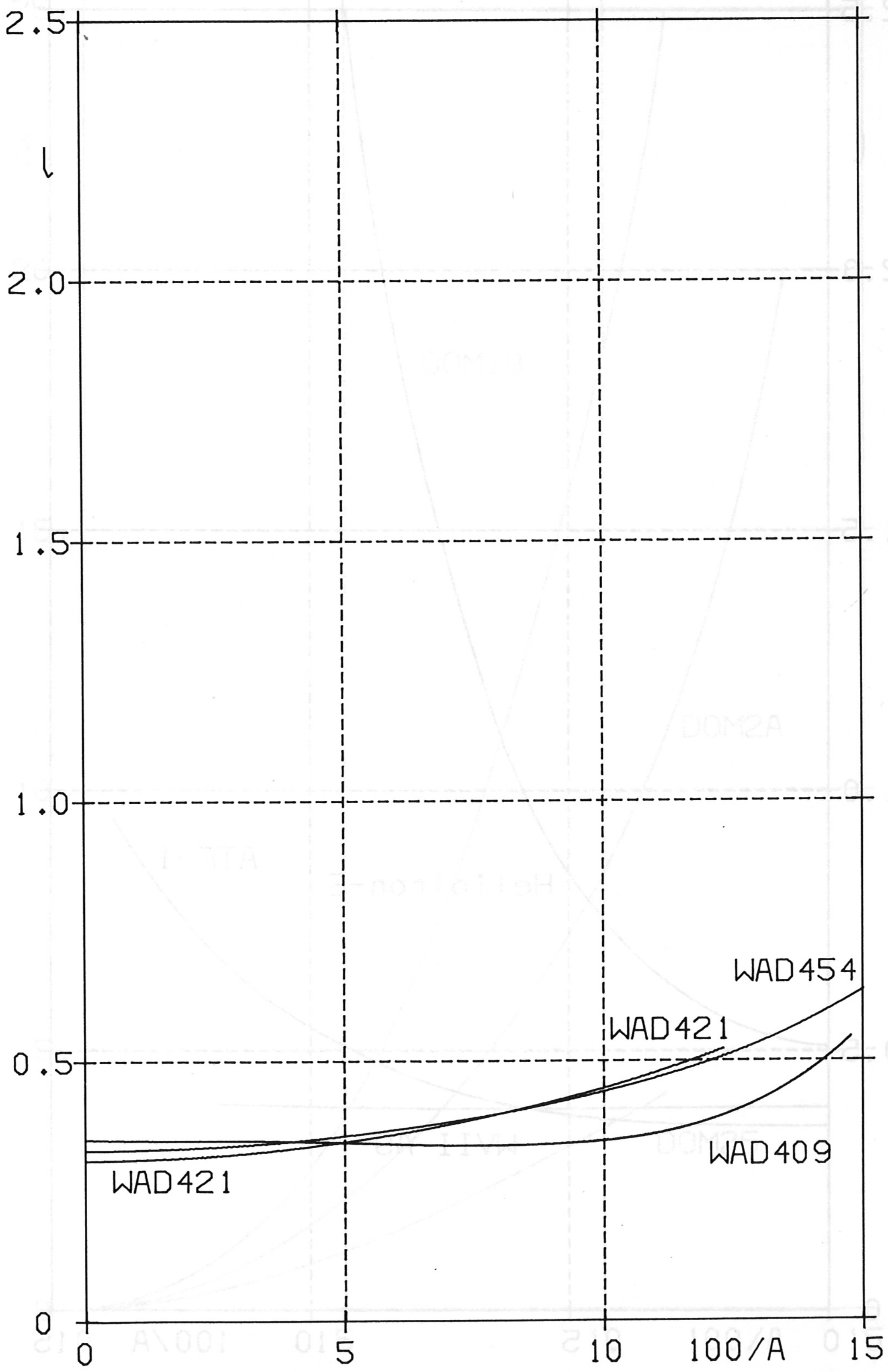

Fig.20: Twist ι versus 100/A for the configurations WAD409, WAD421, and WAD454 of Table III.

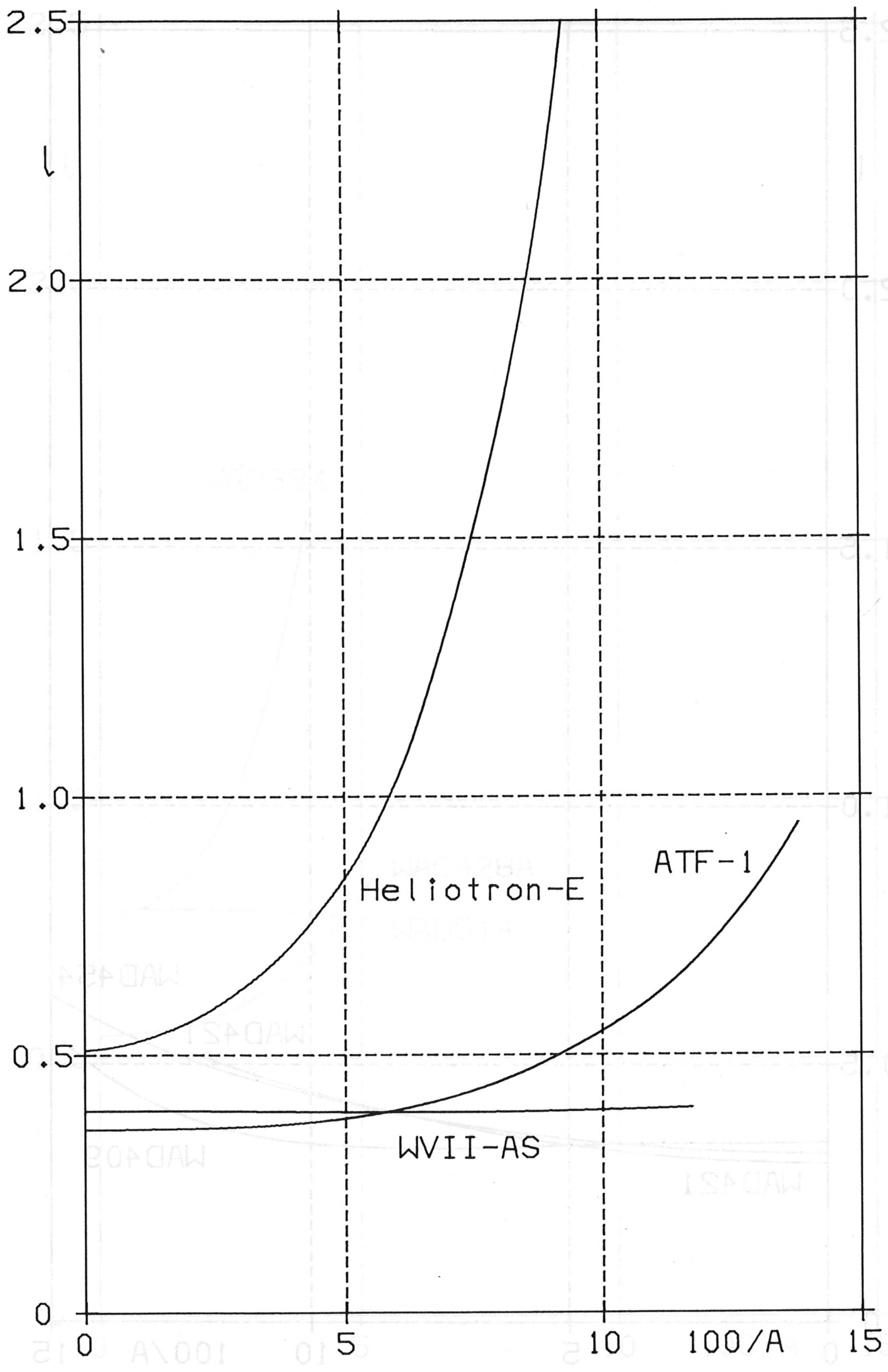

Fig.21: Twist ι versus 100/A for the configurations ATF-1, Heliotron-E, and W VII-AS of Table III.

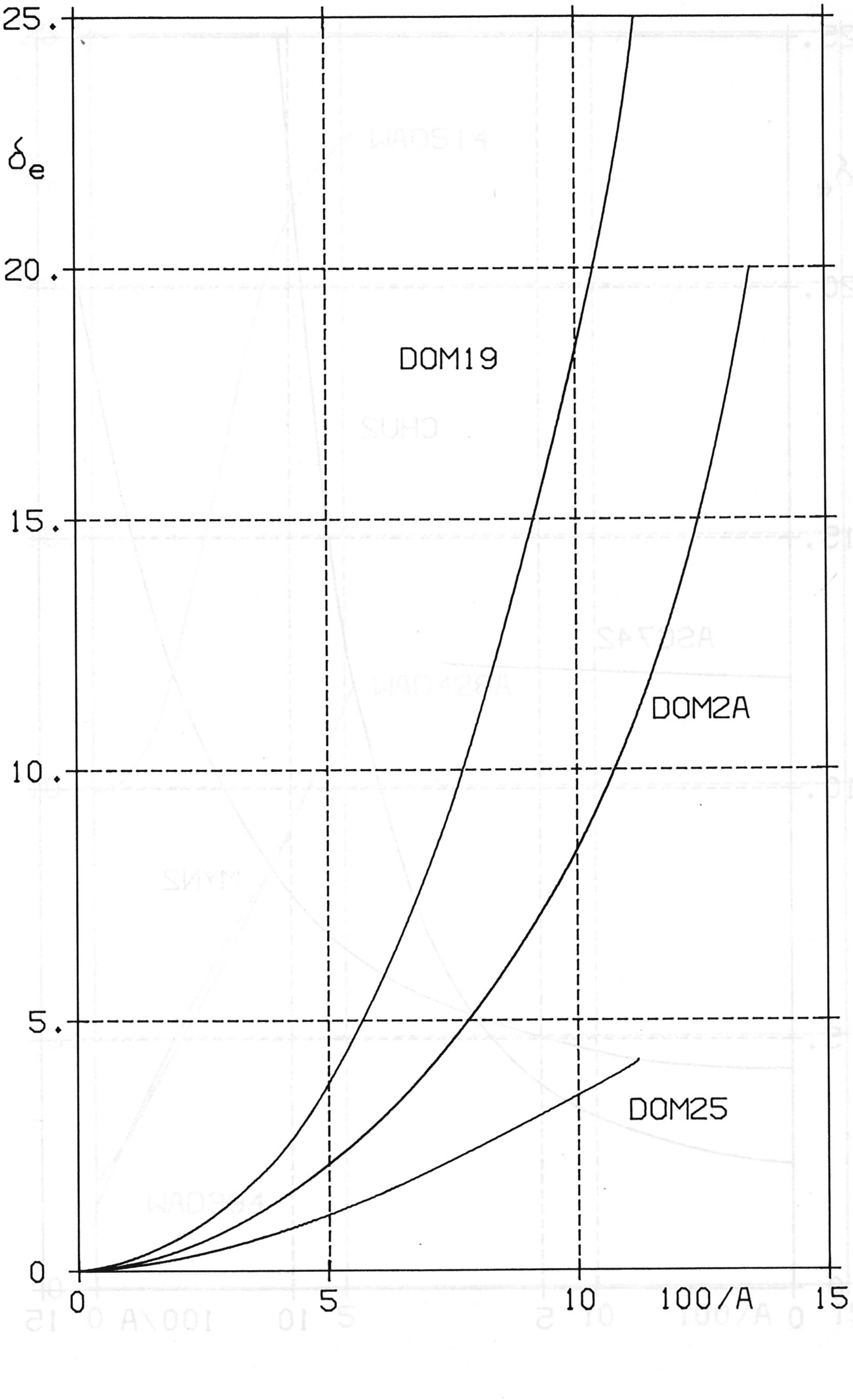

Fig.22: Effective ripple δ_e (in %) versus 100/A for the ℓ = 2 stellarators DOM2A, DOM25, and DOM19 of Table II.

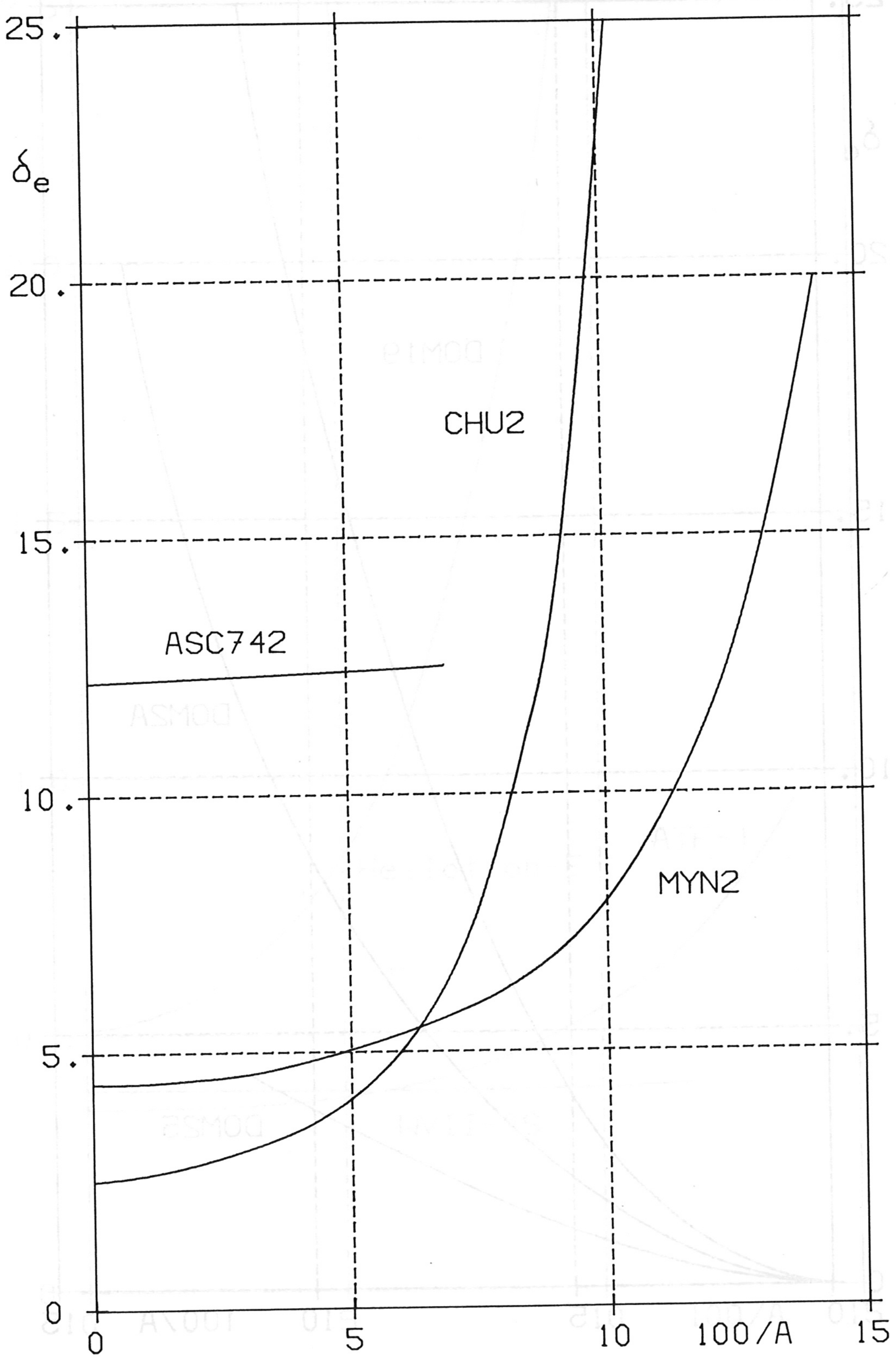

Fig.23: Effective ripple δ_e (in %) versus 100/A for the configurations ASC742, CHU2, and MYN2 of Table III.

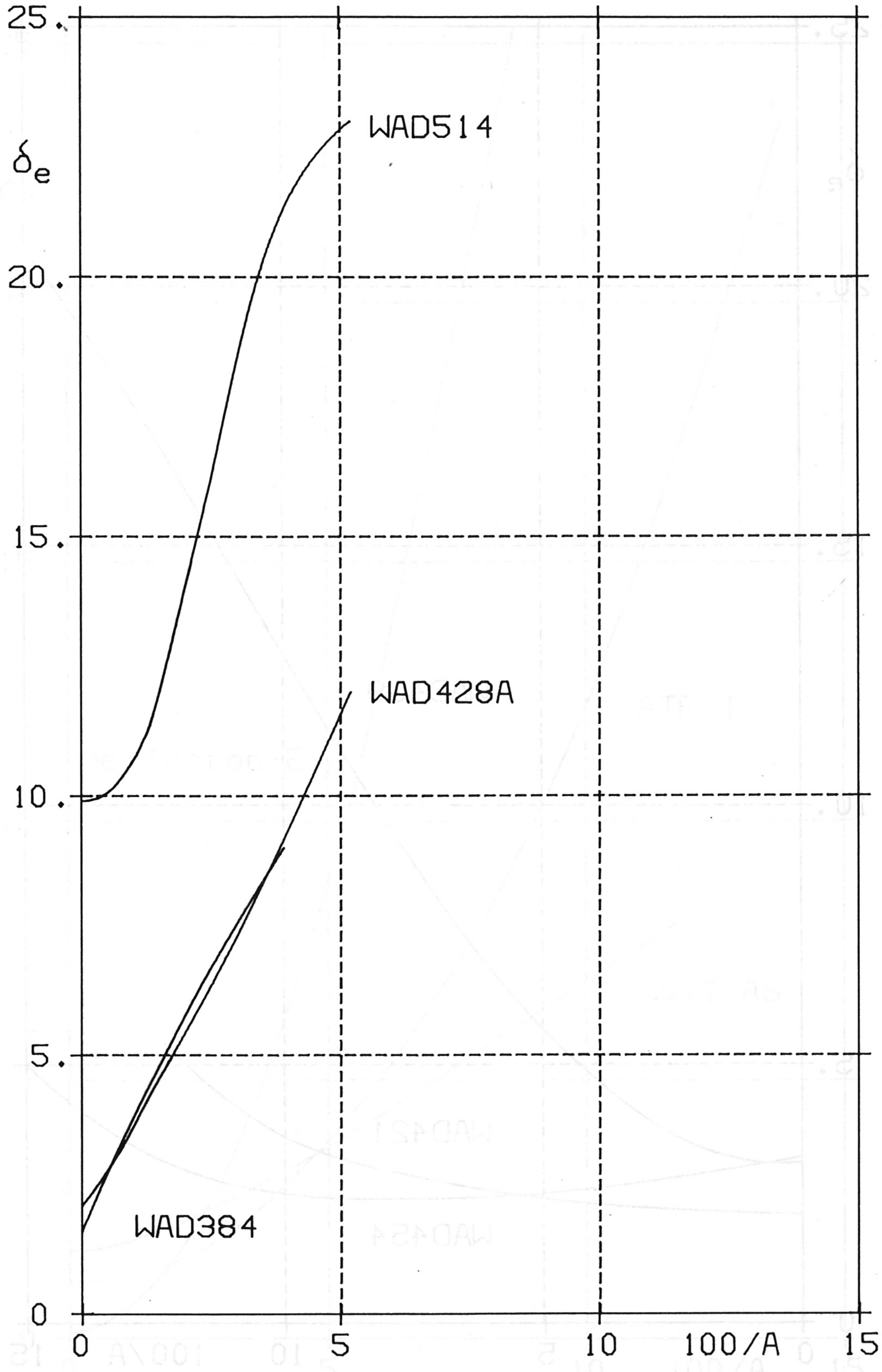

Fig.24: Effective ripple δ_e (in %) versus 100/A for the configurations WAD384, WAD428A, and WAD514 of Table III.

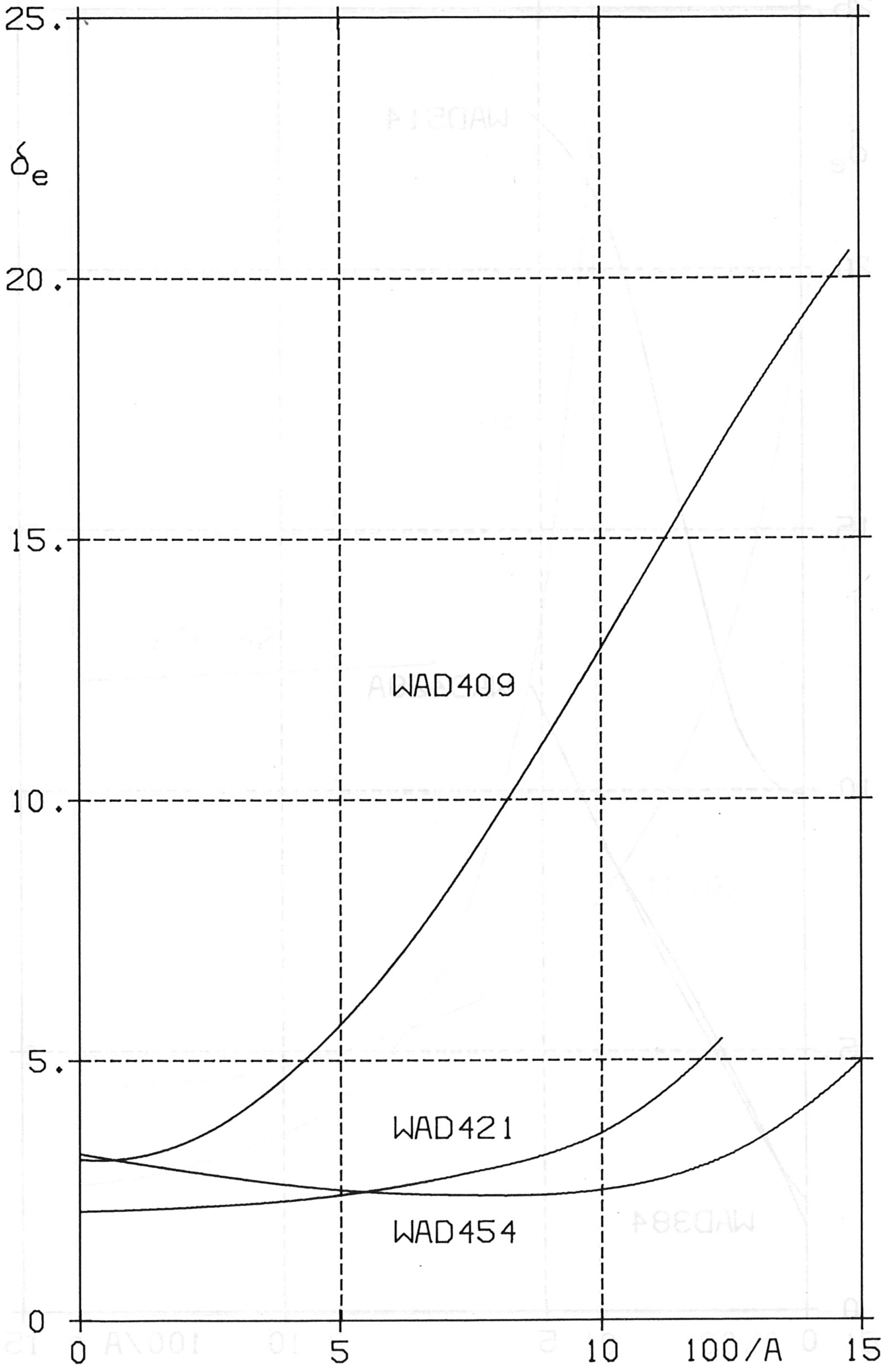

Fig.25: Effective ripple δ_e (in %) versus 100/A for the configurations WAD409, WAD421, and WAD454 of Table III.

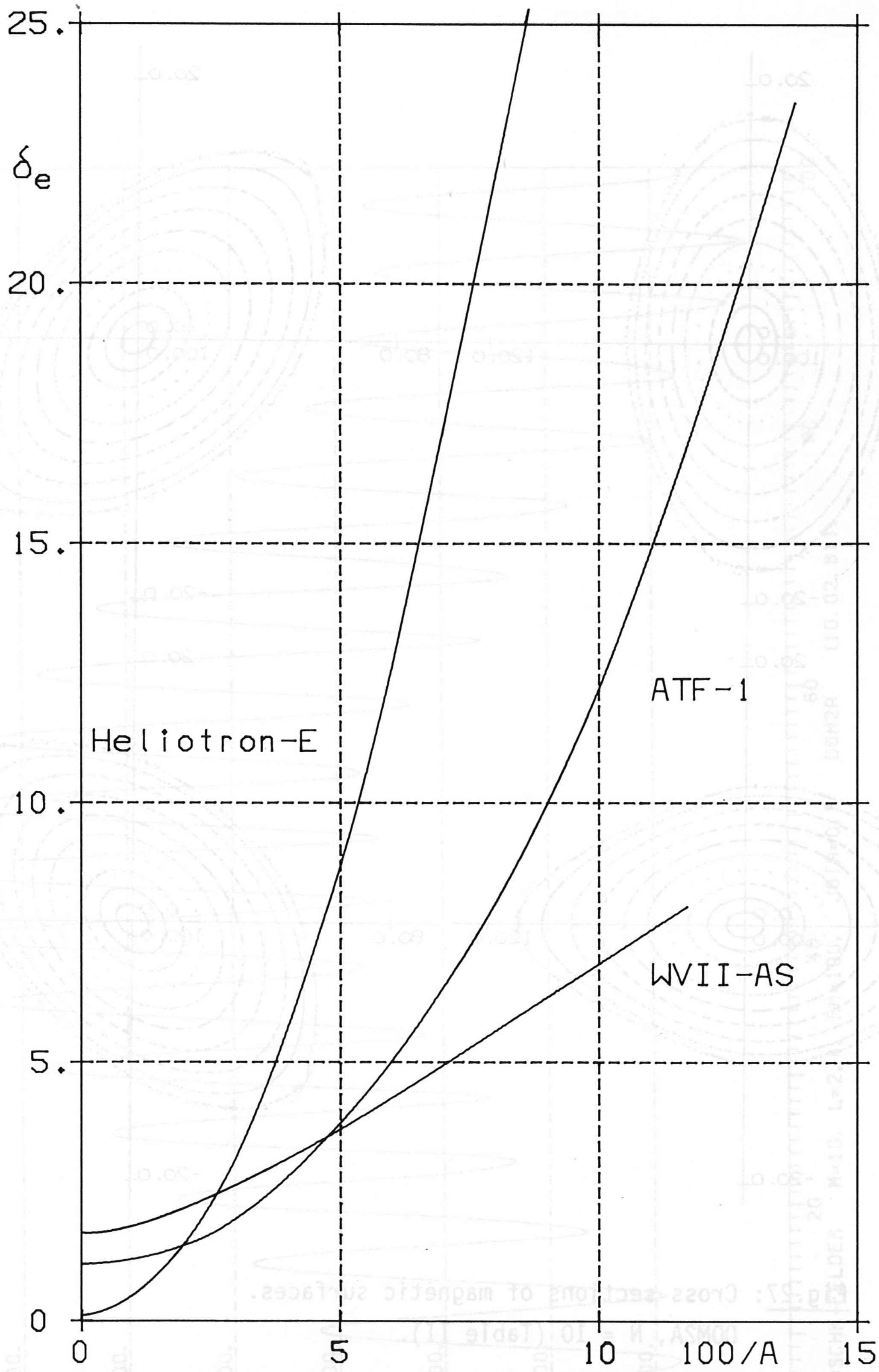

Fig.26: Effective ripple δ_e (in %) versus 100/A for the configurations ATF-1, Heliotron-E, and W VII-AS of Table III.

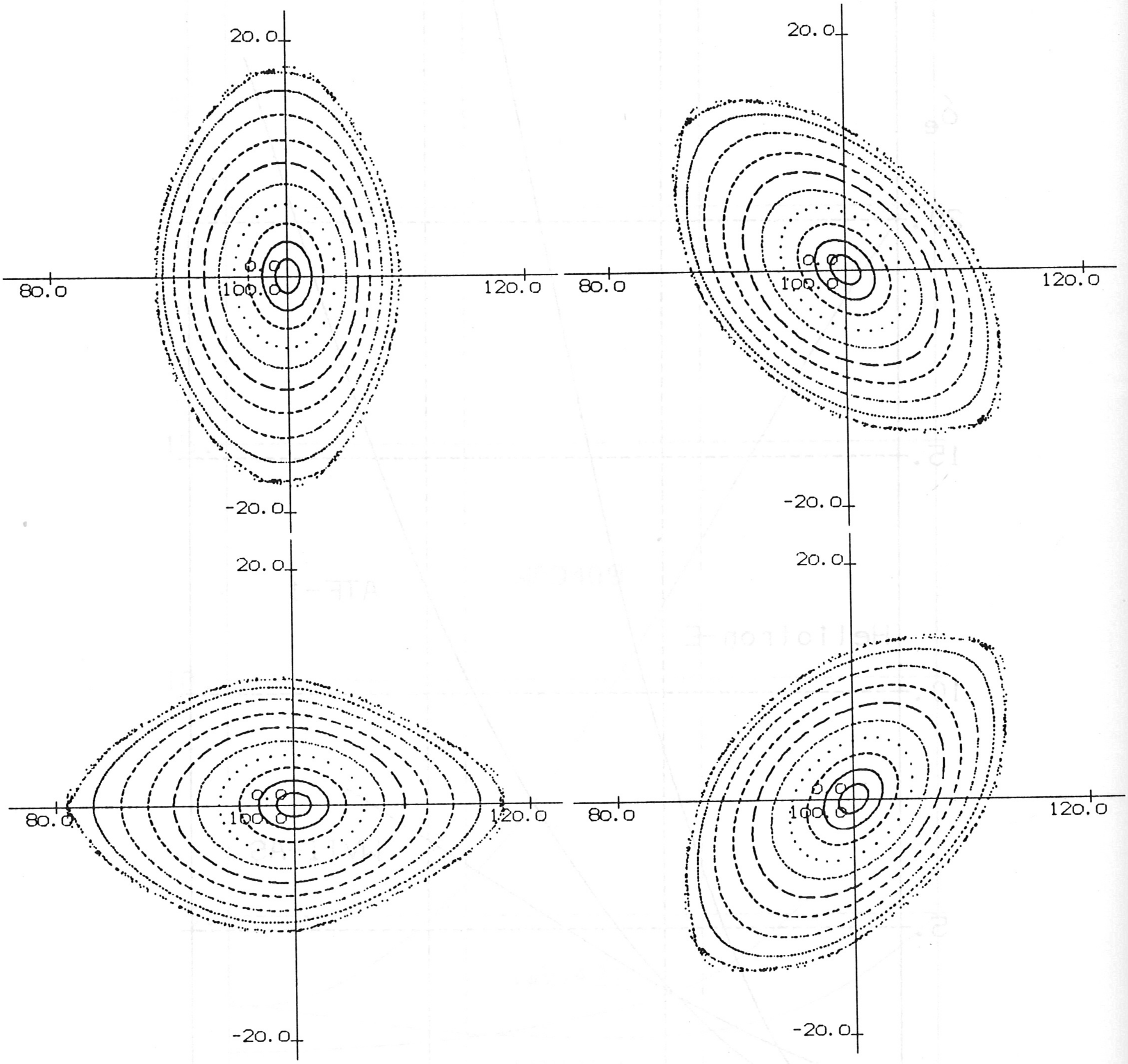

Fig.27: Cross sections of magnetic surfaces.
DOM2A, N = 10 (Table II).

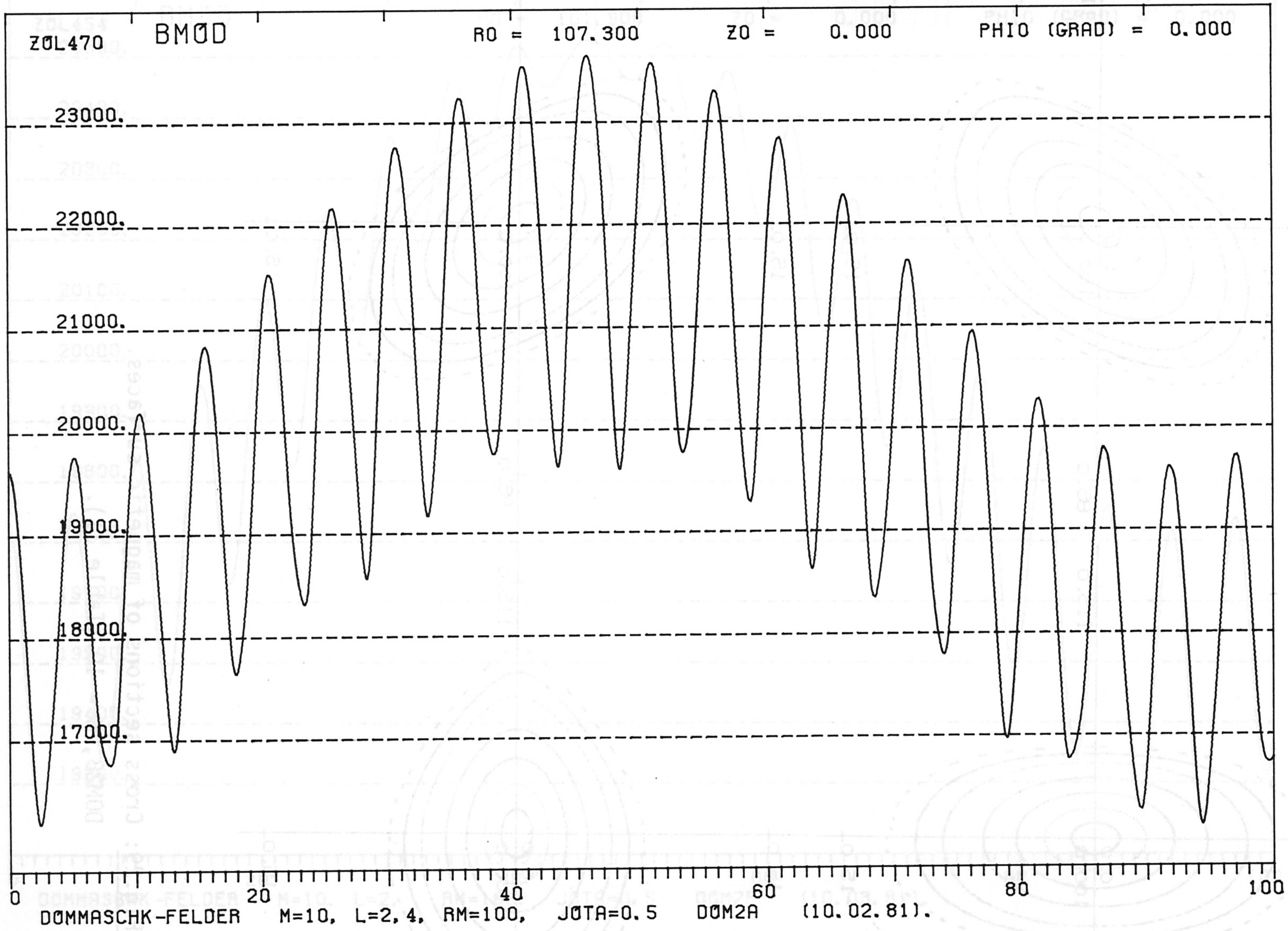

Fig.28: Magnitude of magnetic field along a field line.

DOM2A, N = 10, A = 10, ι = 0.50.

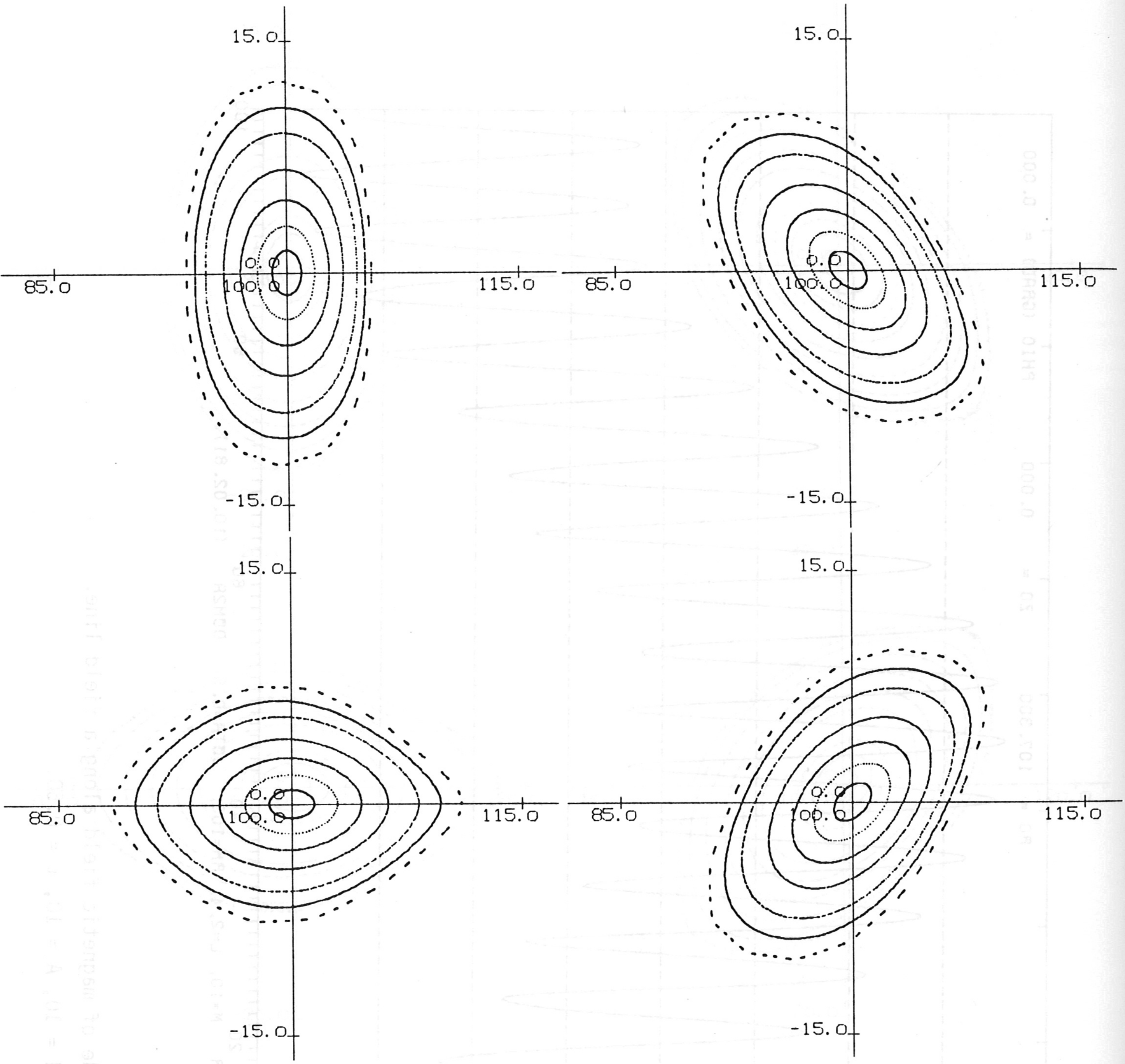

Fig.29: Cross sections of magnetic surfaces.
DOM2B, N = 10 (Table II).

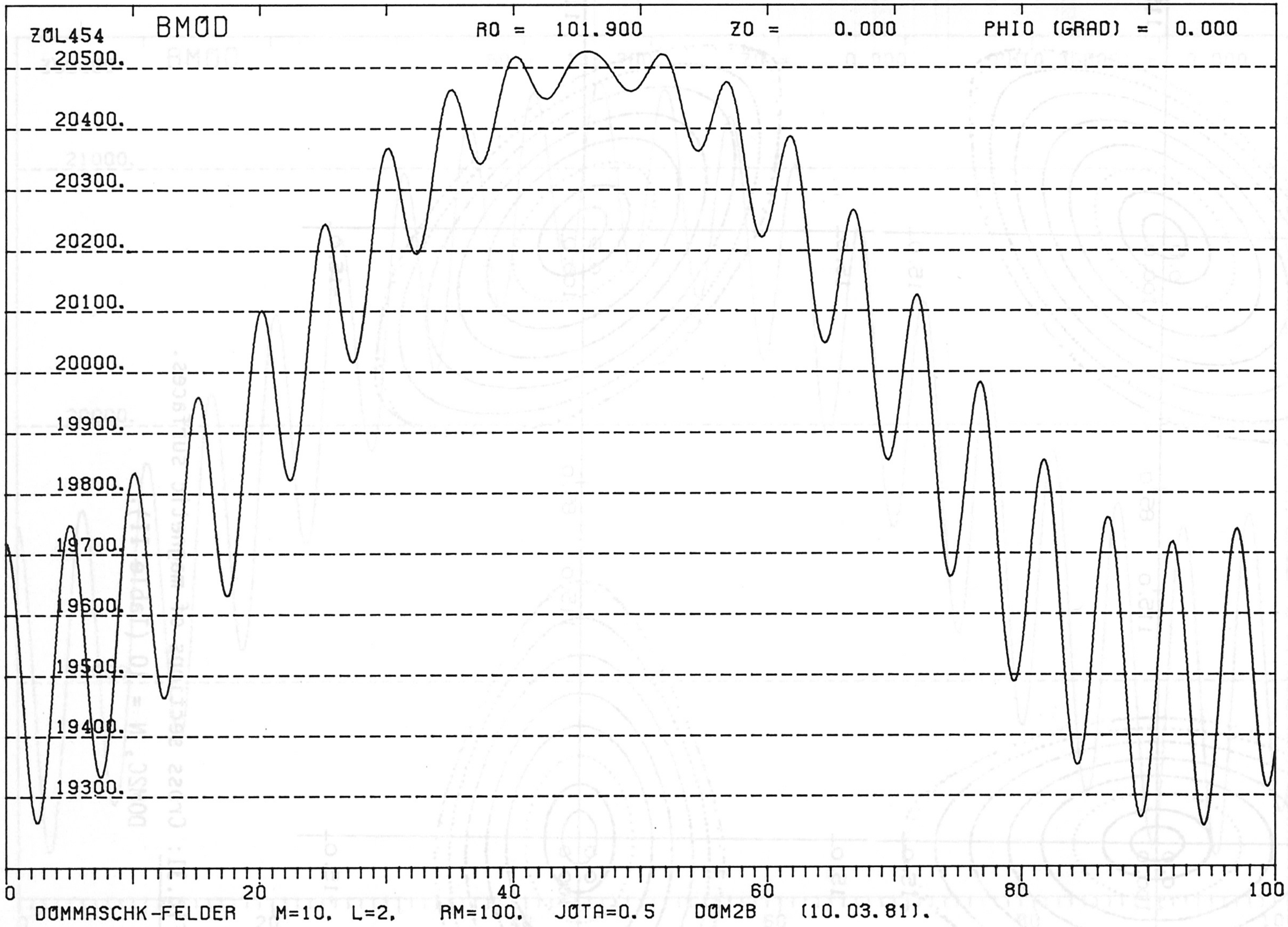

Fig.30: Magnitude of magnetic field along a field line.
DOM2B, N = 10, A = 40, ι = 0.50.

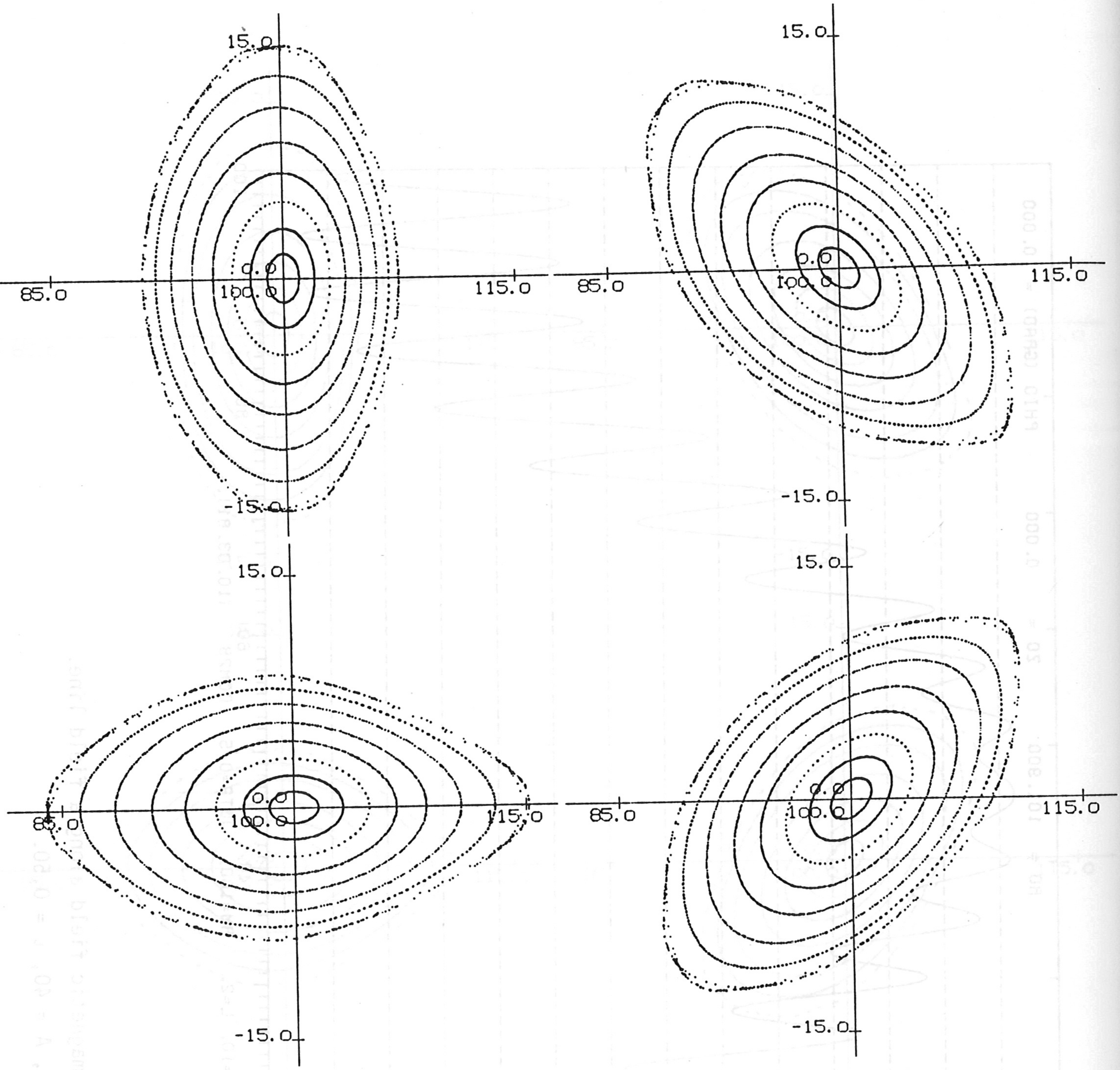

Fig.31: Cross sections of magnetic surfaces.
DOM2C, N = 10 (Table II).

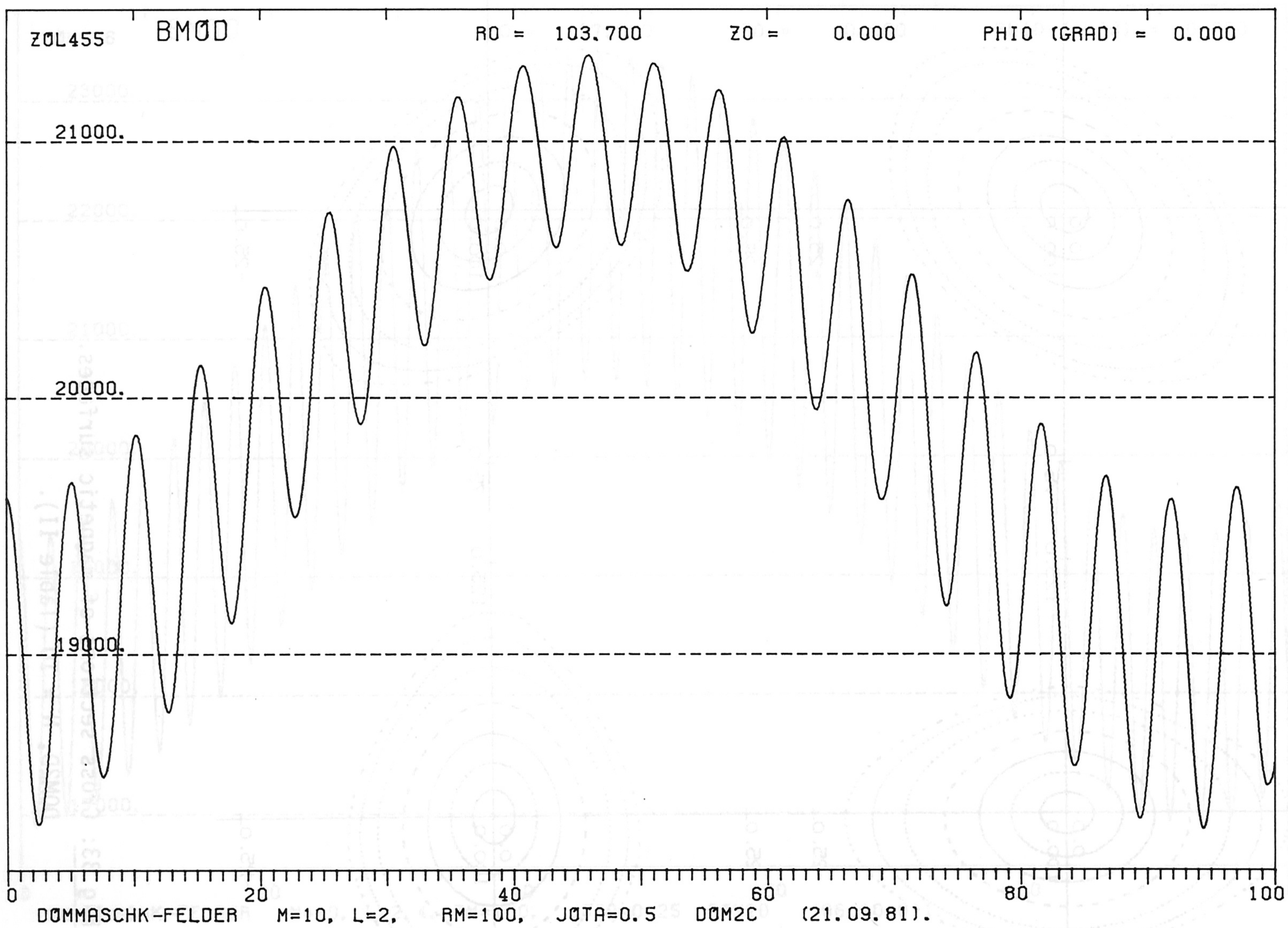

Fig.32: Magnitude of magnetic field along a field line.
DOM2C, N = 10, A = 20, ι = 0.50.

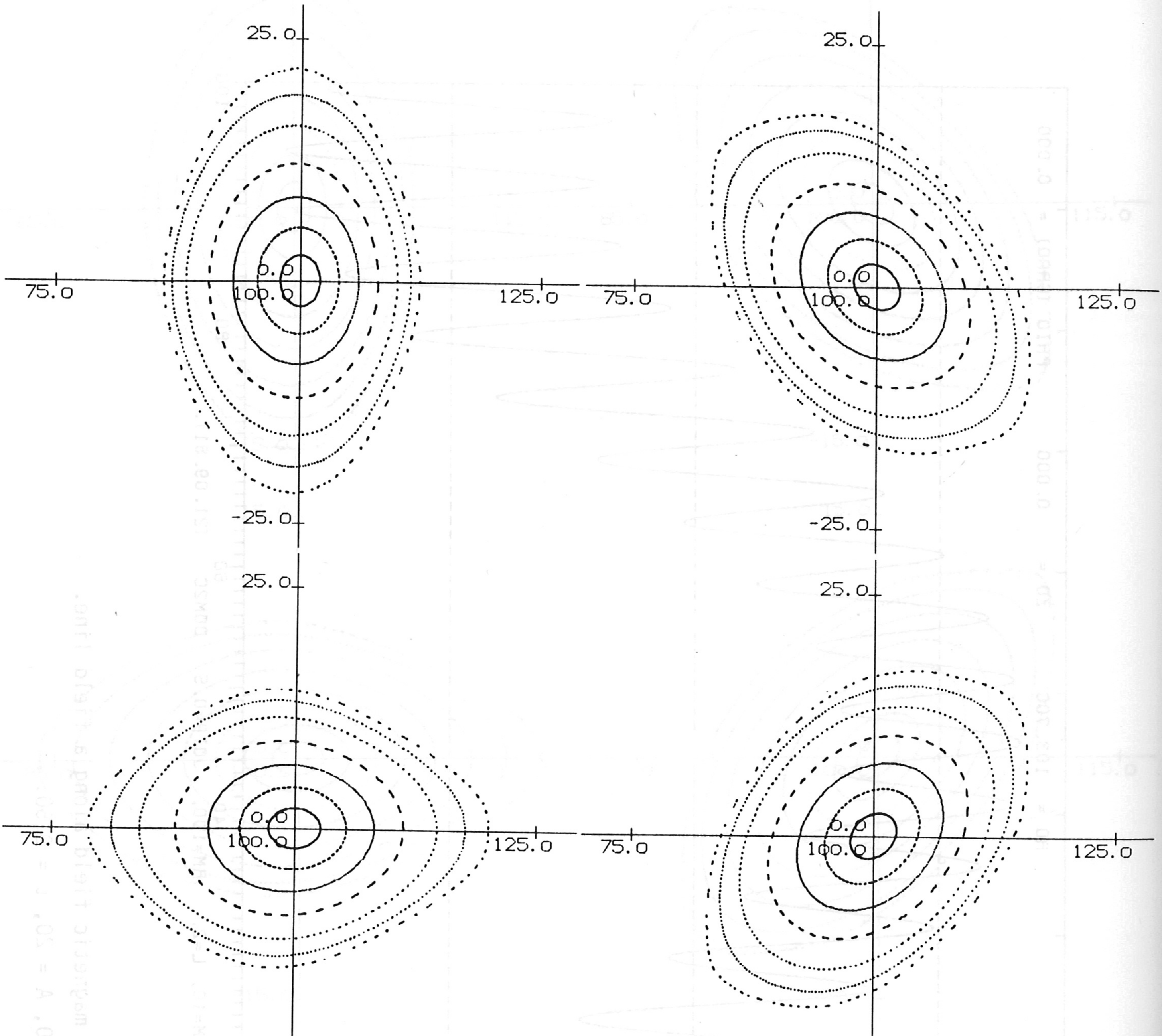

Fig.33: Cross sections of magnetic surfaces.
DOM2D, N = 10 (Table II).

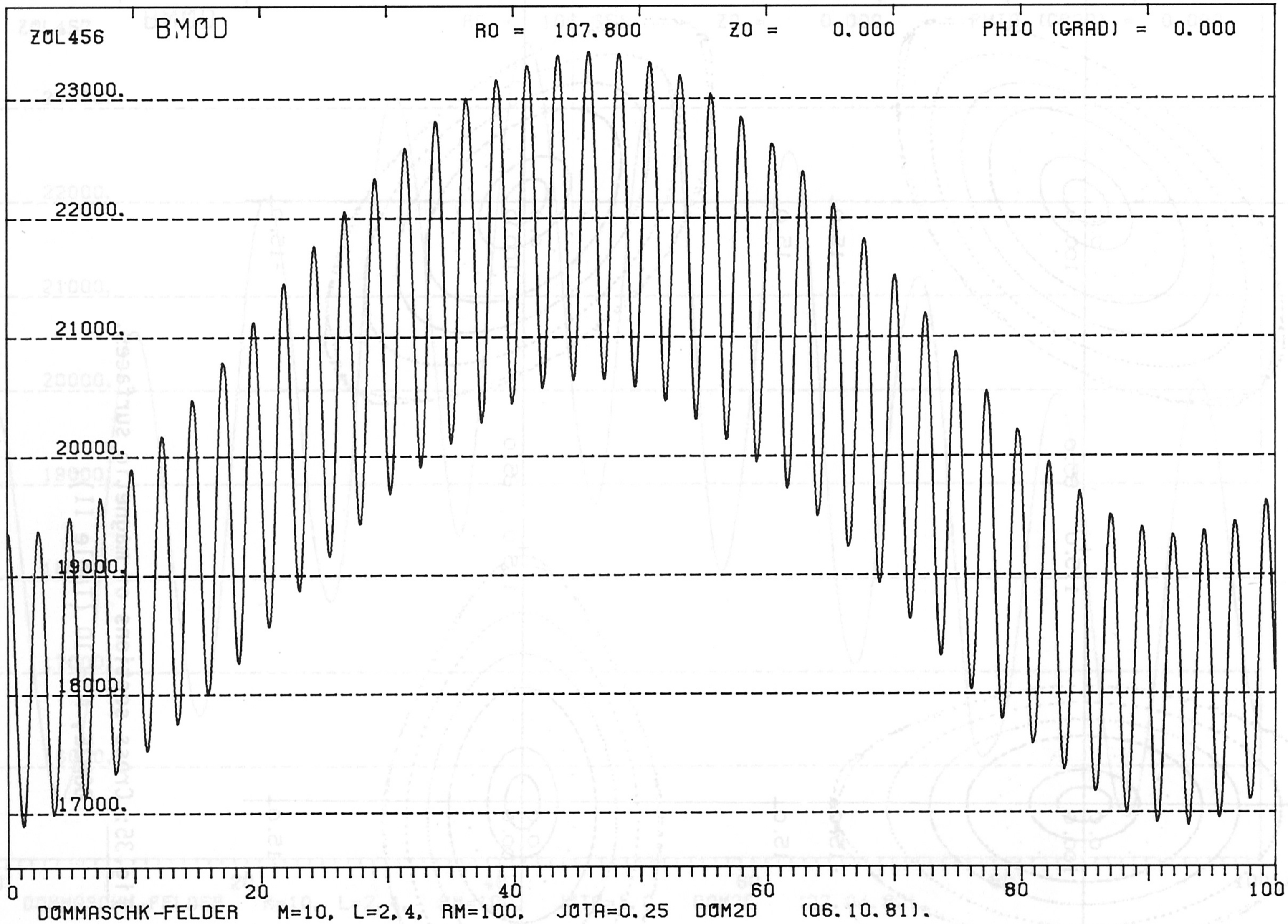

Fig.34: Magnitude of magnetic field along a field line.
DOM2D, $N = 10$, $A = 10$, $\iota = 0.25$.

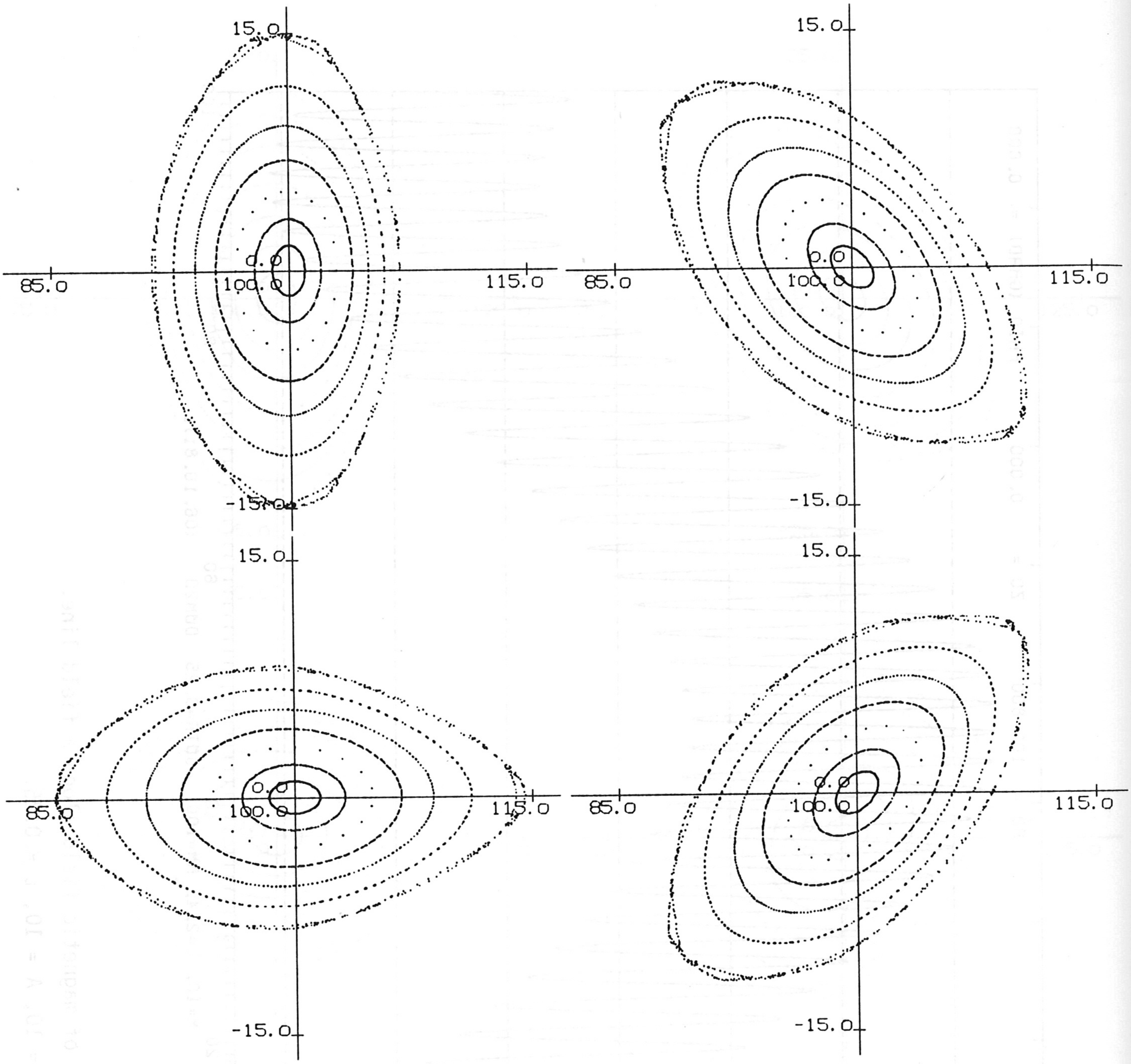

Fig.35: Cross sections of magnetic surfaces. DOM2E, N = 10 (Table II).

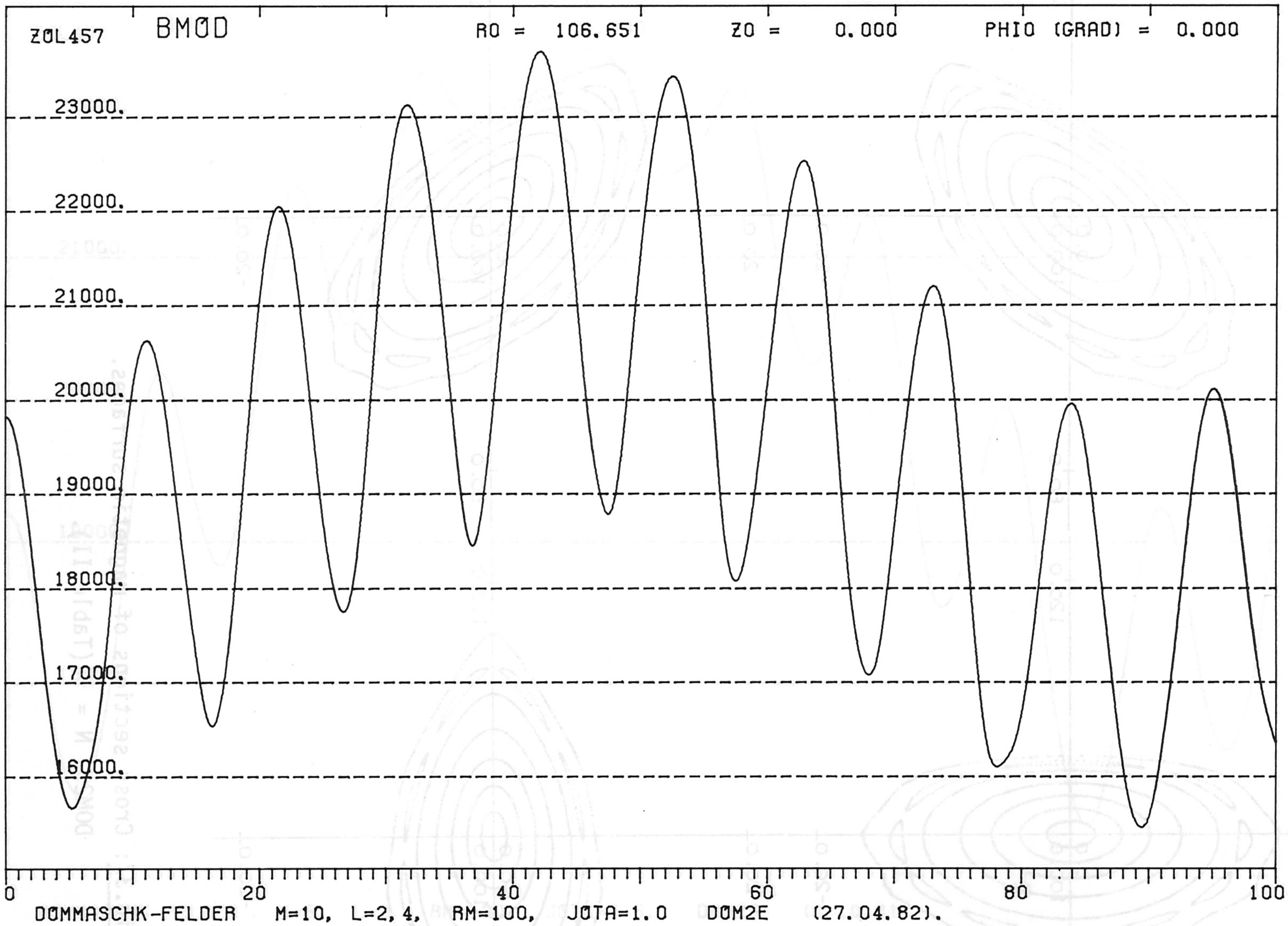

Fig.36: Magnitude of magnetic field along a field line.
DOM2E, N = 10, A = 10, ι = 0.96.

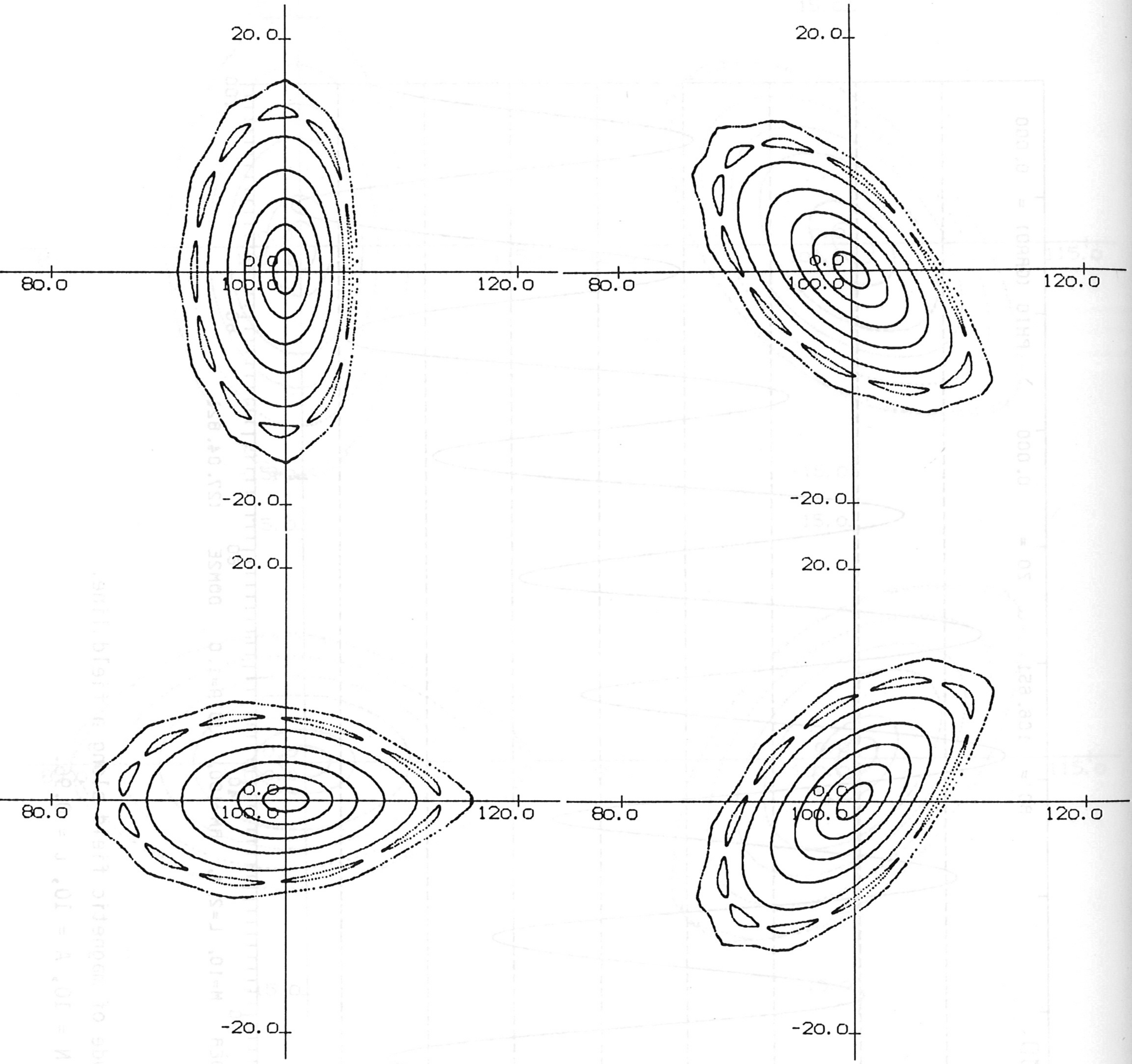

Fig.37: Cross sections of magnetic surfaces.
DOM25, N = 5 (Table II).

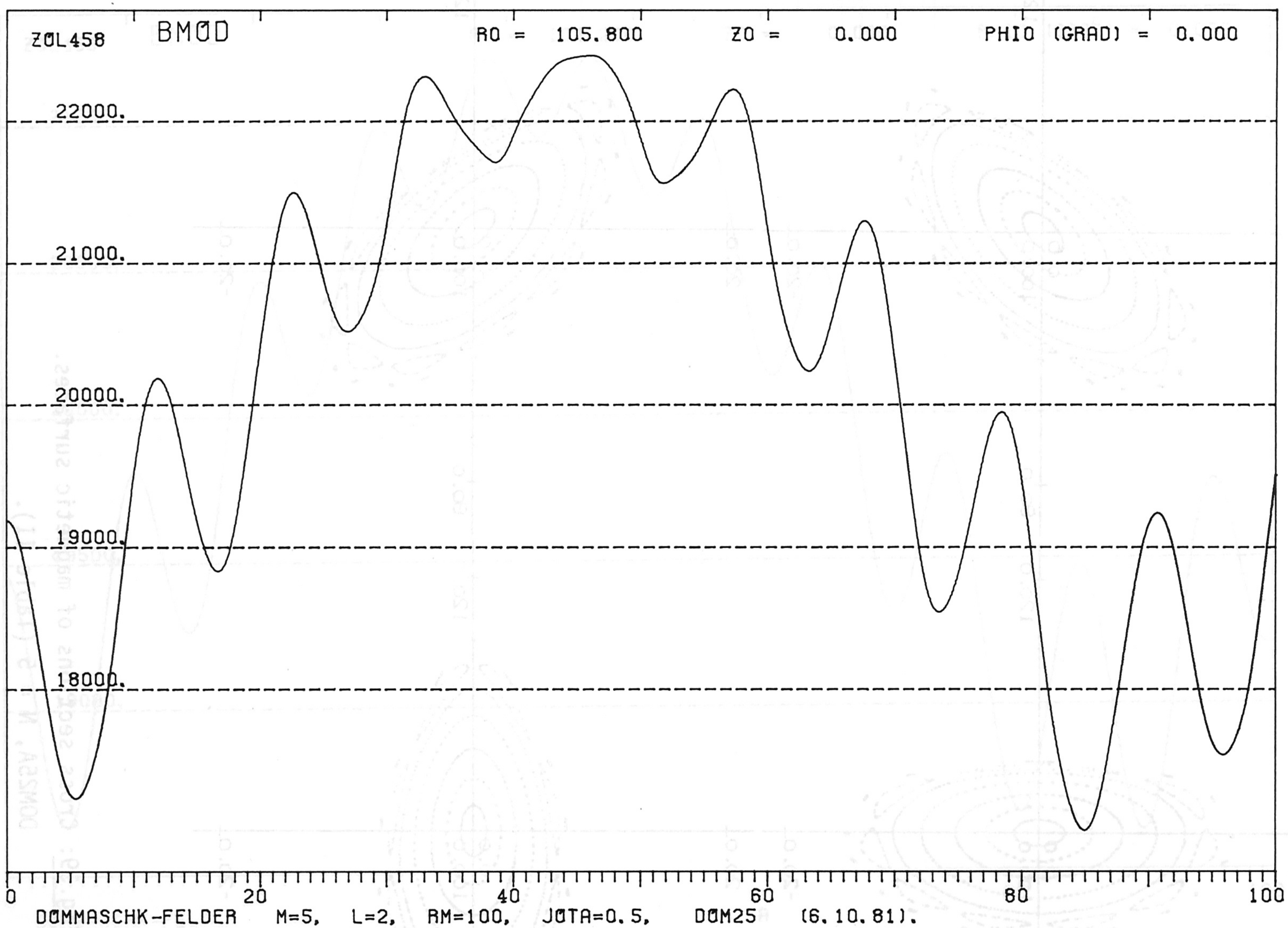

Fig.38: Magnitude of magnetic field along a field line.
DOM25, N = 5, A = 10, ι = 0.51.

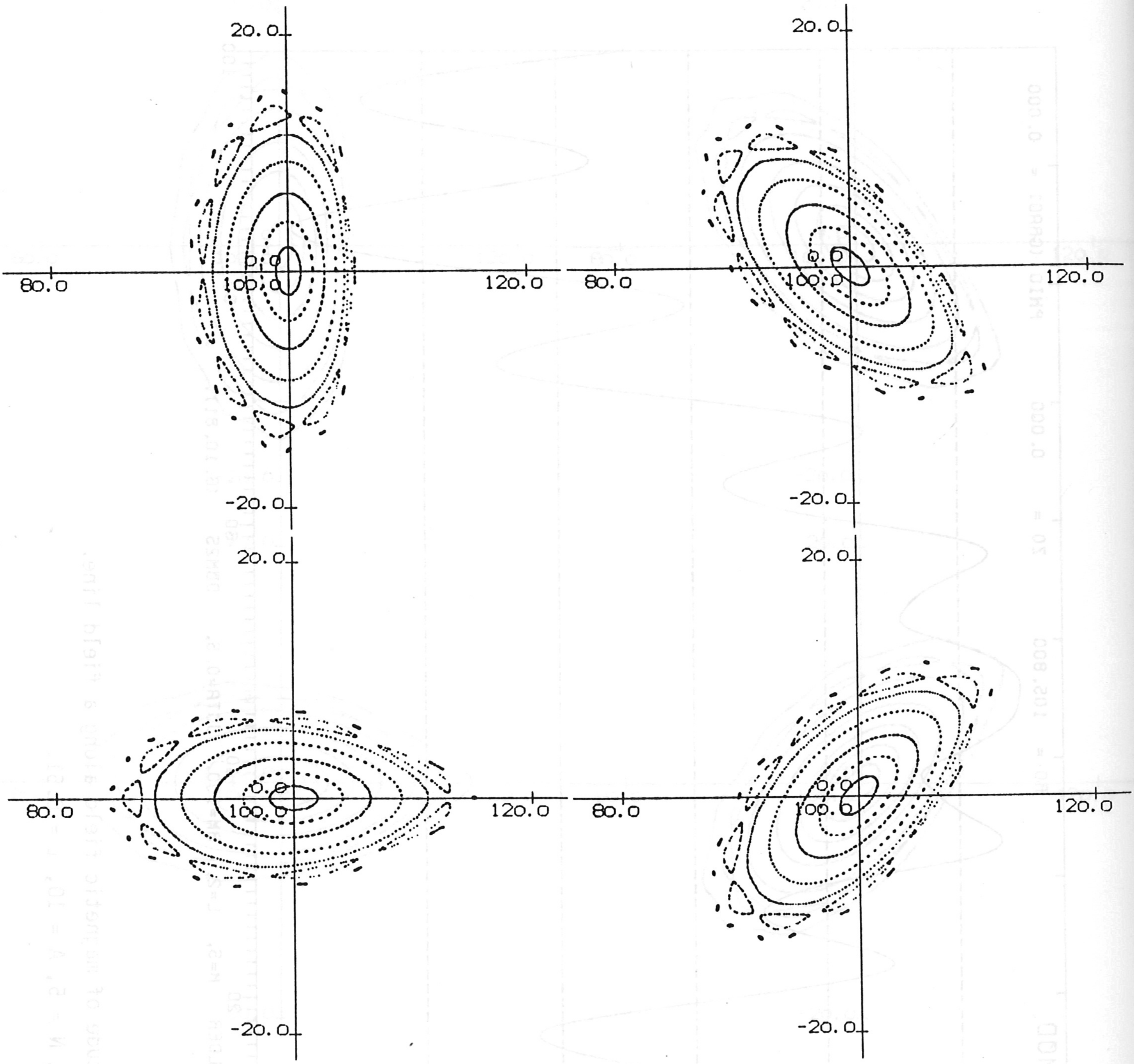

Fig.39: Cross sections of magnetic surfaces.
DOM25A, N = 5 (Table II).

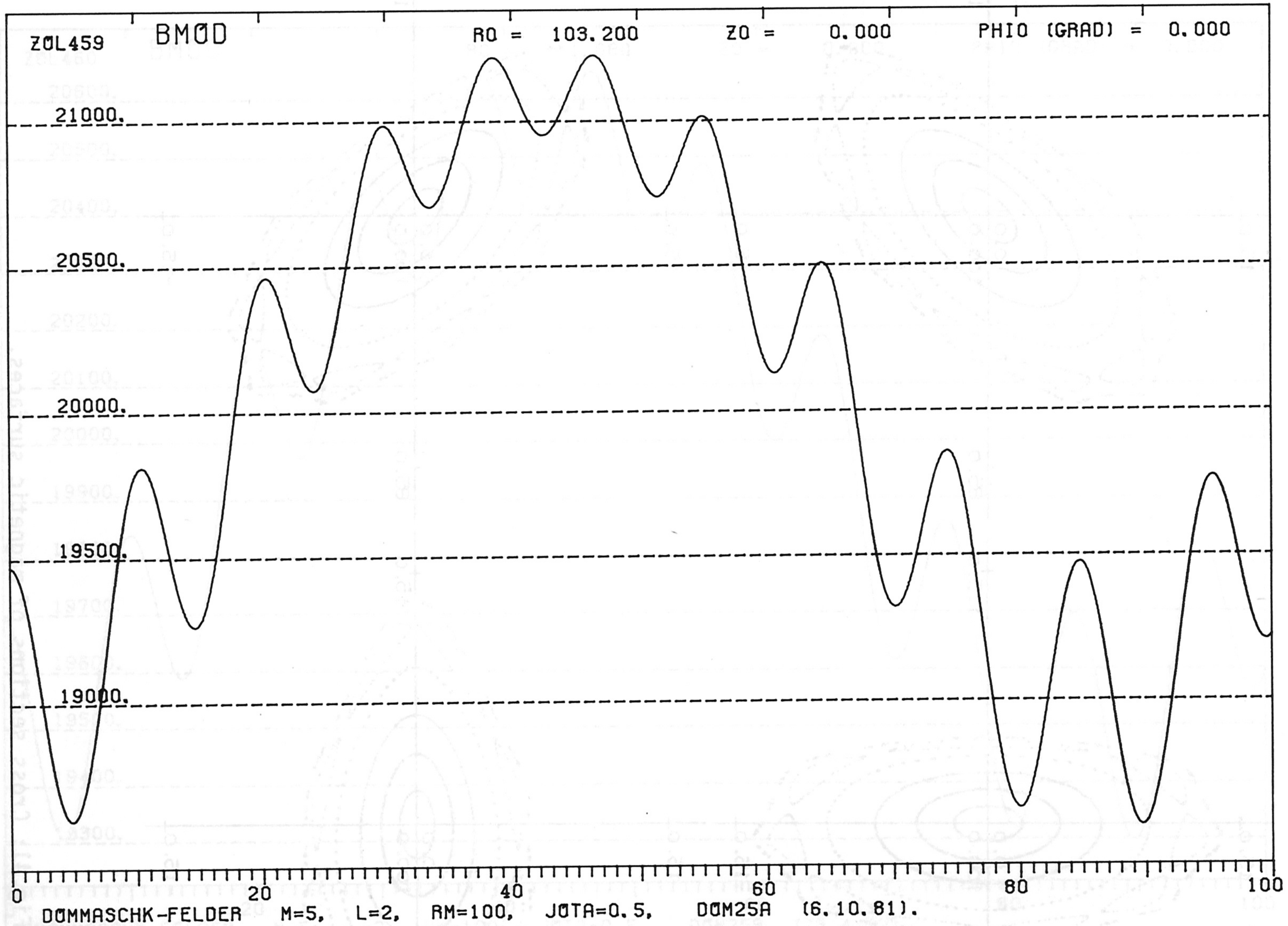

Fig.40: Magnitude of magnetic field along a field line.
DOM25A, N = 5, A = 20, ι = 0.50.

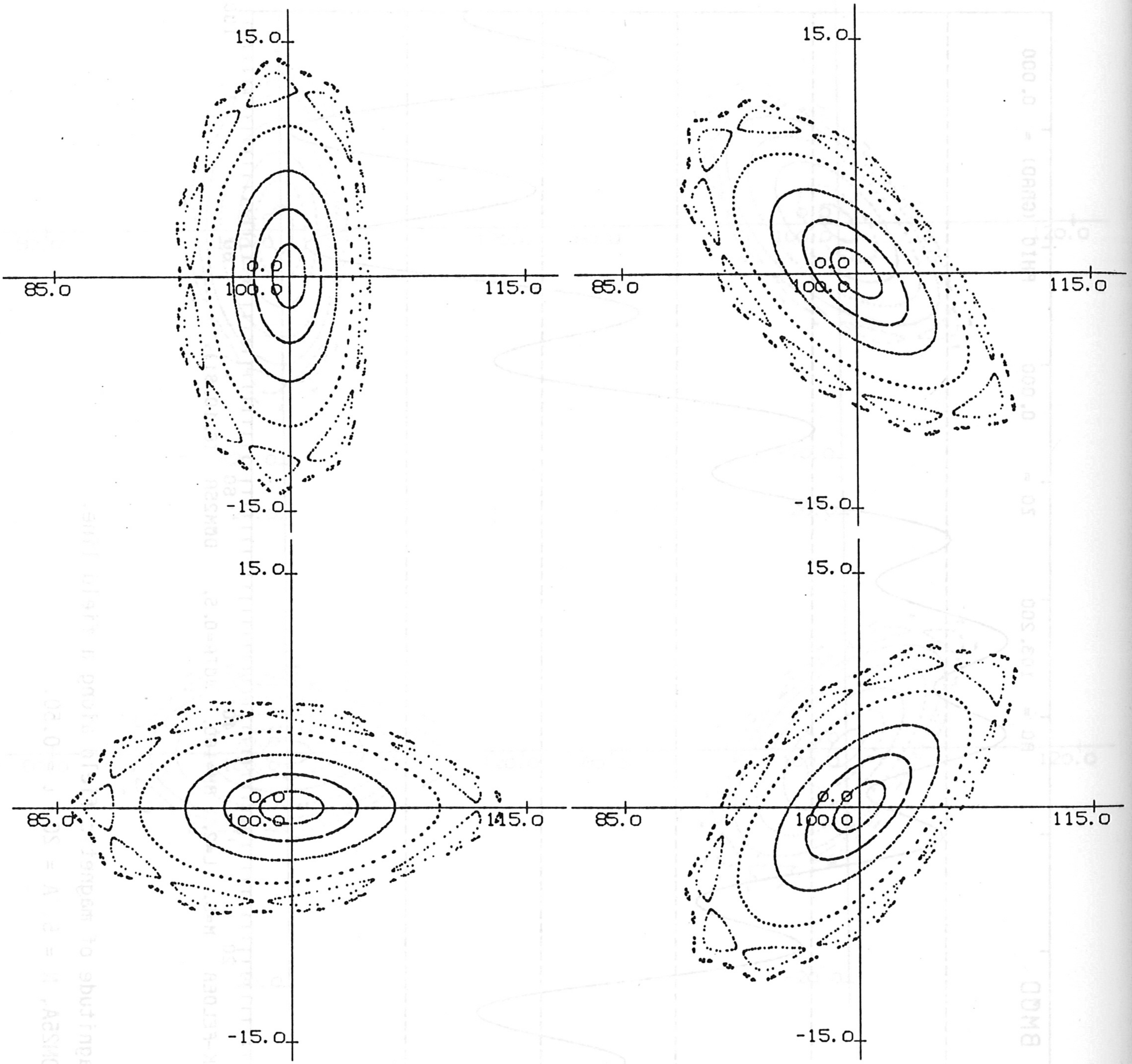

Fig.41: Cross sections of magnetic surfaces.
DOM25B, N = 5 (Table II).

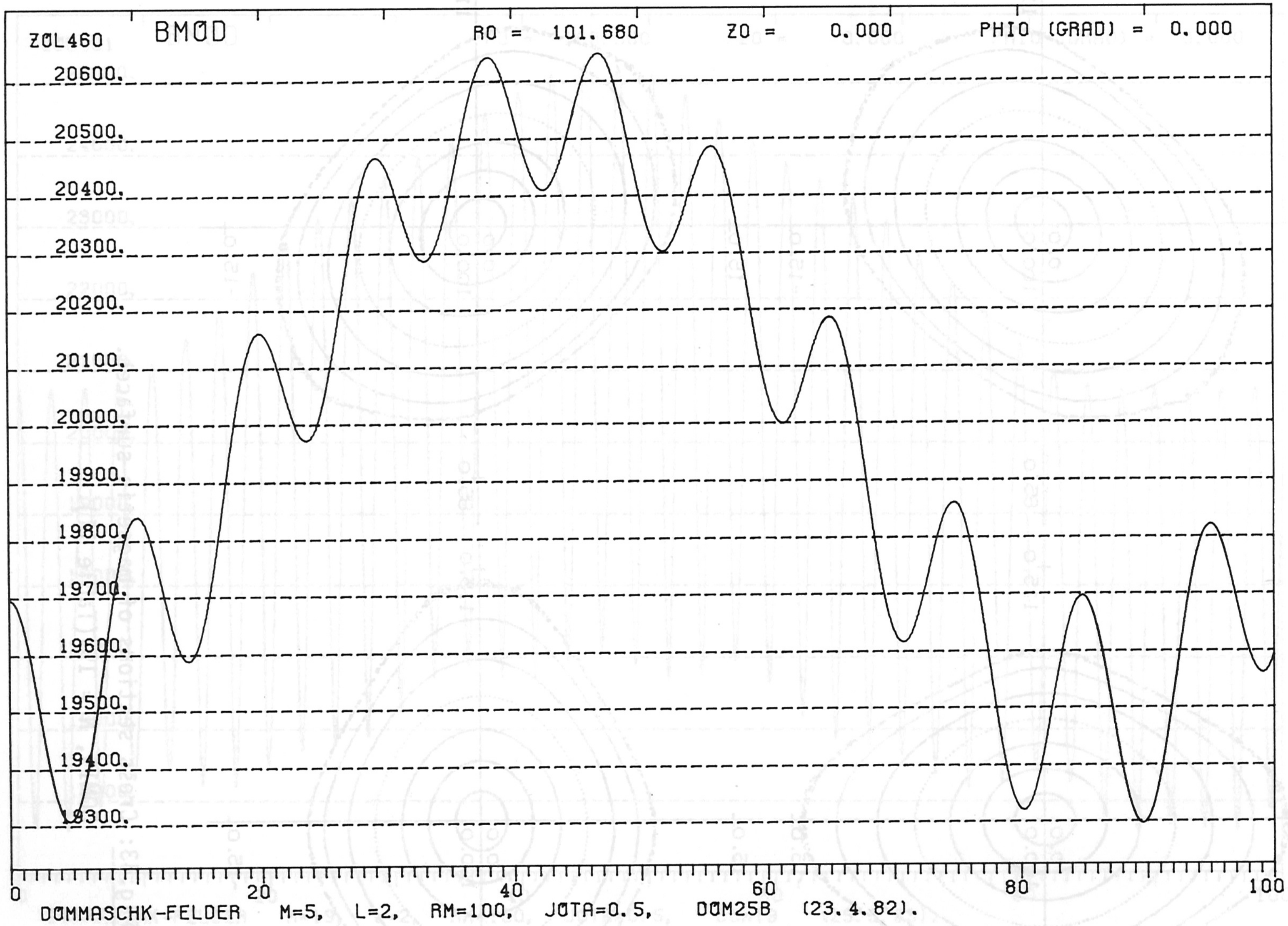

Fig.42: Magnitude of magnetic field along a field line.
DOM25B, N = 5, A = 40, ι = 0.50.

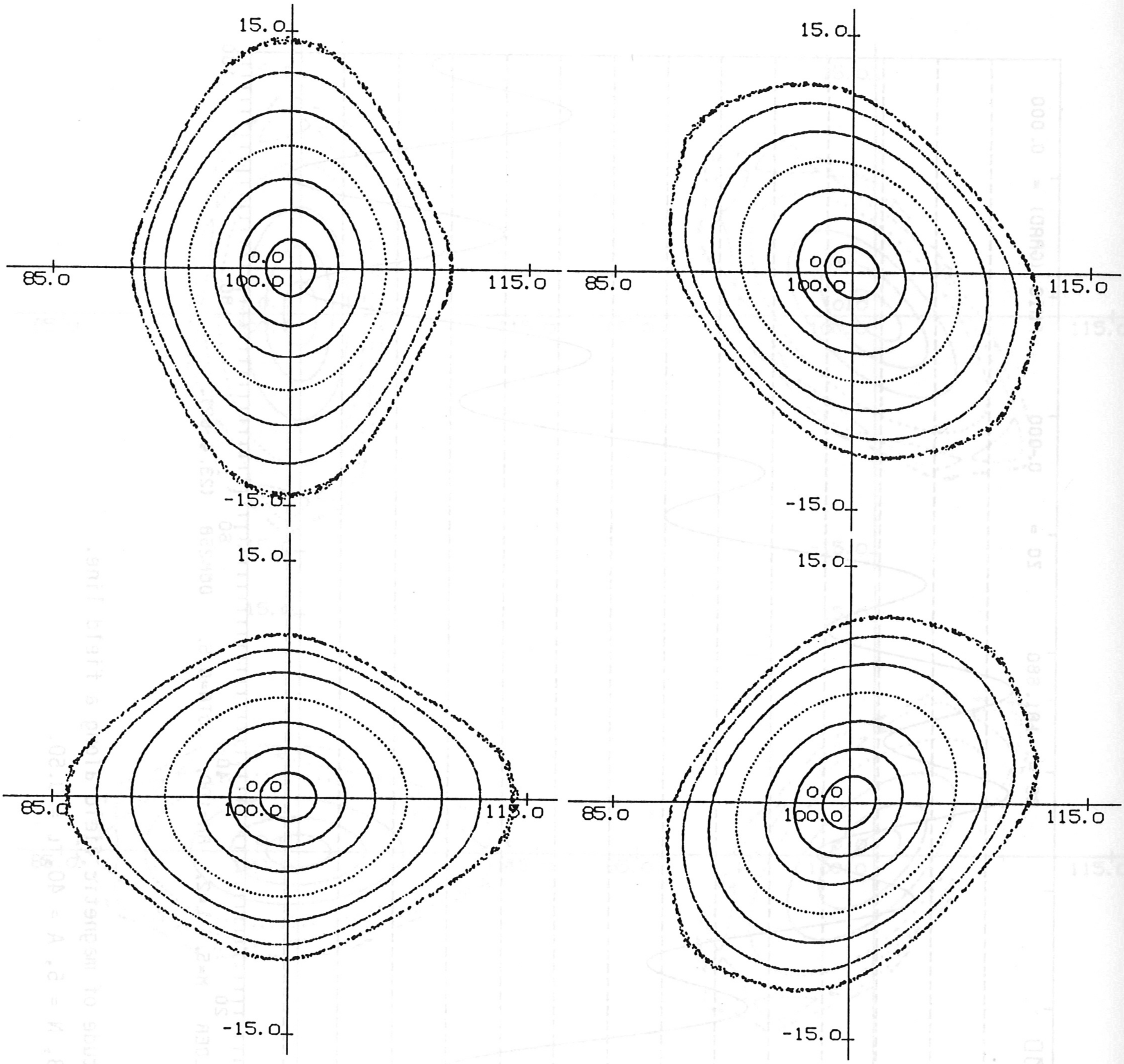

Fig.43: Cross sections of magnetic surfaces.
DOM19, N = 19 (Table II).

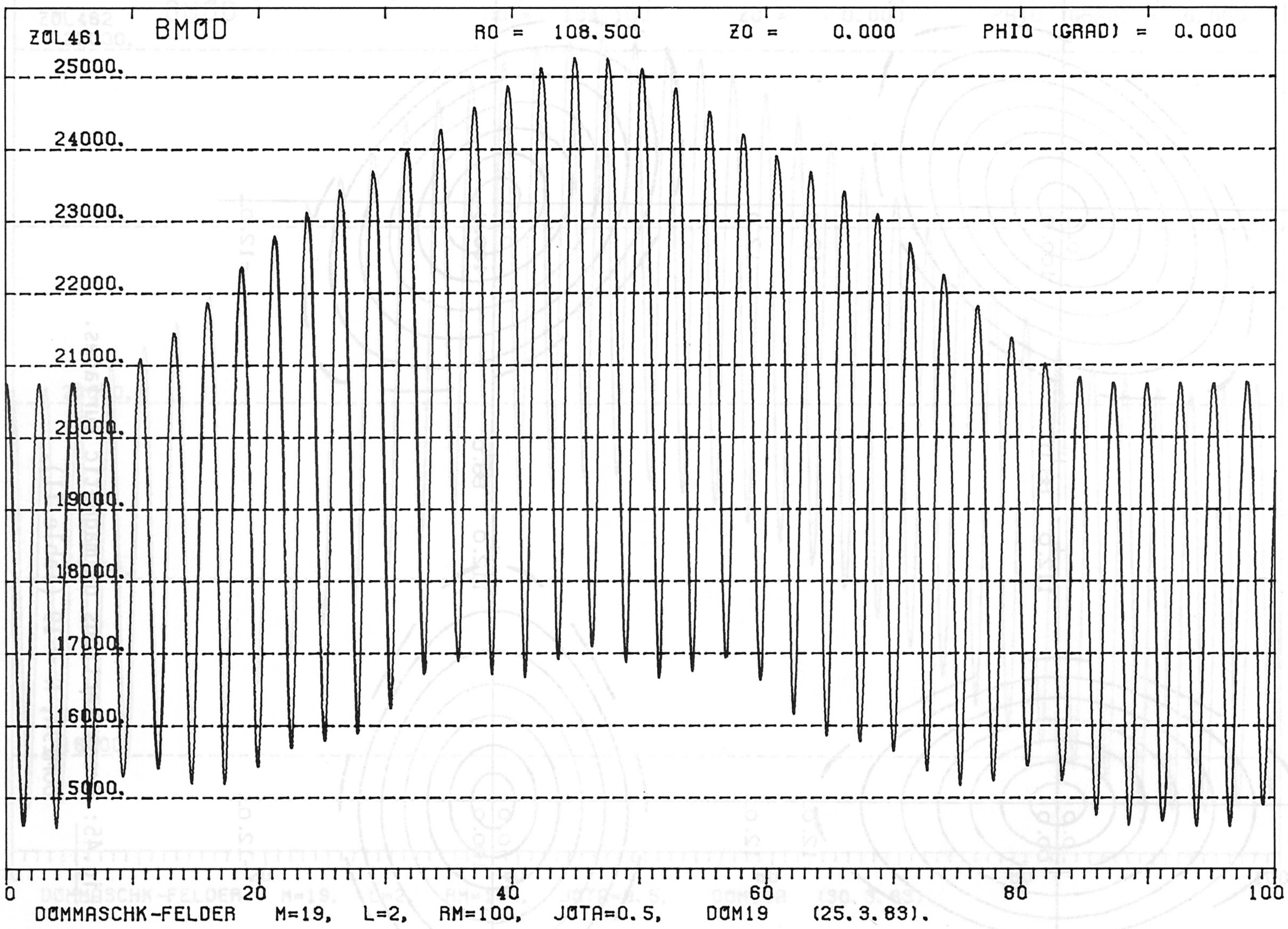

Fig.44: Magnitude of magnetic field along a field line.
DOM19, N = 19, A = 10, ι = 0.52.

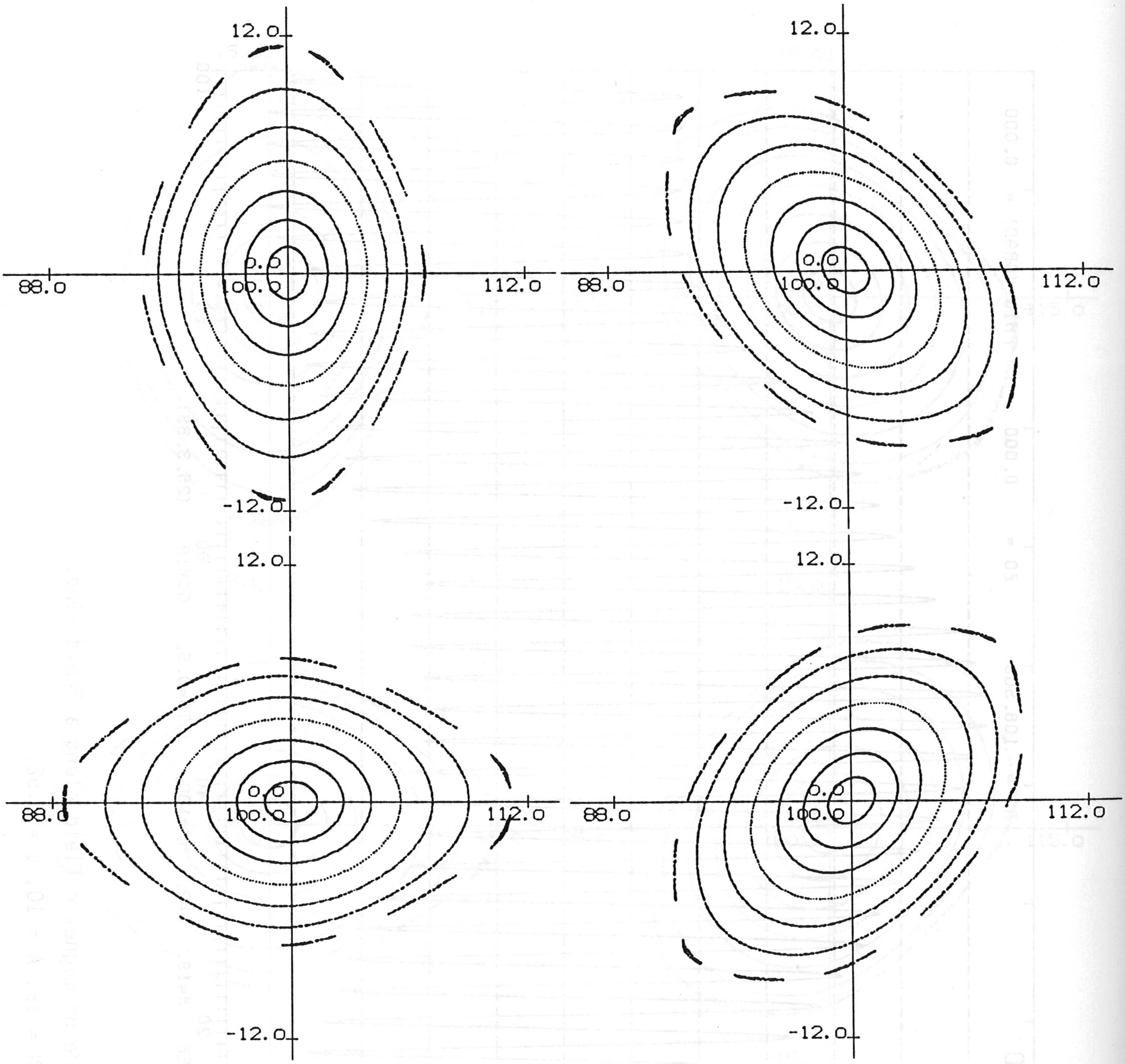

Fig.45: Cross sections of magnetic surfaces.
DOM19A, N = 19 (Table II).

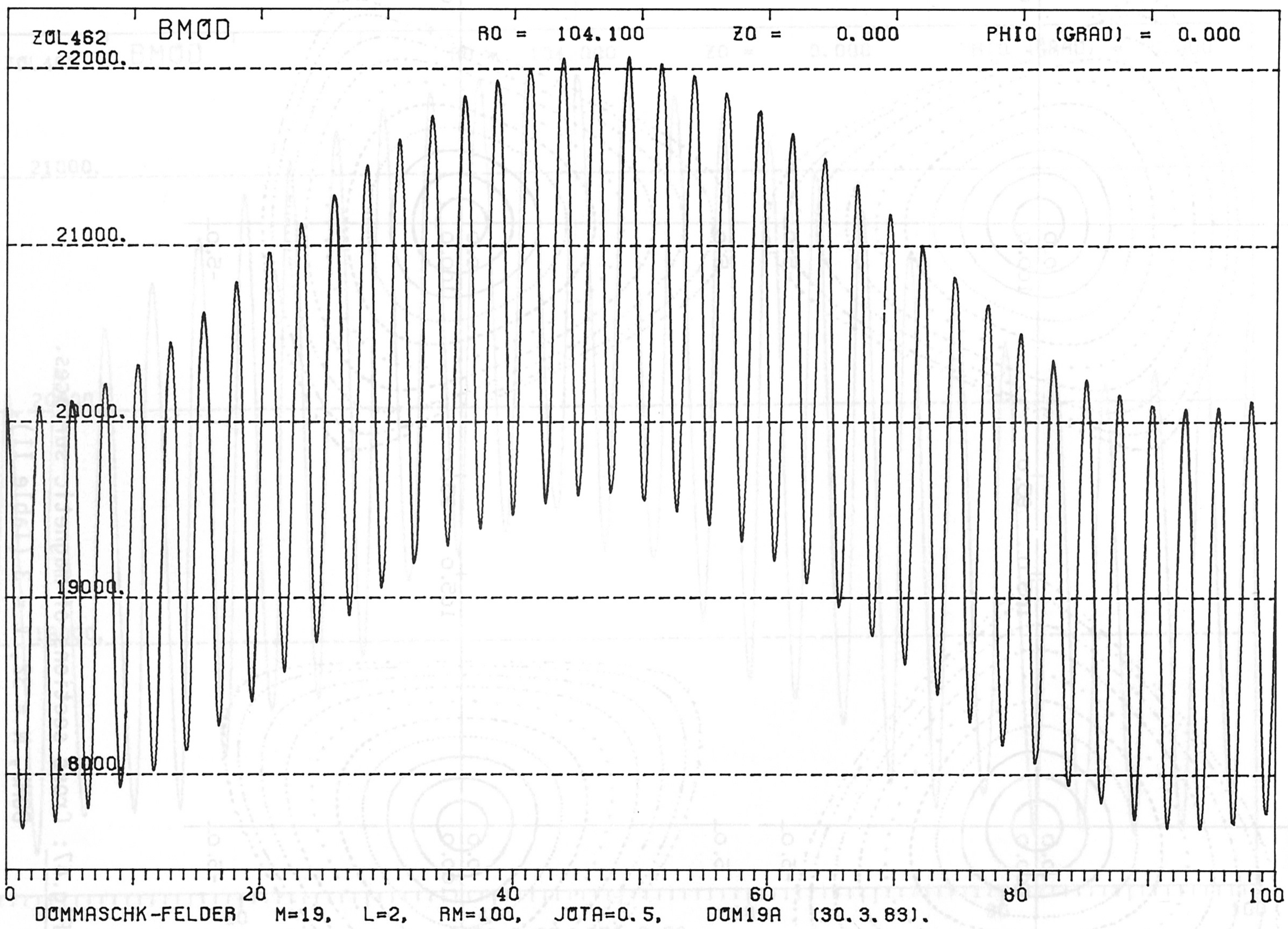

Fig.46: Magnitude of magnetic field along a field line.
DOM19A, N = 19, A = 20, ι = 0.50.

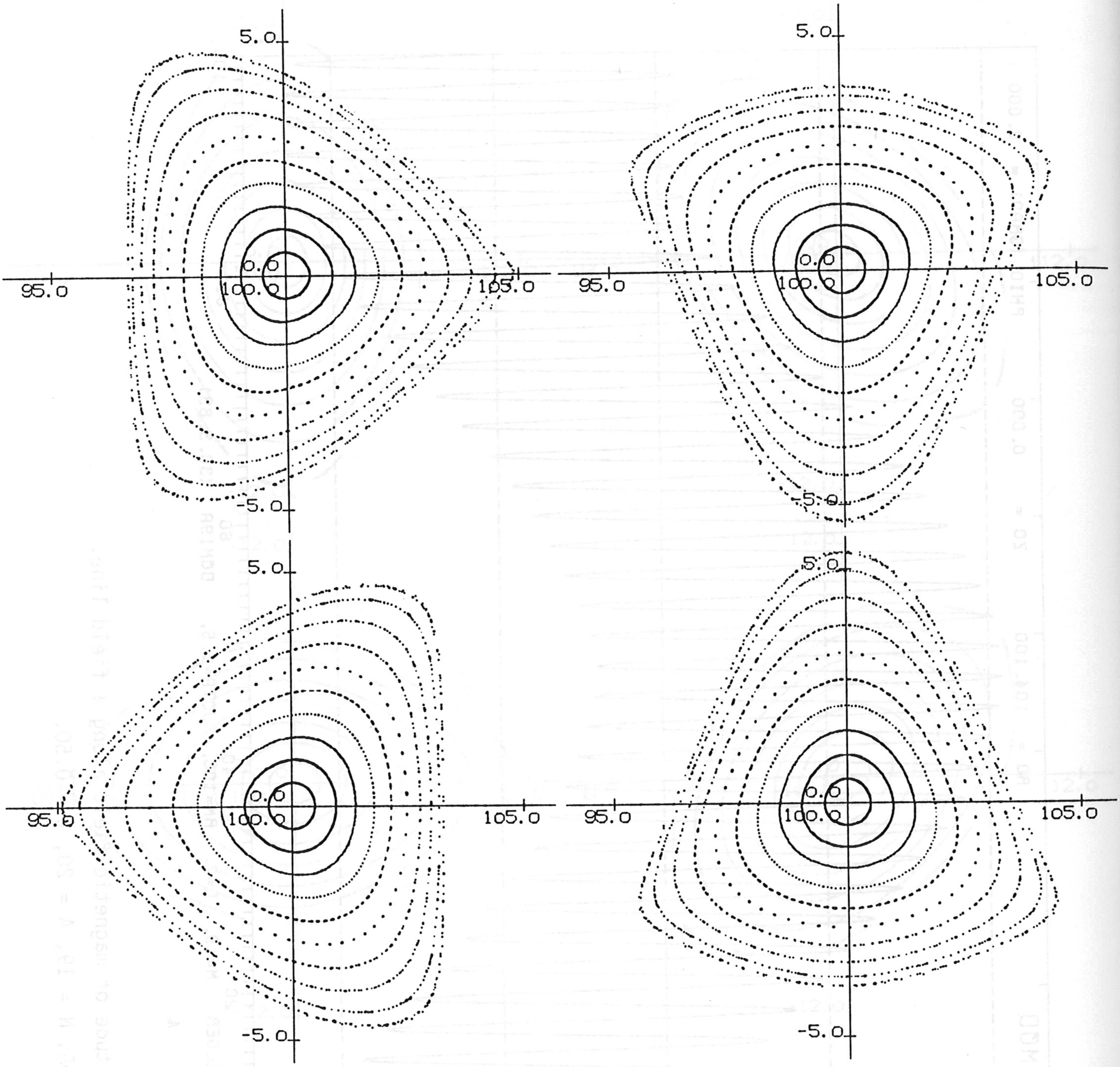

Fig.47: Cross sections of magnetic surfaces.
DOM3, N = 32, ℓ = 3 (Table II).

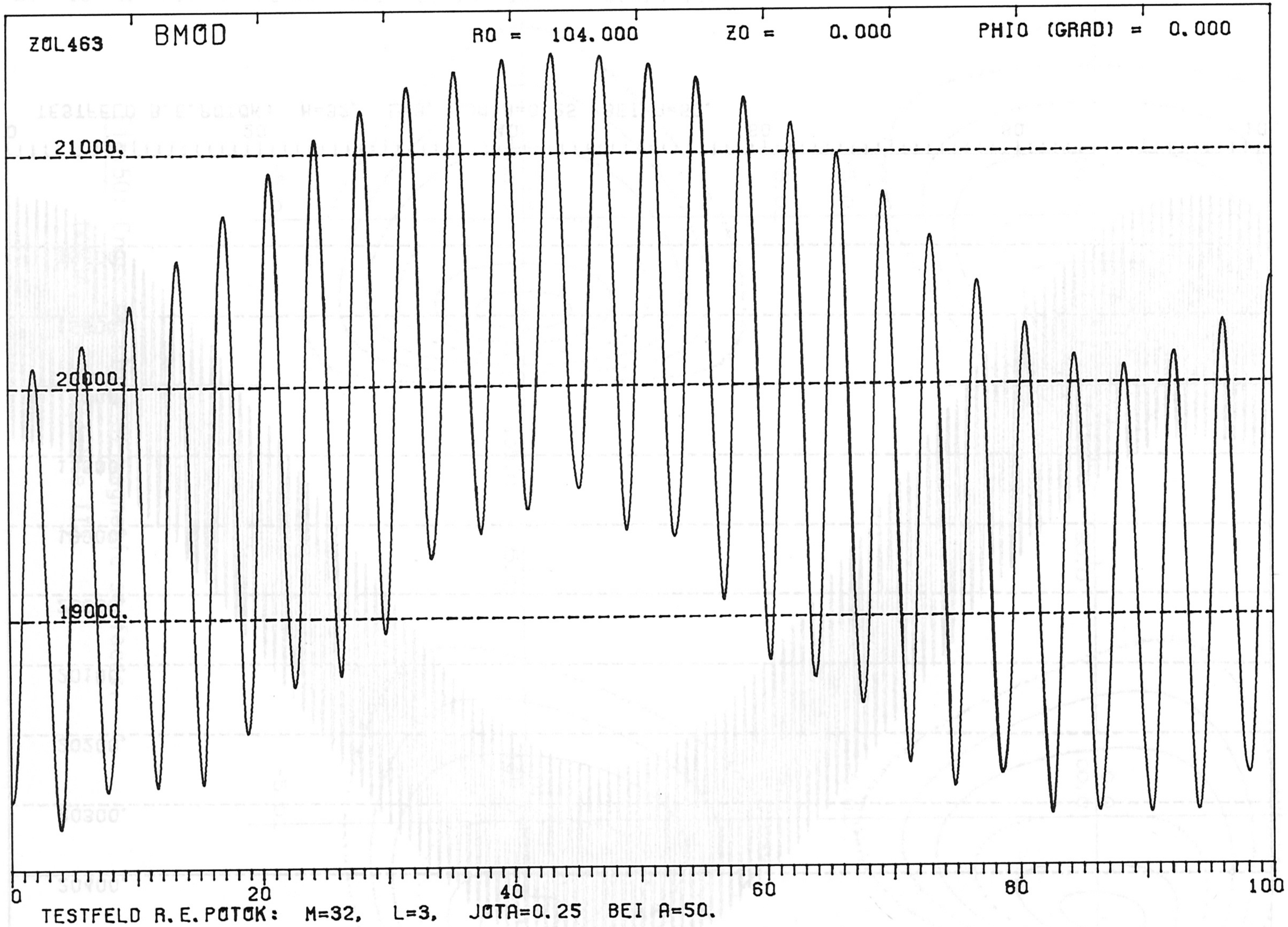

Fig.48: Magnitude of magnetic field along a field line.
DOM3, N = 32, A = 27, ι = 1.21.

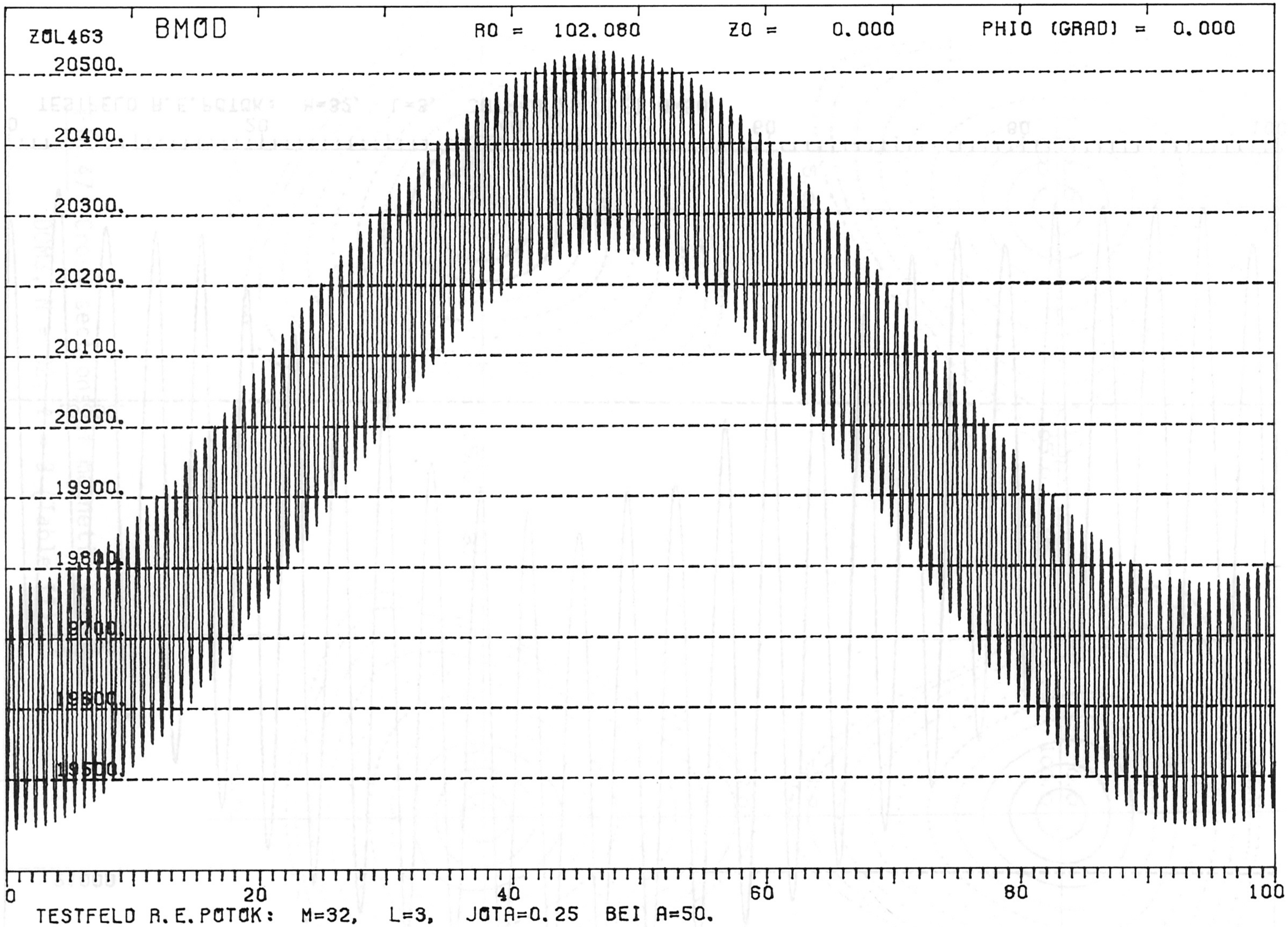

Fig.49: Magnitude of magnetic field along a field line.

DOM3, N = 32, A = 50, ι = 0.25.

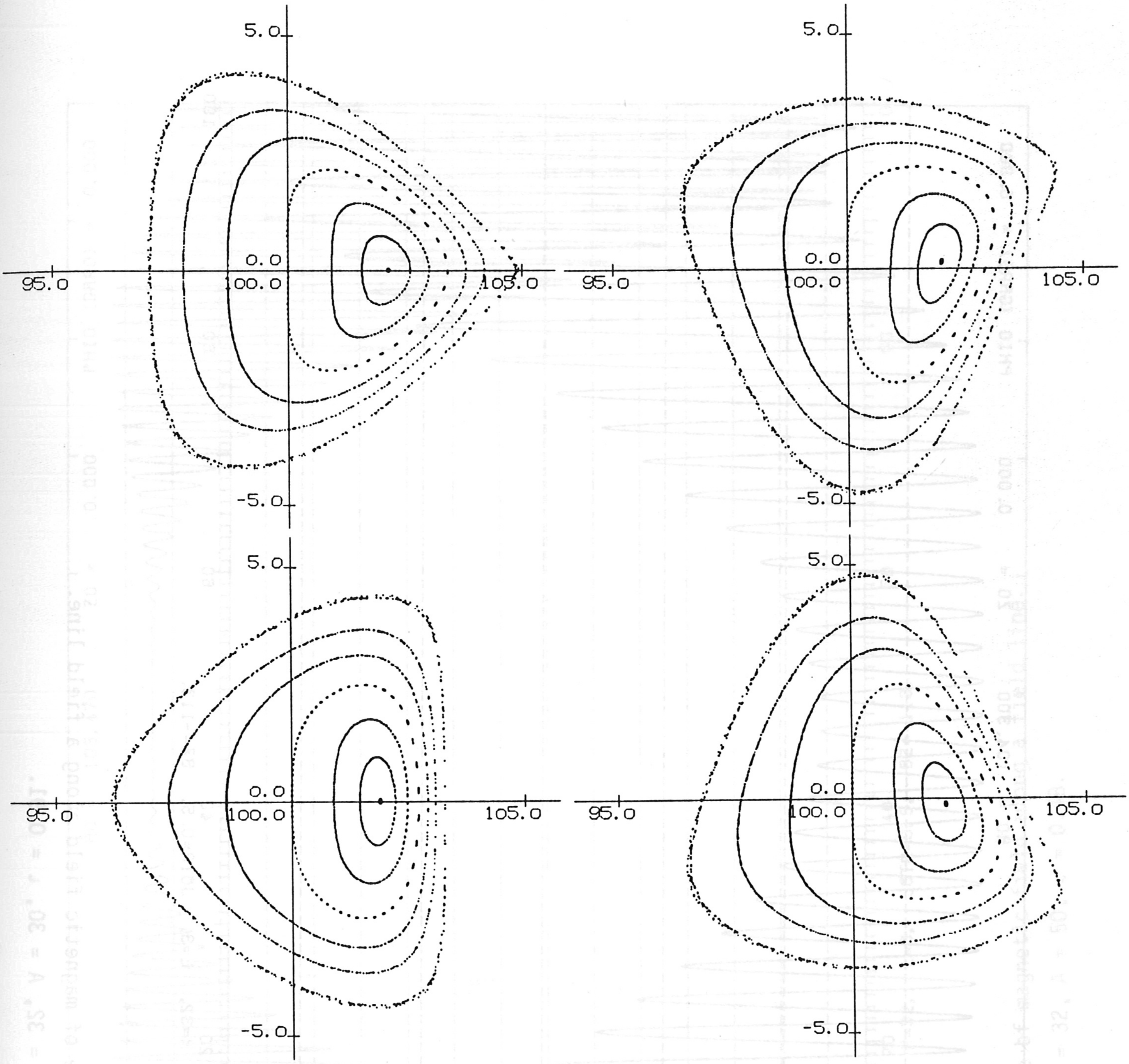

Fig.50: Cross sections of magnetic surfaces.
DOM3A, N = 32 (Table II).

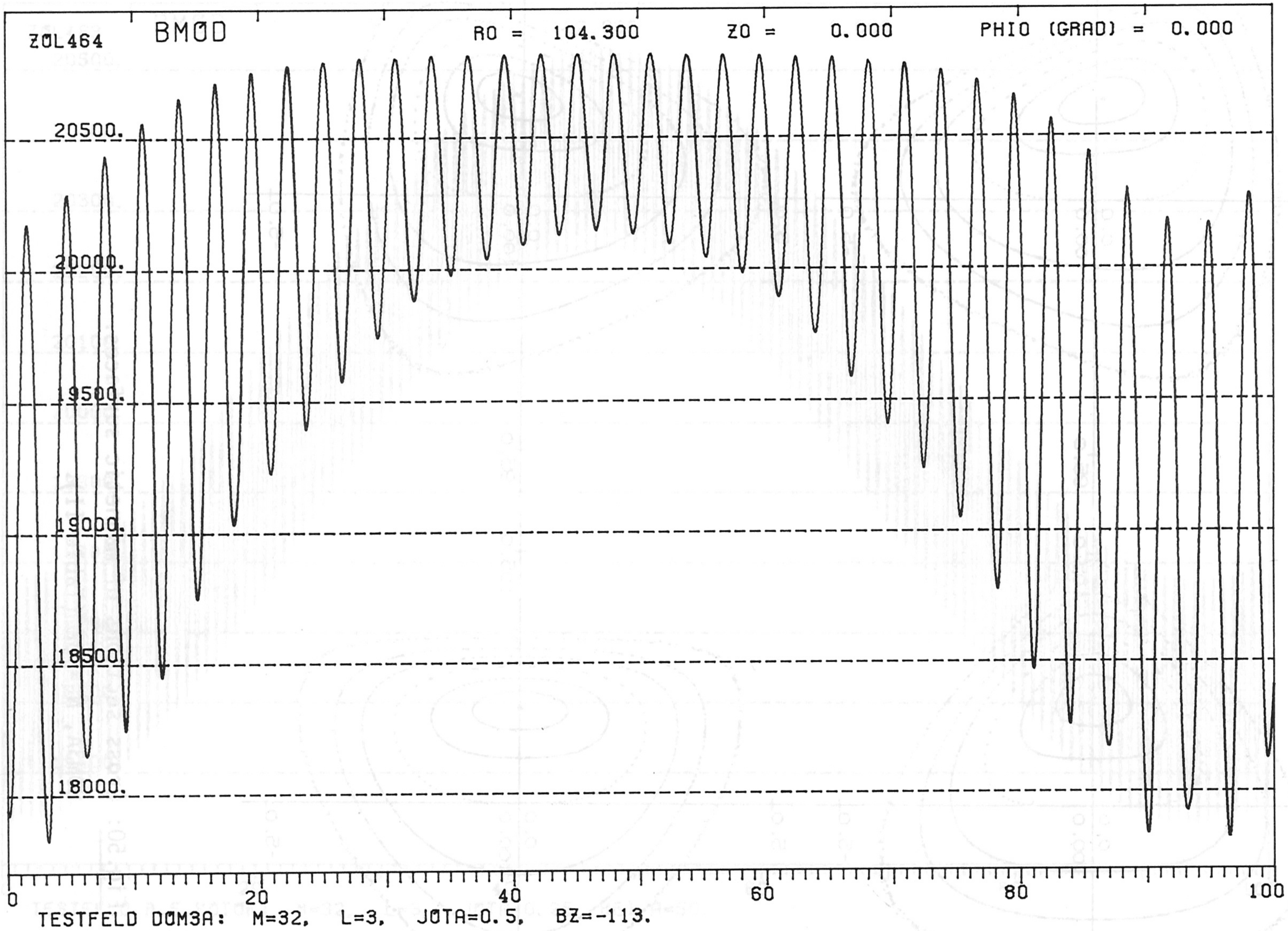

Fig.51: Magnitude of magnetic field along a field line.
DOM3A, N = 32, A = 30, ι = 0.91.

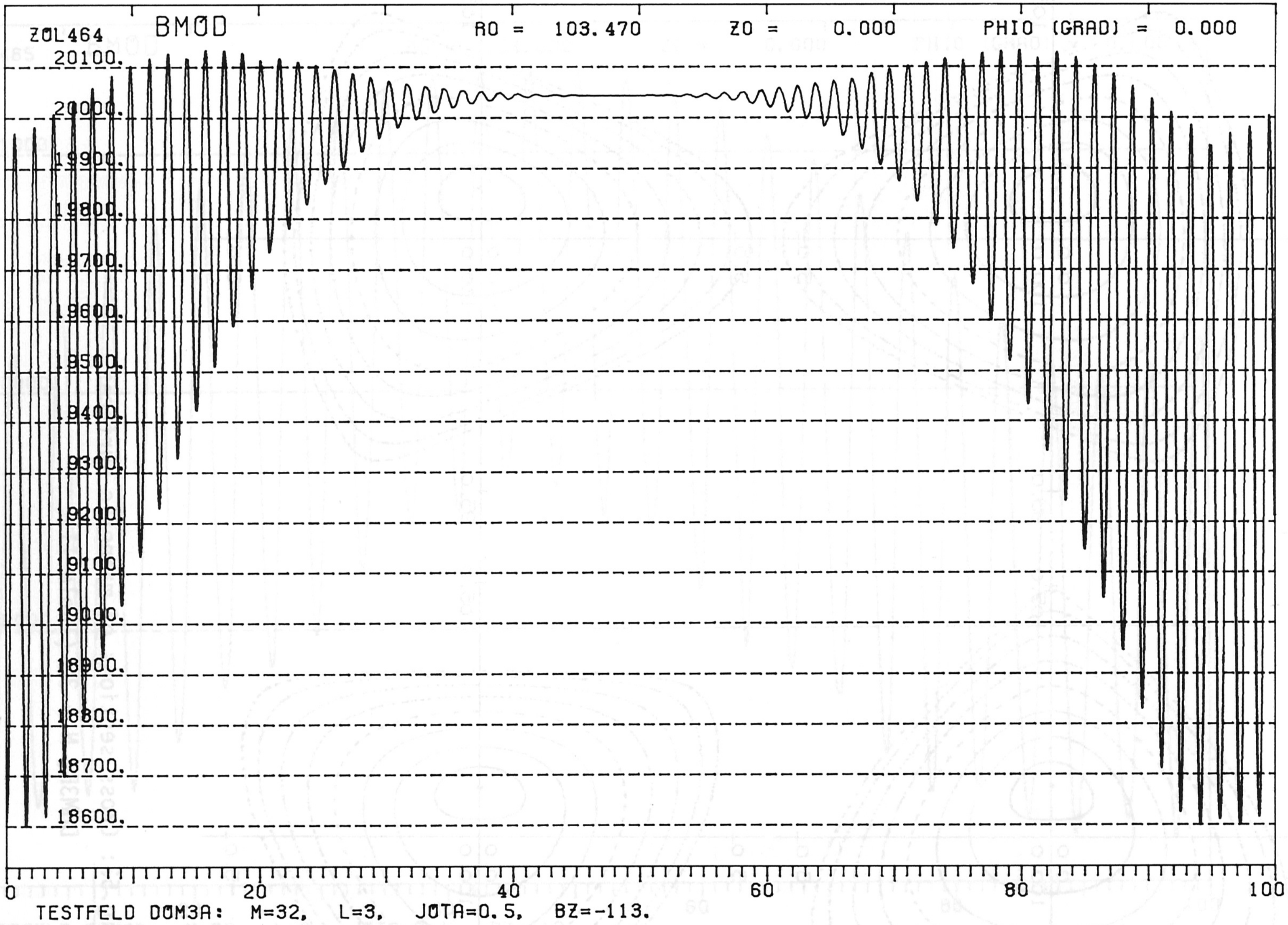

Fig.52: Magnitude of magnetic field along a field line.
DOM3A, N = 32, A = 50, ι = 0.48.

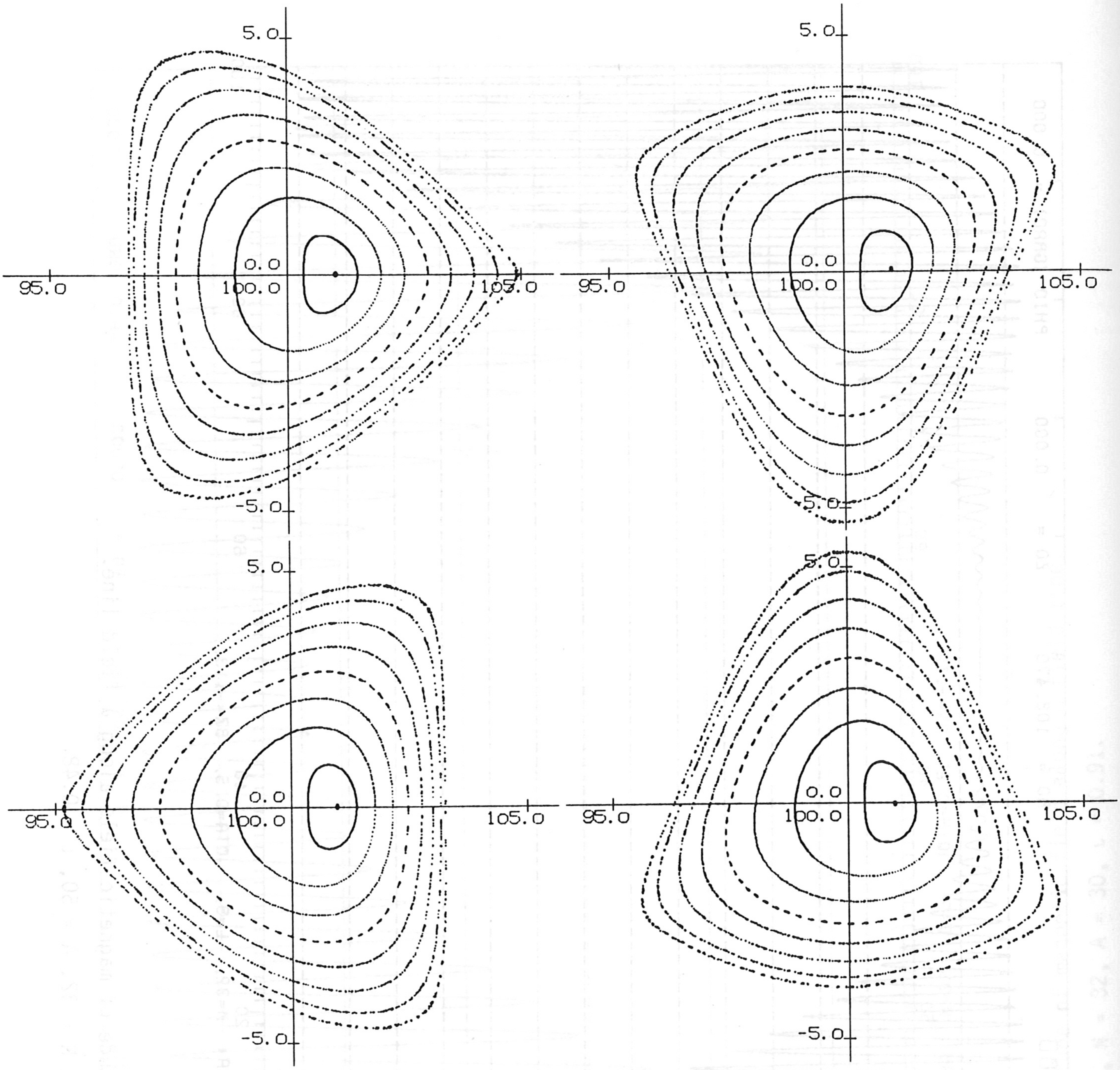

Fig.53: Cross sections of magnetic surfaces.
DOM3B, N = 32 (Table II).

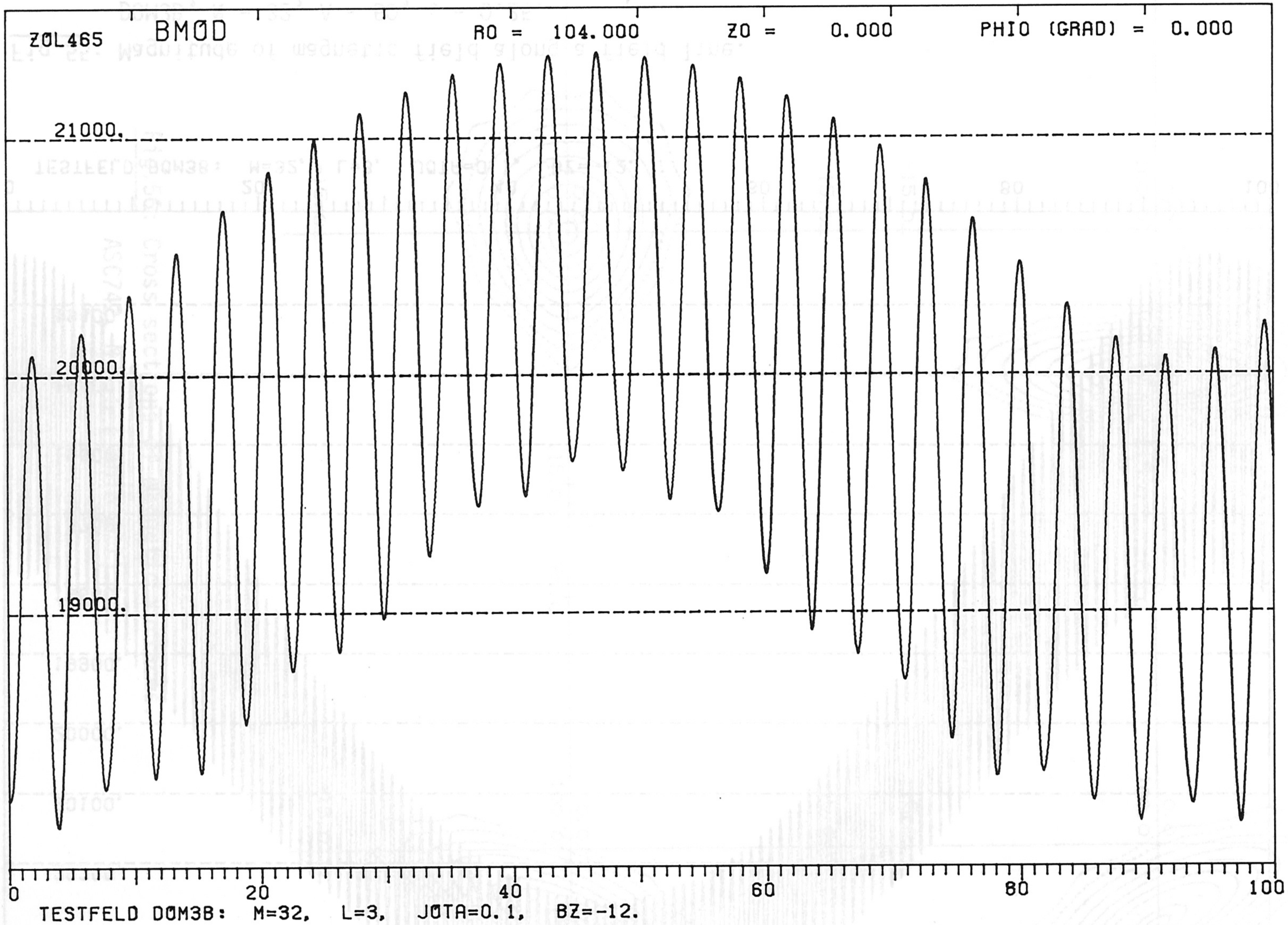

Fig.54: Magnitude of magnetic field along a field line.
DOM3B, N = 32, A = 27, ι = 1.15.

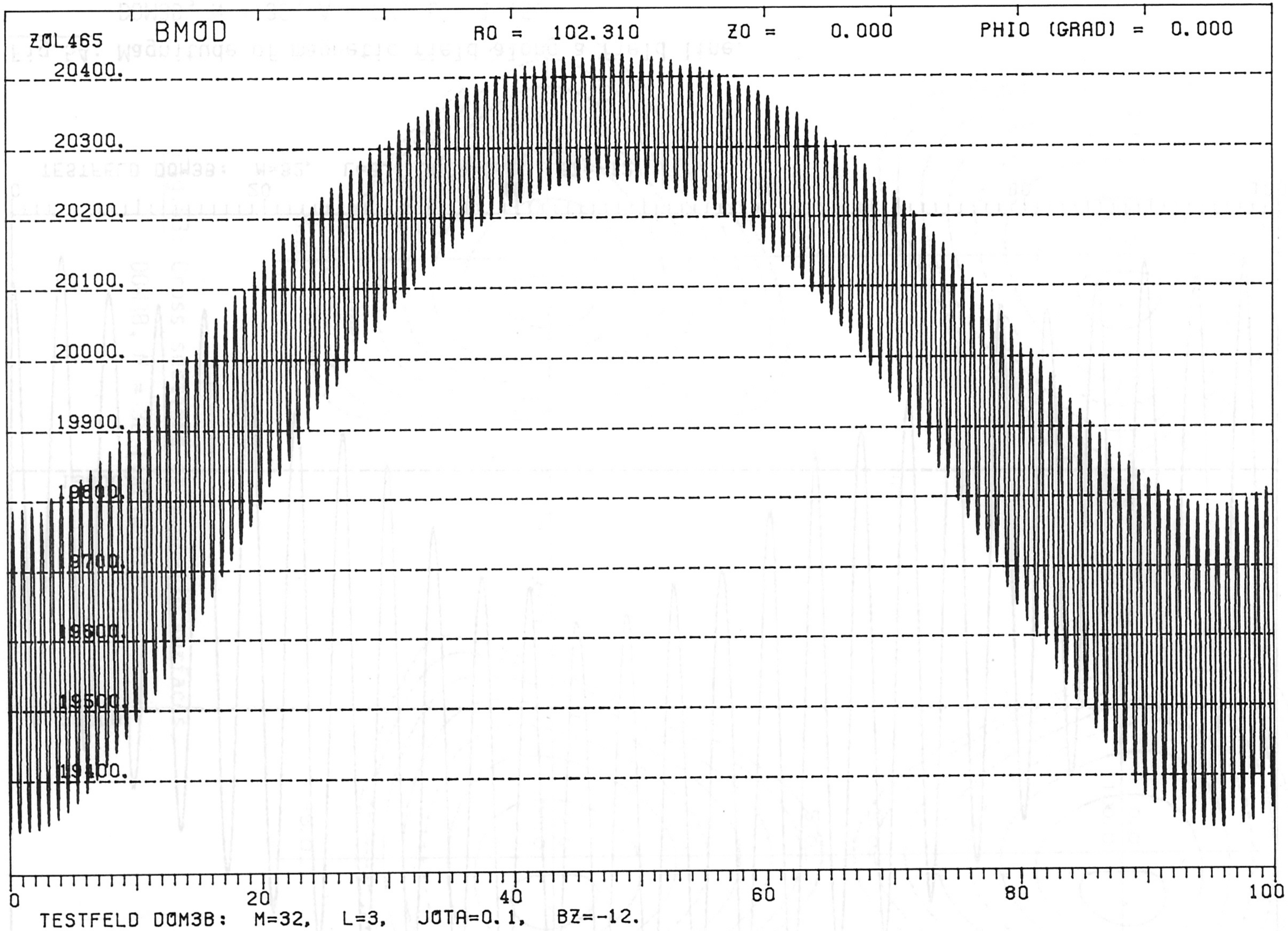

Fig.55: Magnitude of magnetic field along a field line.
DOM3B, N = 32, A = 50, ι = 0.25.

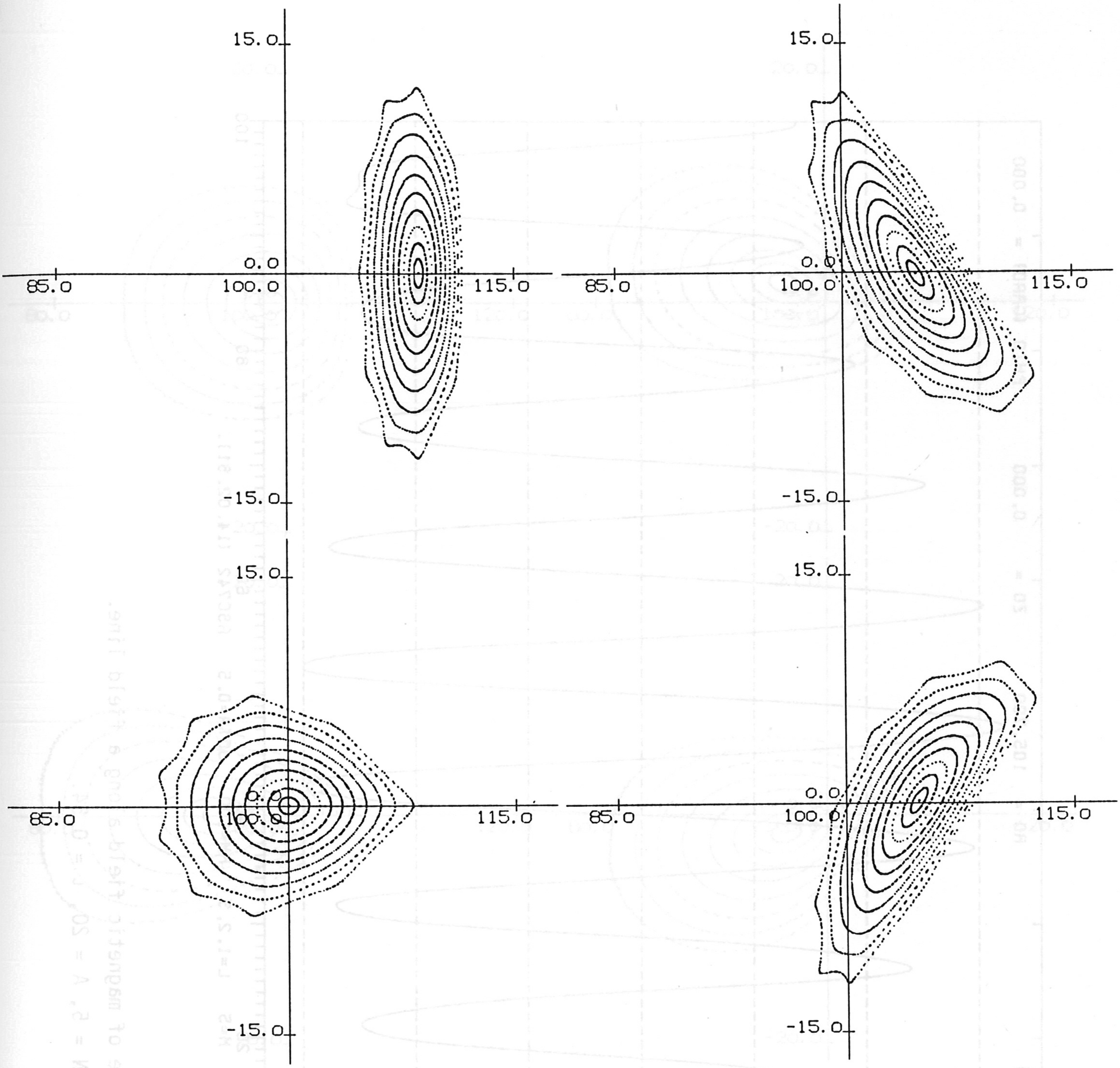

Fig.56: Cross sections of magnetic surfaces.
ASC742, N = 5 (Table III).

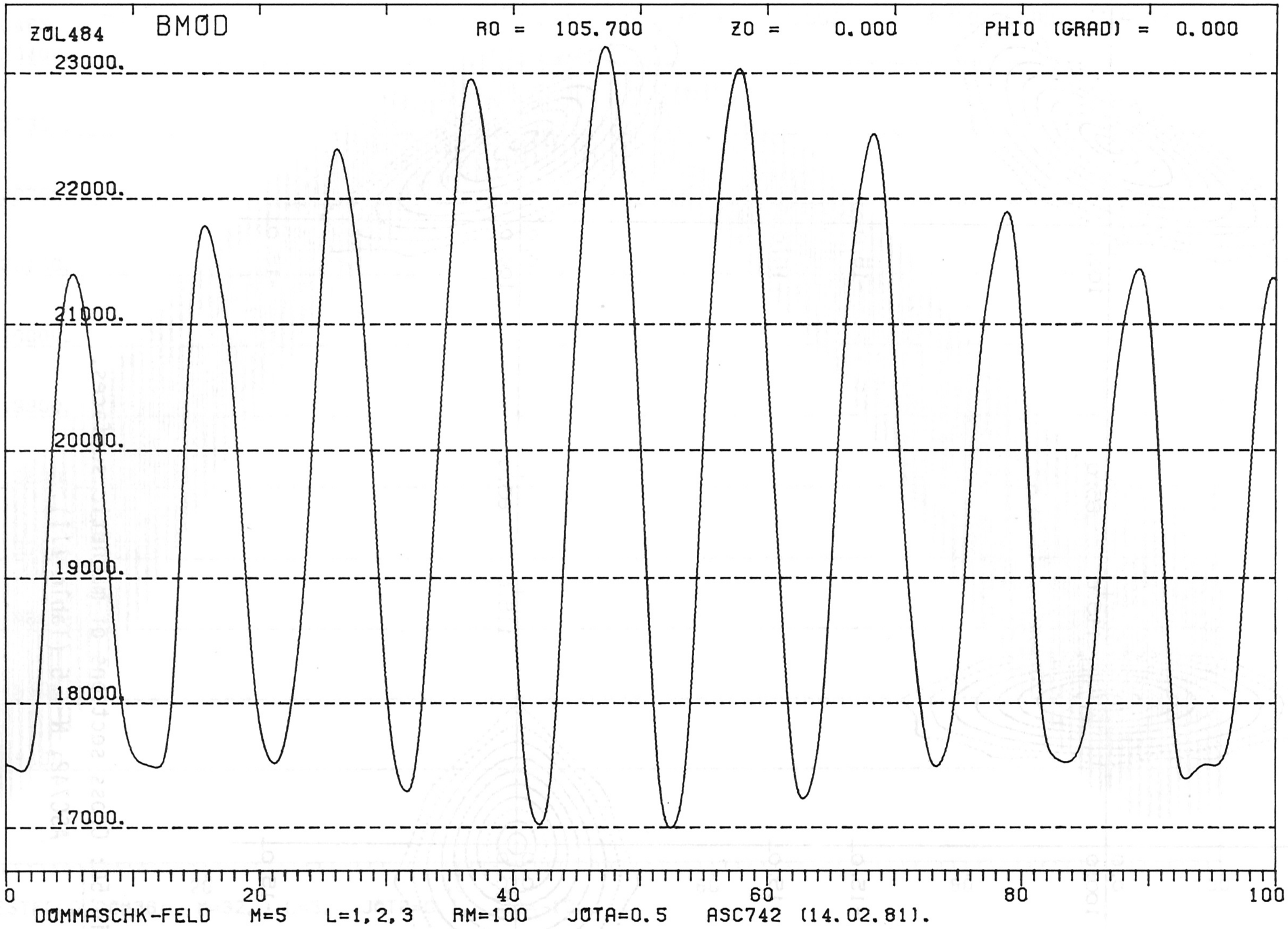

Fig.57: Magnitude of magnetic field along a field line.
ASC742, N = 5, A = 20, ι = 0.54.

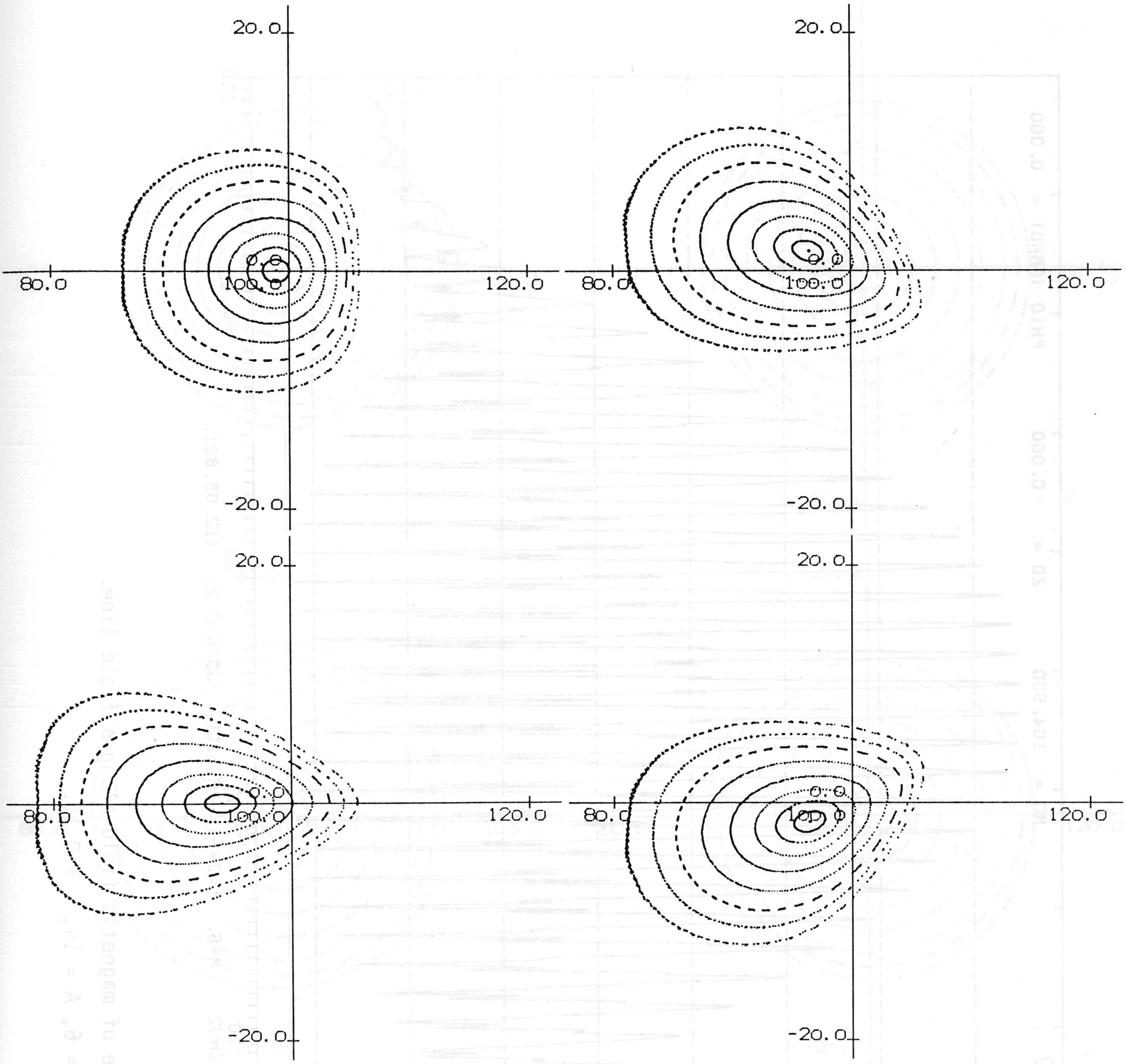

Fig.58: Cross sections of magnetic surfaces.
CHU2, N = 6 (Table III).

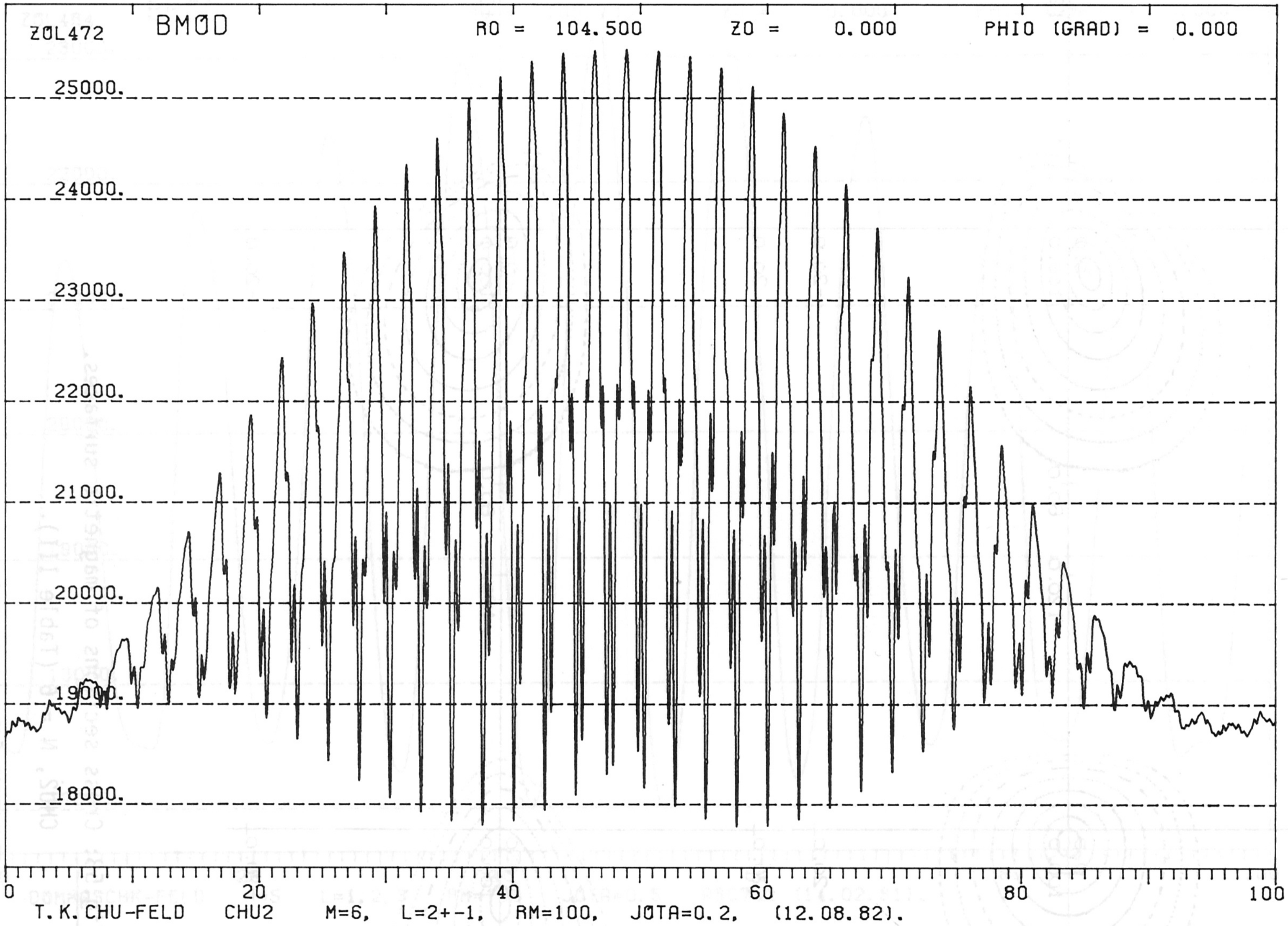

Fig.59: Magnitude of magnetic field along a field line.
CHU2, N = 6, A = 14, ι = 0.15.

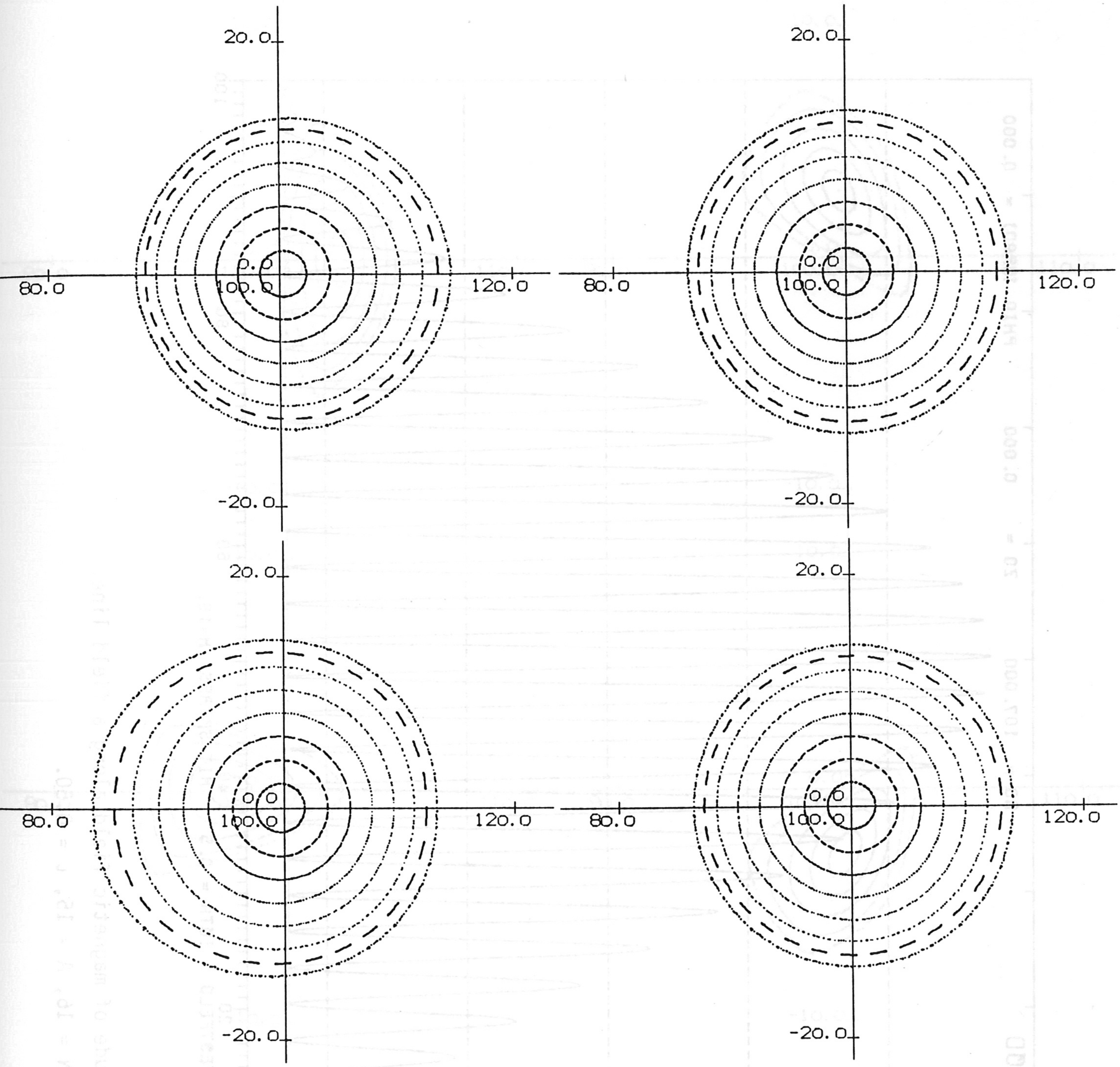

Fig.60: Cross sections of magnetic surfaces.
MYN2, N = 16 (Table III).

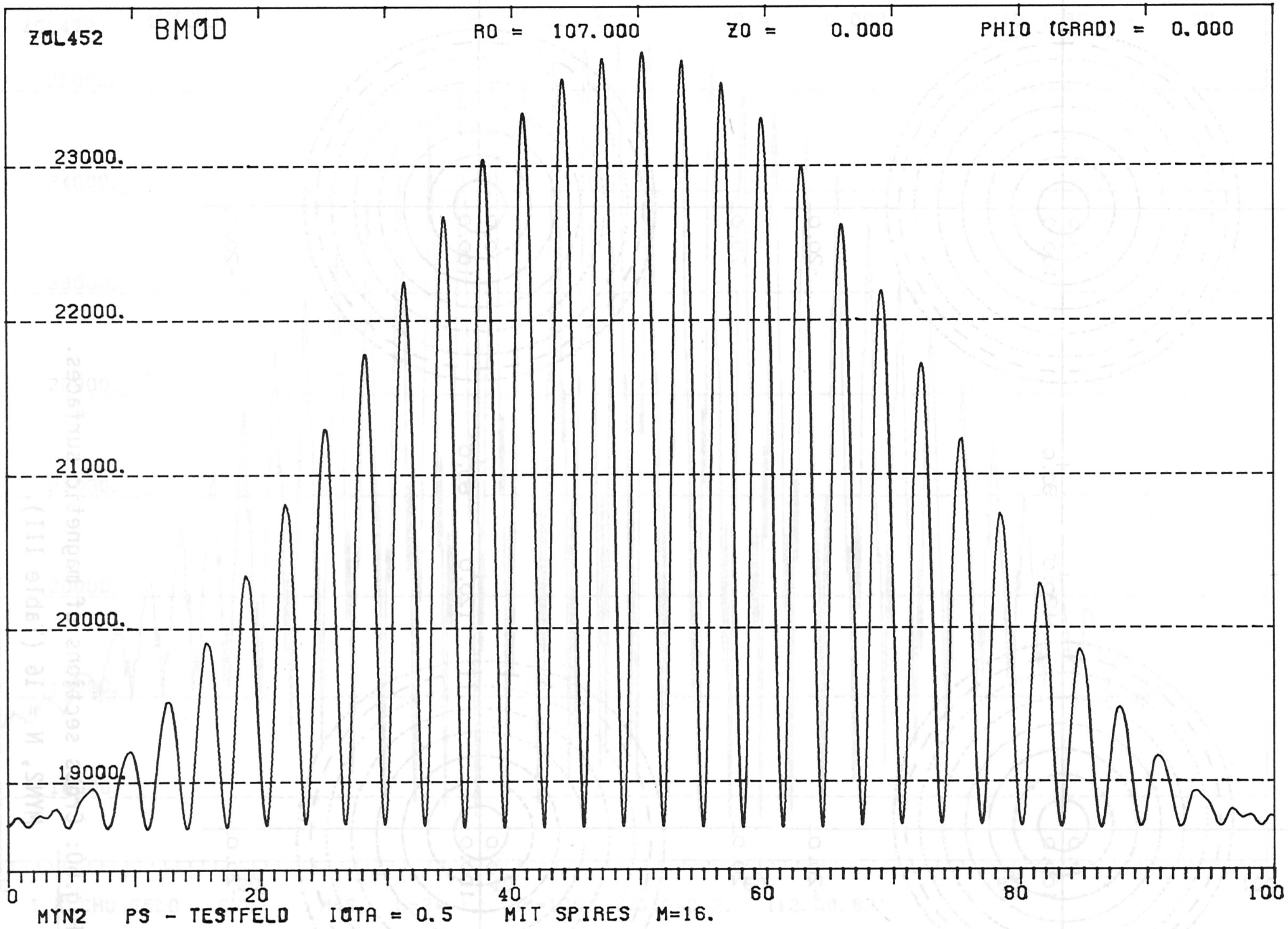

Fig.61: Magnitude of magnetic field along a field line.
MYN2, N = 16, A = 15, ι = 0.50.

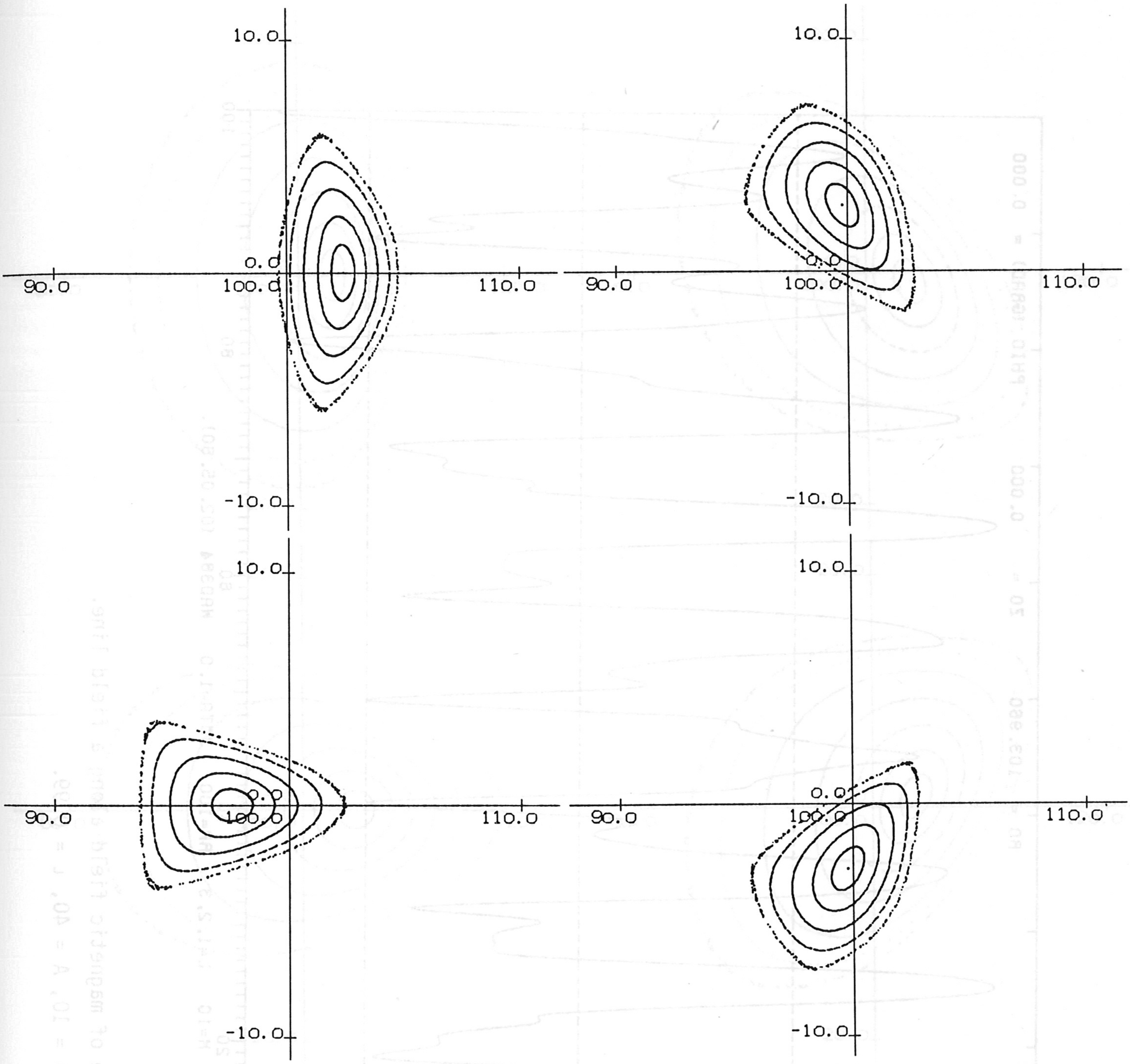

Fig.62: Cross sections of magnetic surfaces. WAD384, N = 10 (Table III).

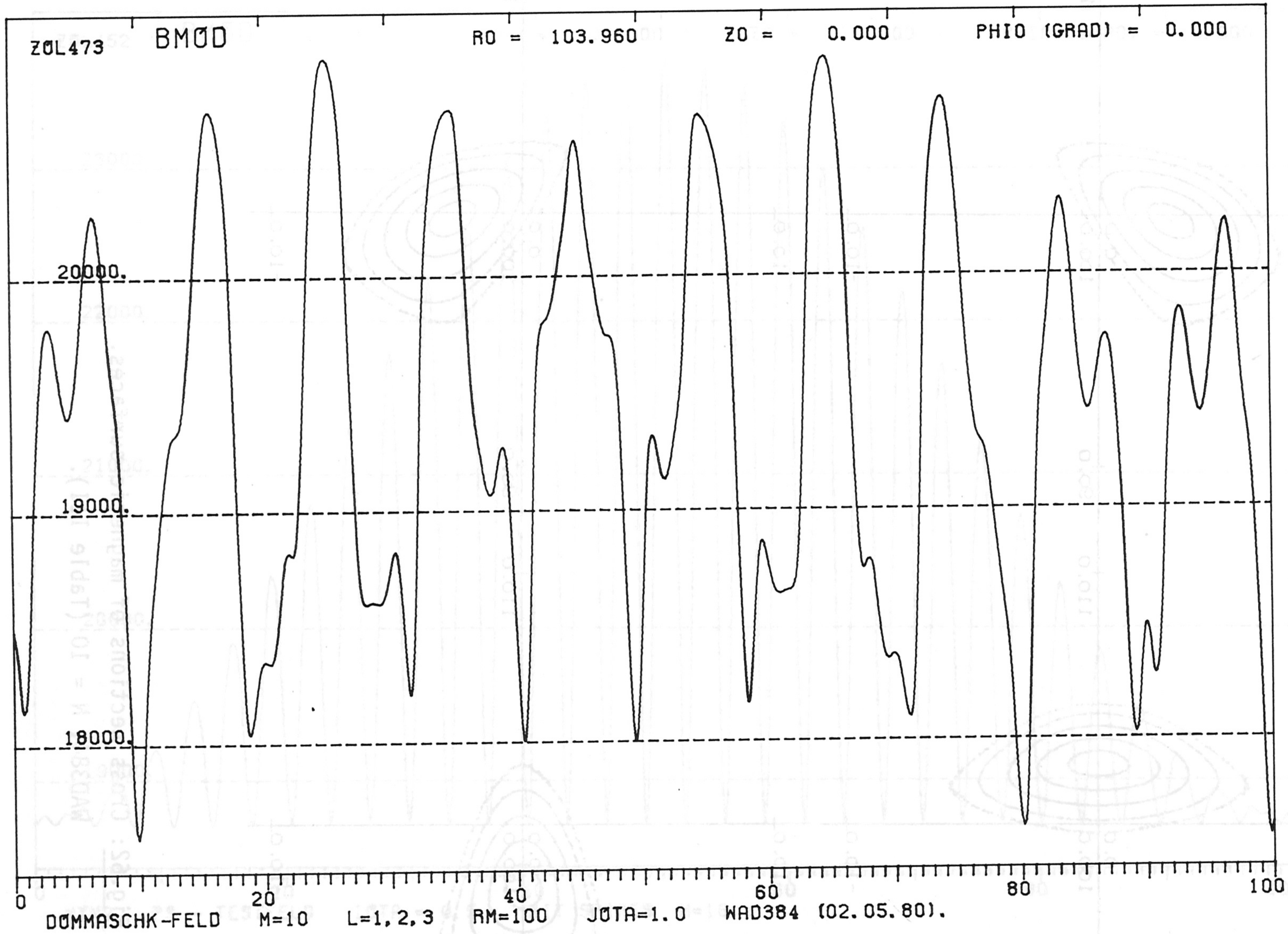

Fig.63: Magnitude of magnetic field along a field line.
WAD384, N = 10, A = 40, ι = 0.99.

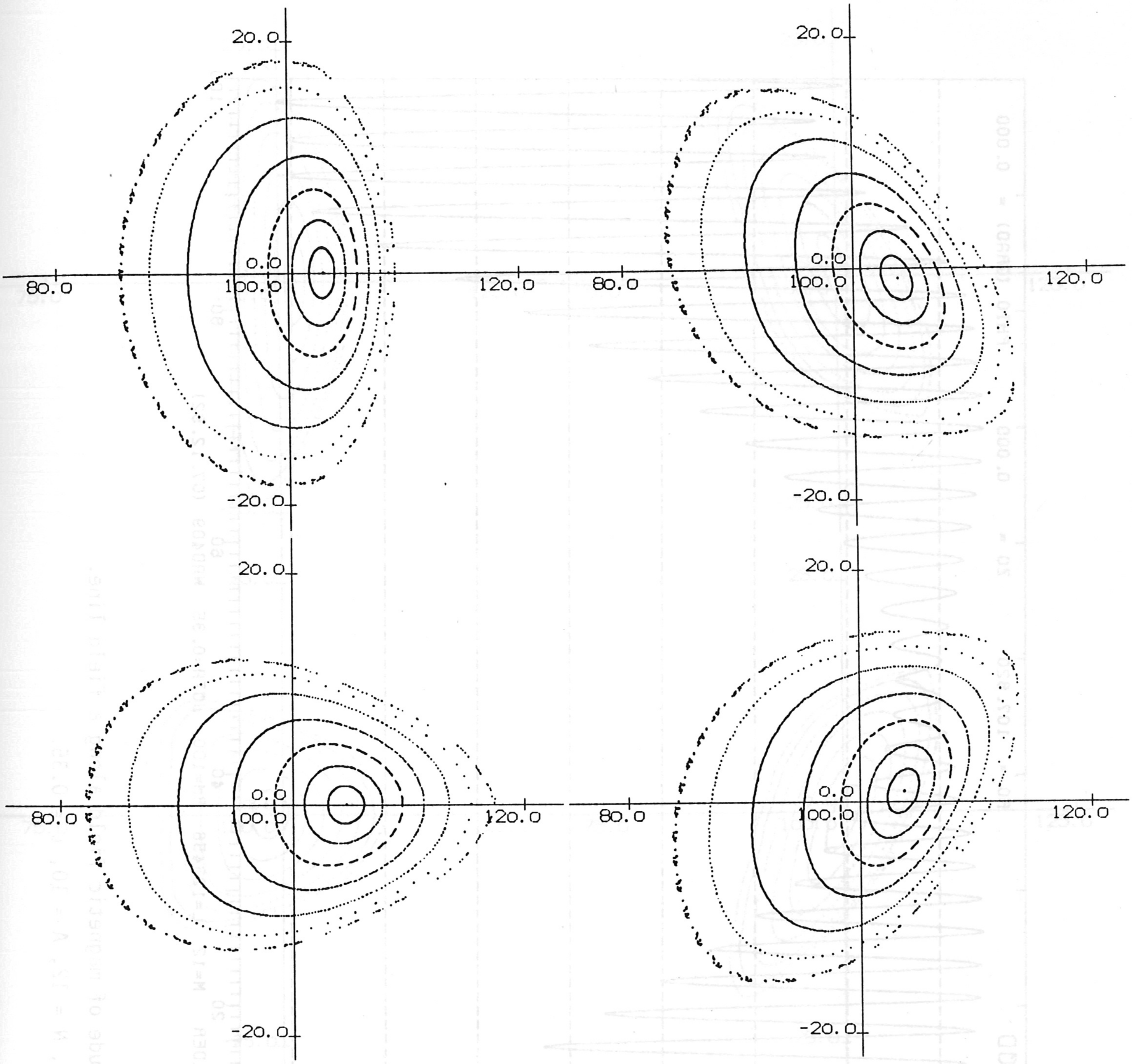

Fig.64: Cross sections of magnetic surfaces.
WAD409, N = 12 (Table III).

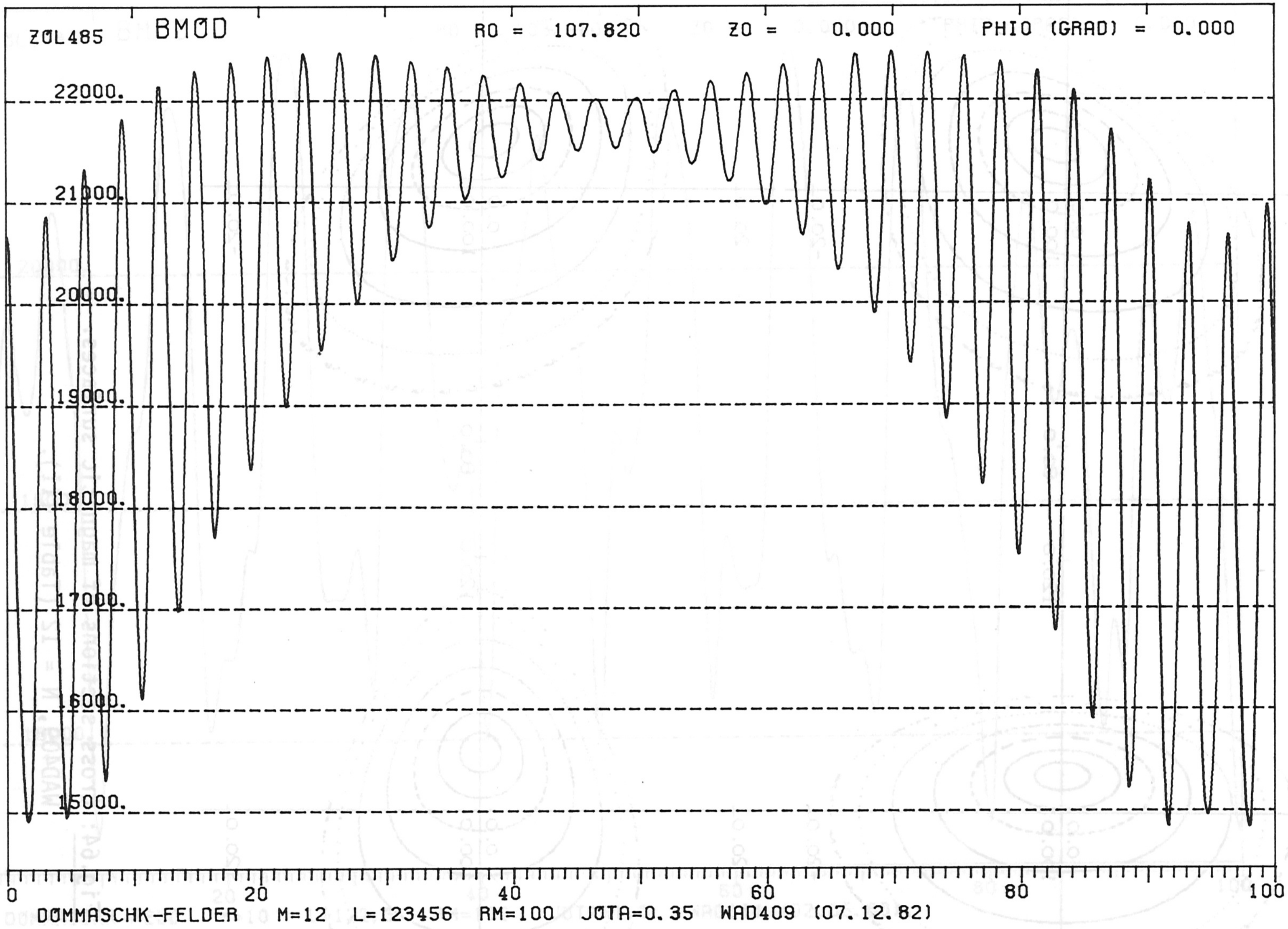

Fig.65: Magnitude of magnetic field along a field line.
WAD409, $N = 12$, $A = 10$, $\iota = 0.35$.

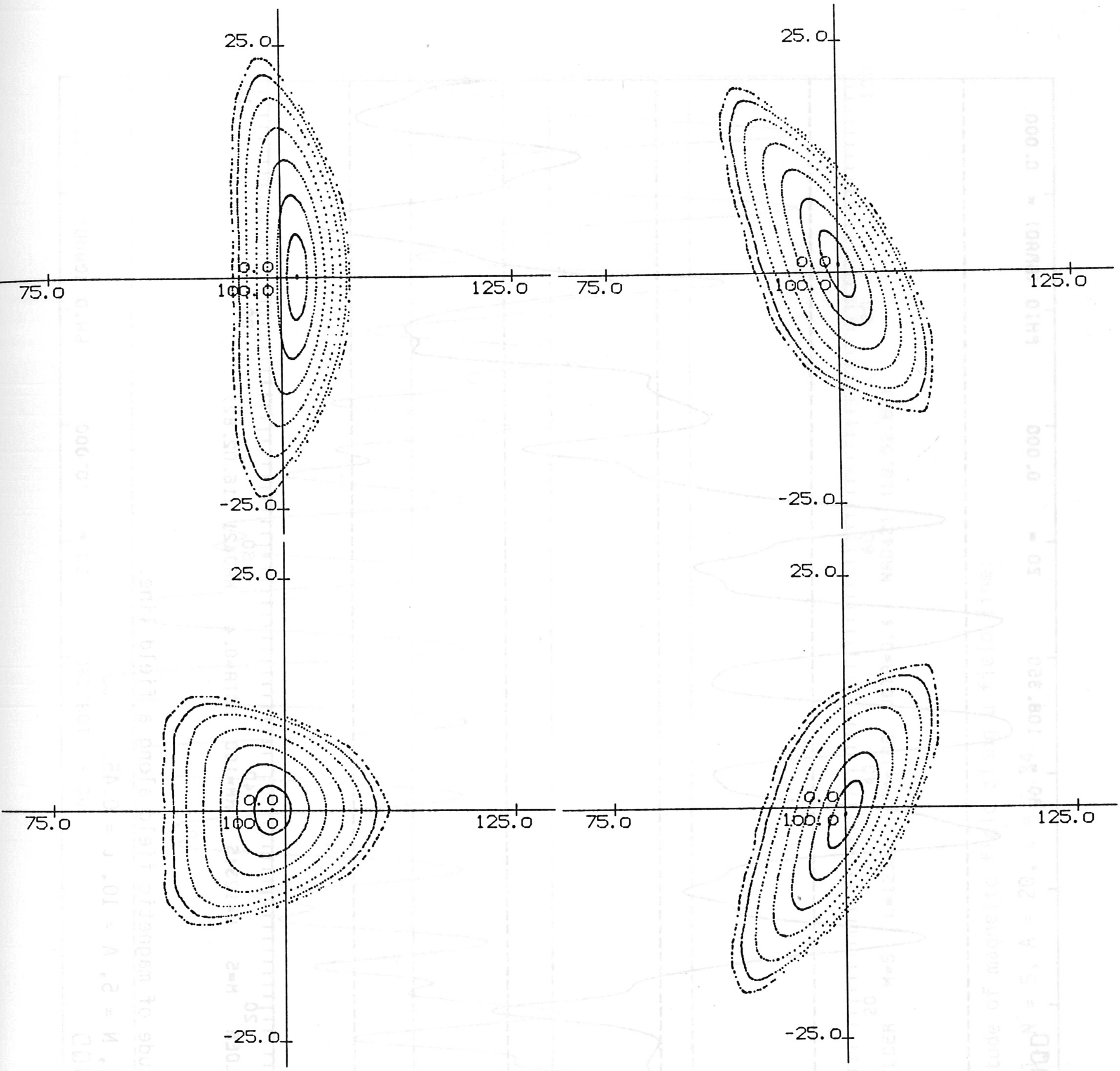

Fig.66: Cross sections of magnetic surfaces.
WAD421, N = 5, (Table III).

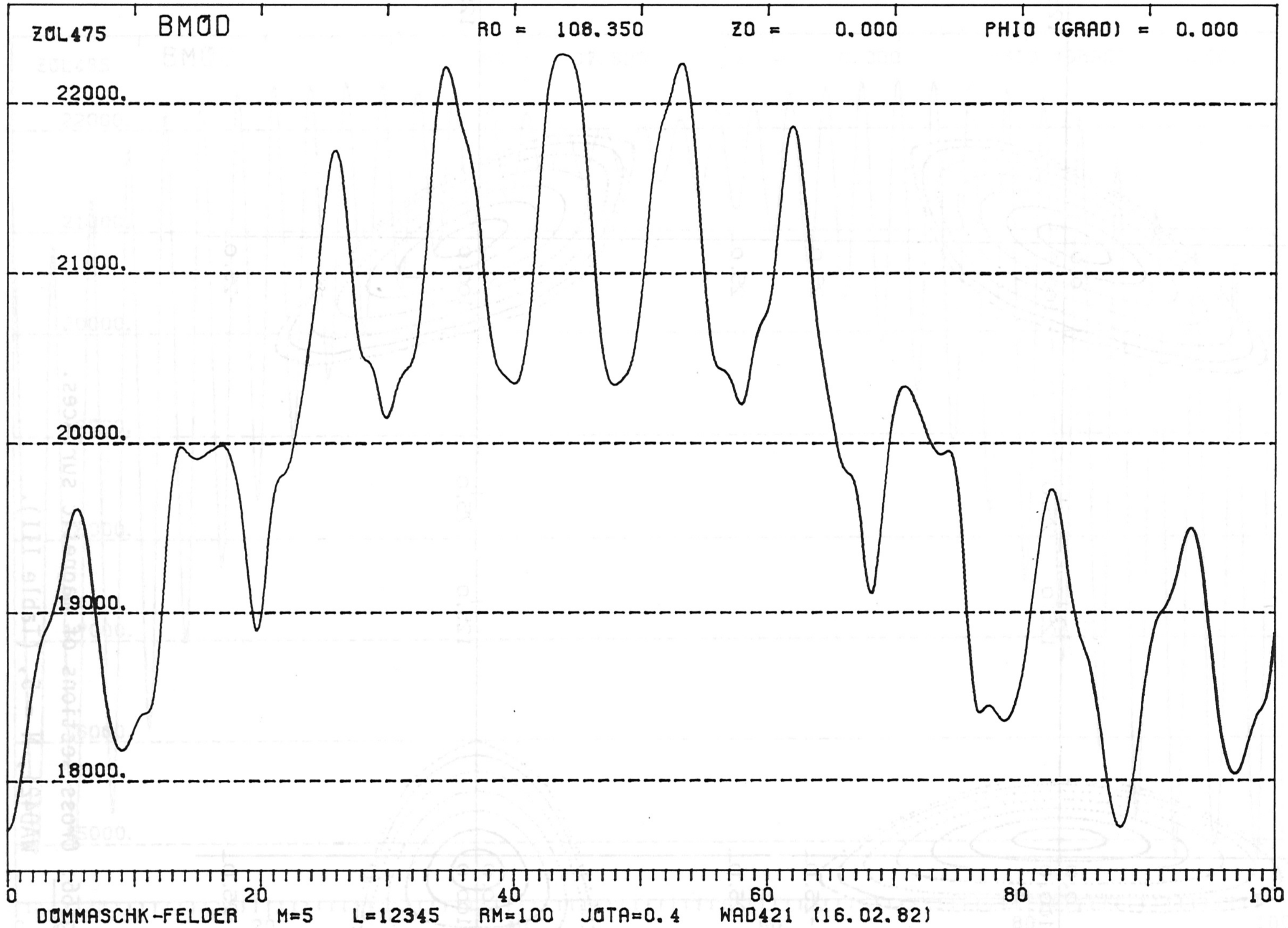

Fig.67: Magnitude of magnetic field along a field line.
WAD421, N = 5, A = 10, ι = 0.45.

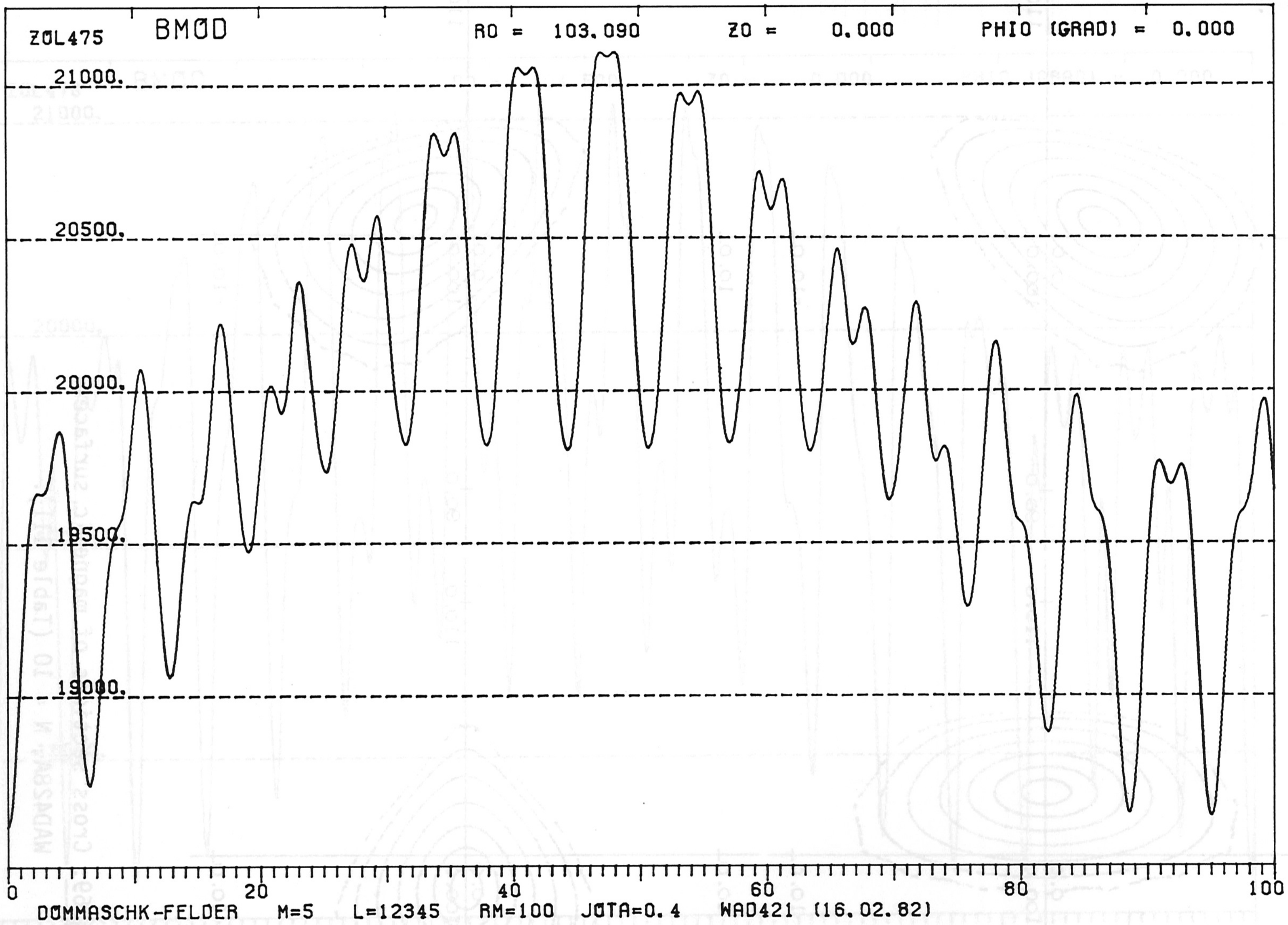

Fig.68: Magnitude of magneitc field along a field line.

WAD421, N = 5, A = 20, ι = 0.34.

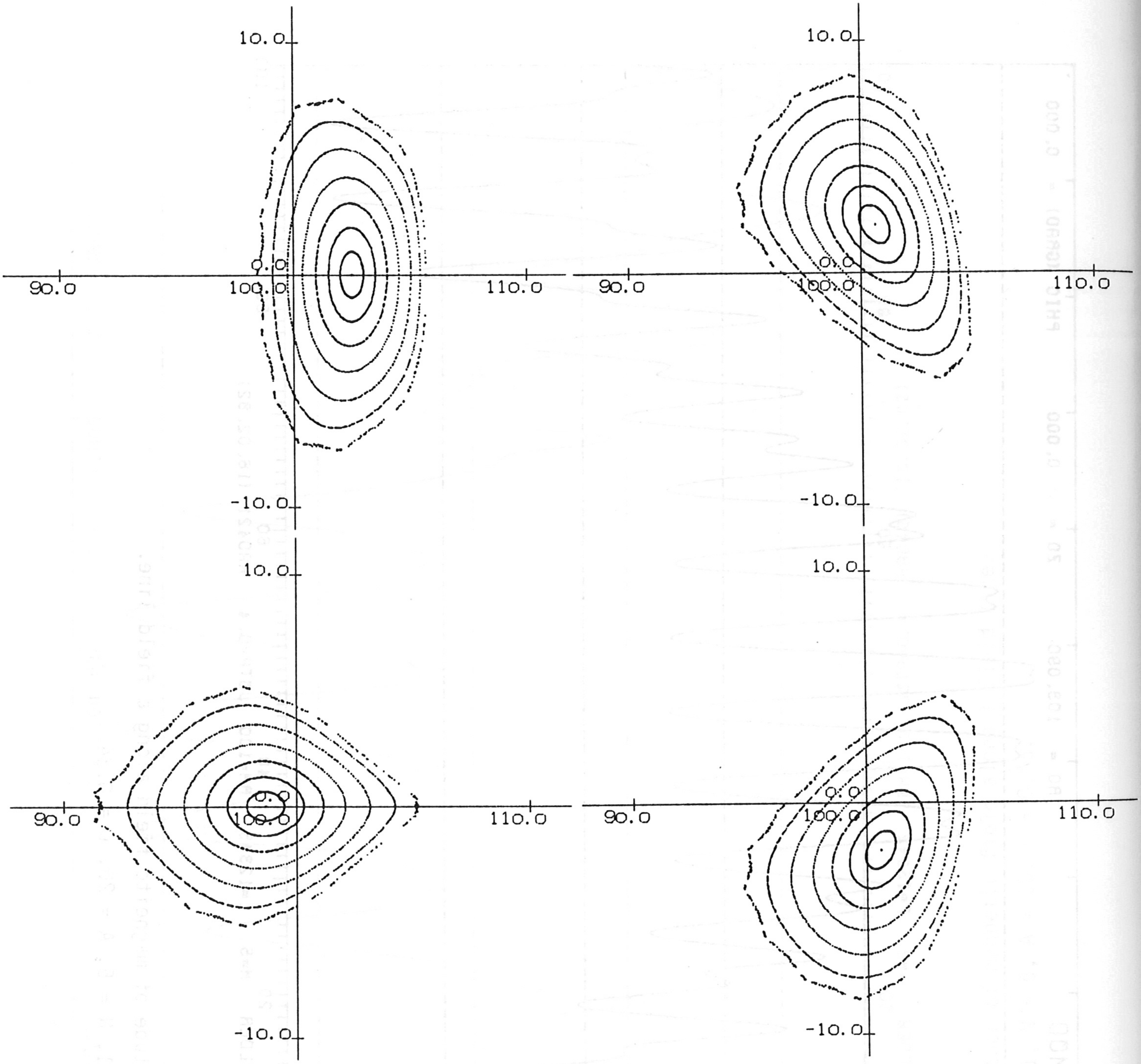

Fig.69: Cross sections of magnetic surfaces.
WAD428A, N = 10 (Table III).

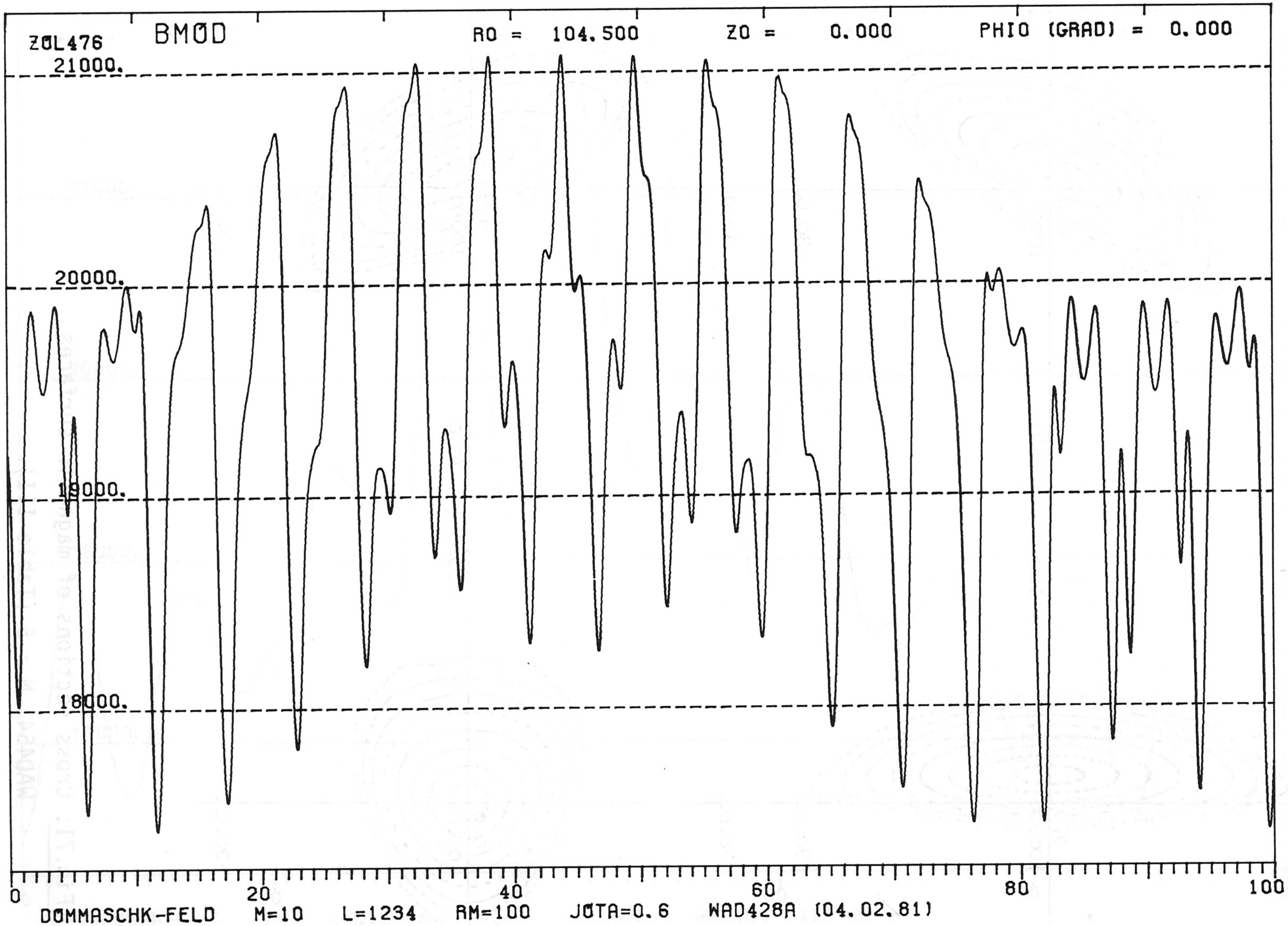

Fig.70: Magnitude of magnetic field along a field line.
WAD428A, N = 10, A = 33, ι = 0.61.

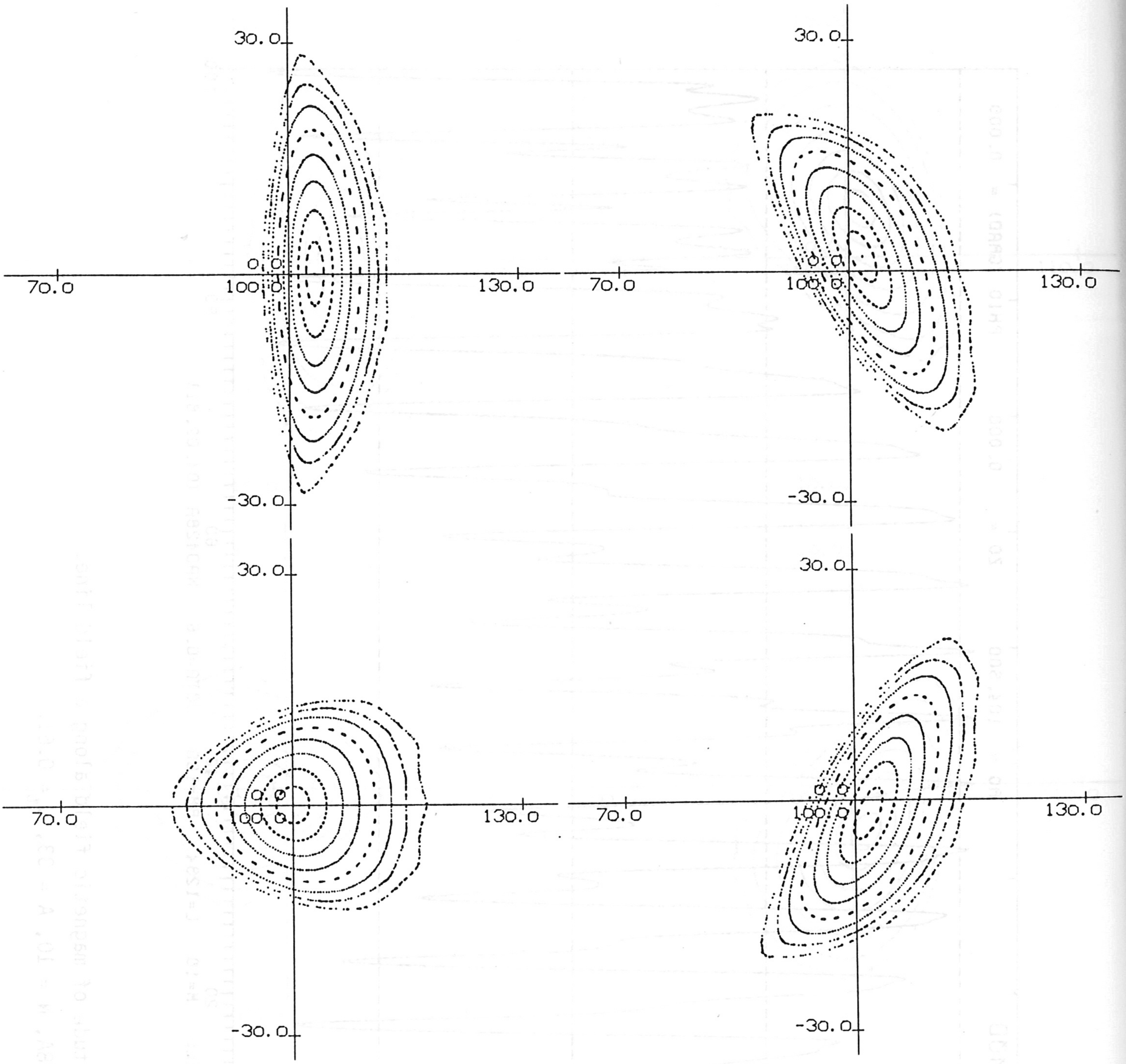

Fig.71: Cross sections of magnetic surfaces.
WAD454, N = 5 (Table III).

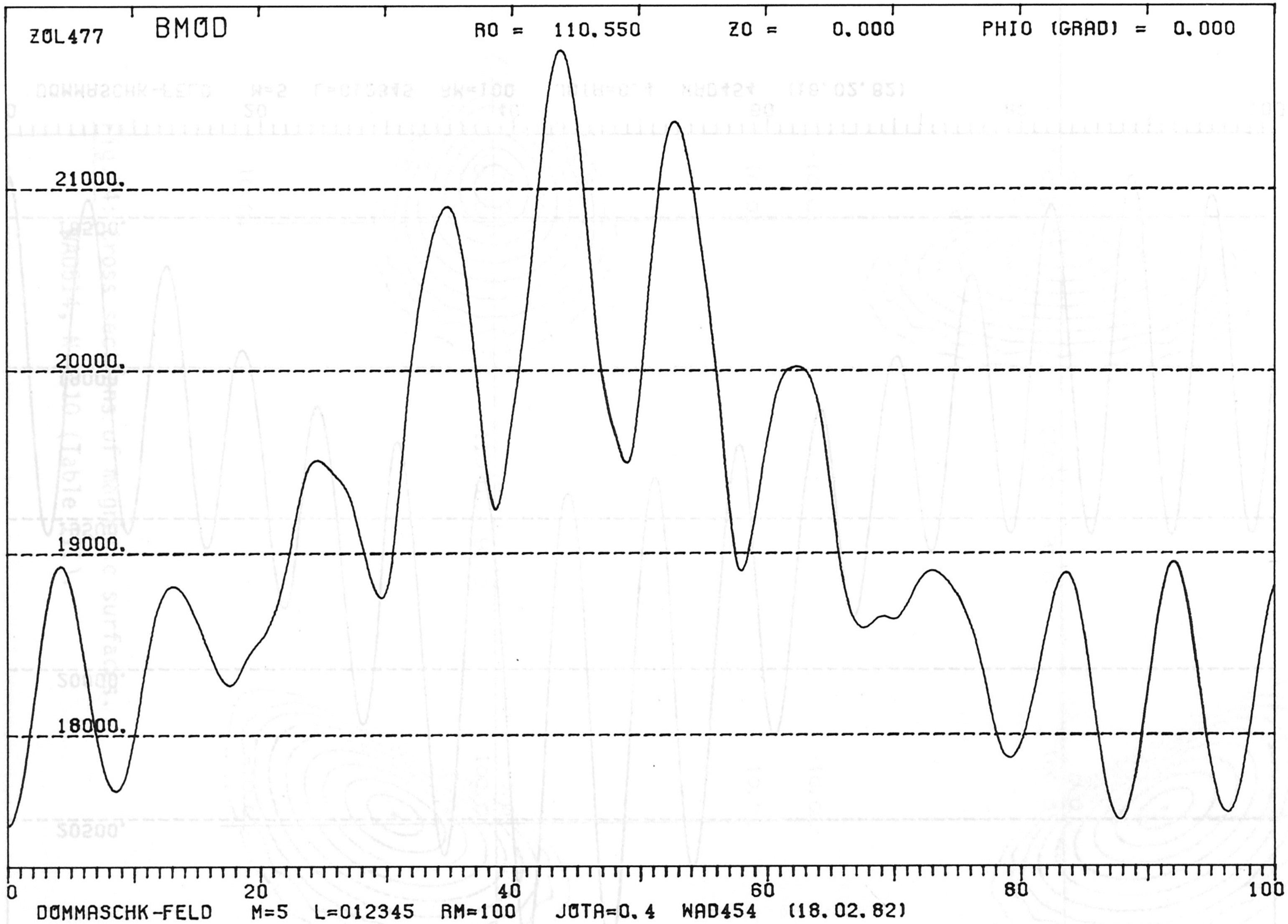

Fig.72: Magnitude of magnetic field along a field line.
WAD454, N = 5, A = 10, ι = 0.44.

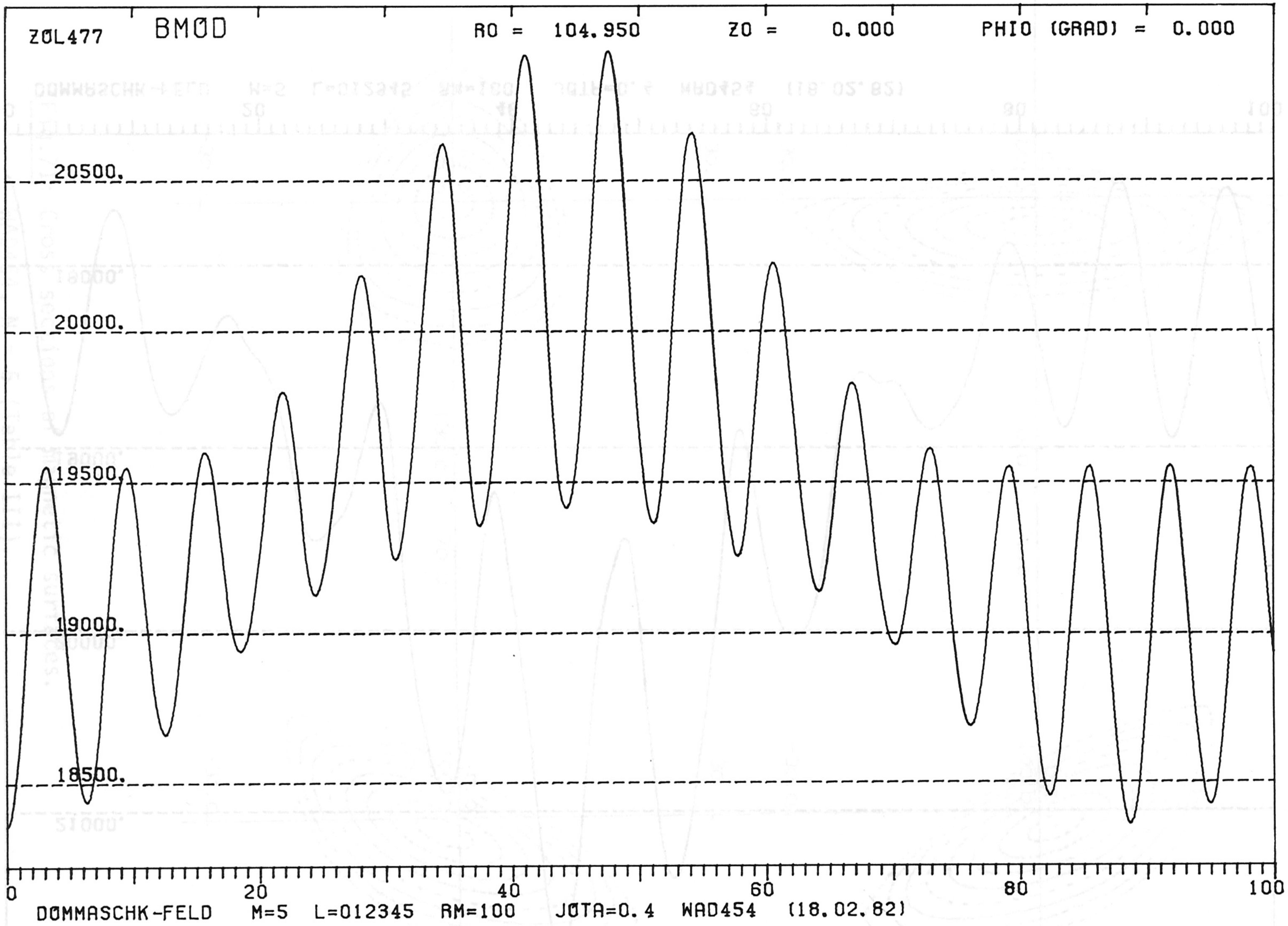

Fig.73: Magnitude of magnetic field along a field line.
WAD454, N = 5, A = 20, ι = 0.35.

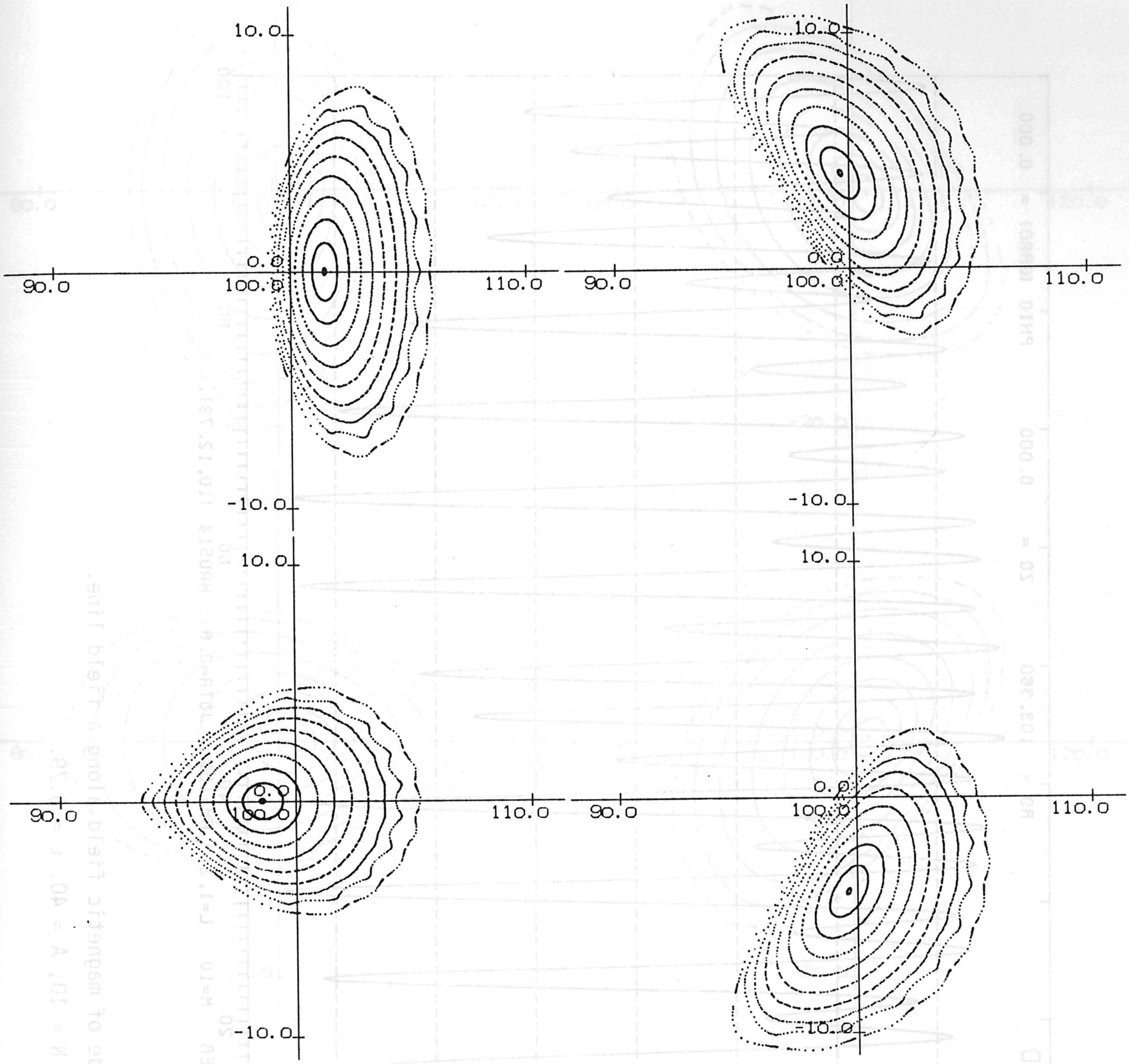

Fig.74: Cross sections of magnetic surfaces.
WAD514, N = 10 (Table III).

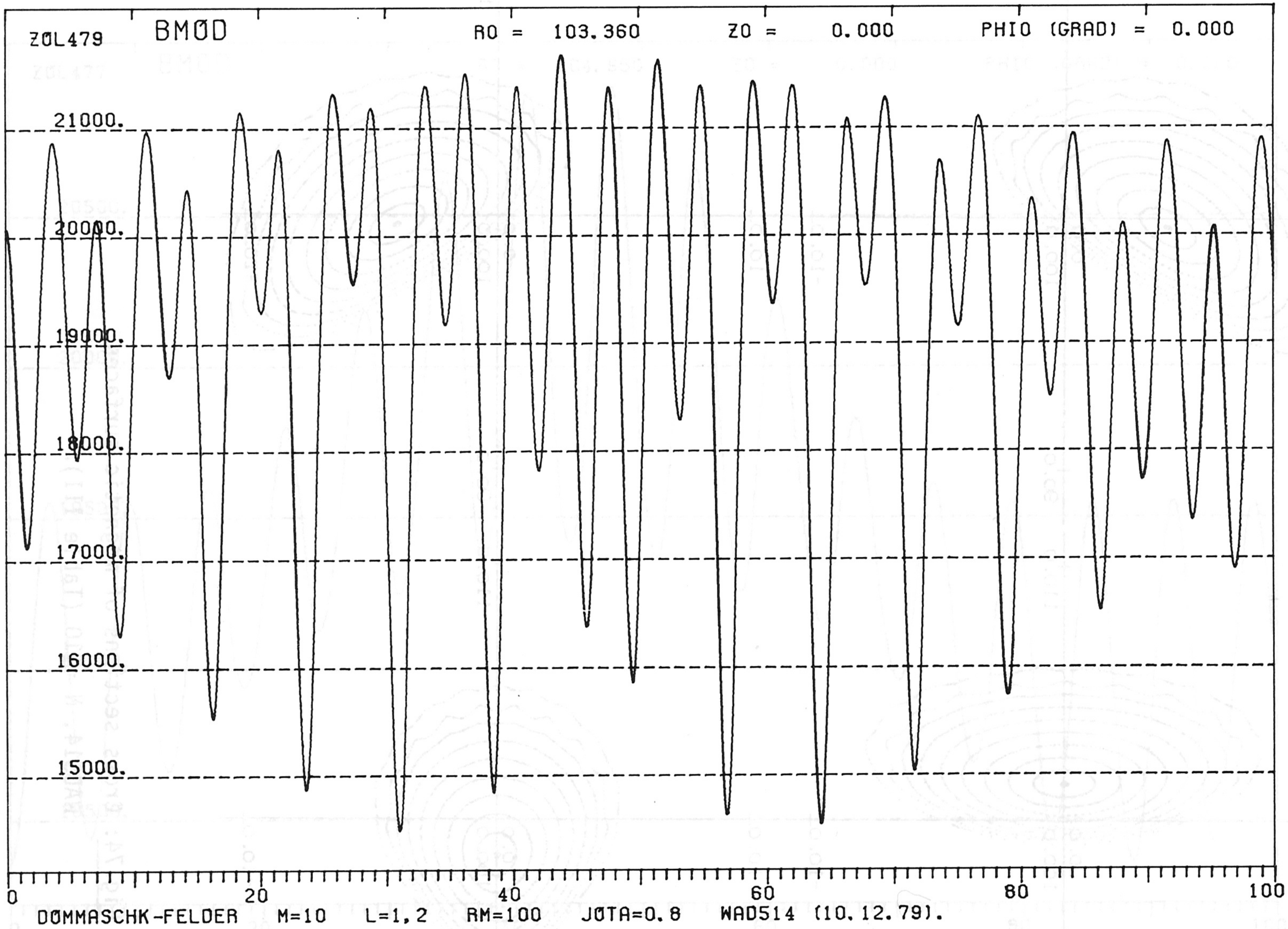

Fig.75: Magnitude of magnetic field along a field line.
WAD514, N = 10, A = 40, ι = 0.79.

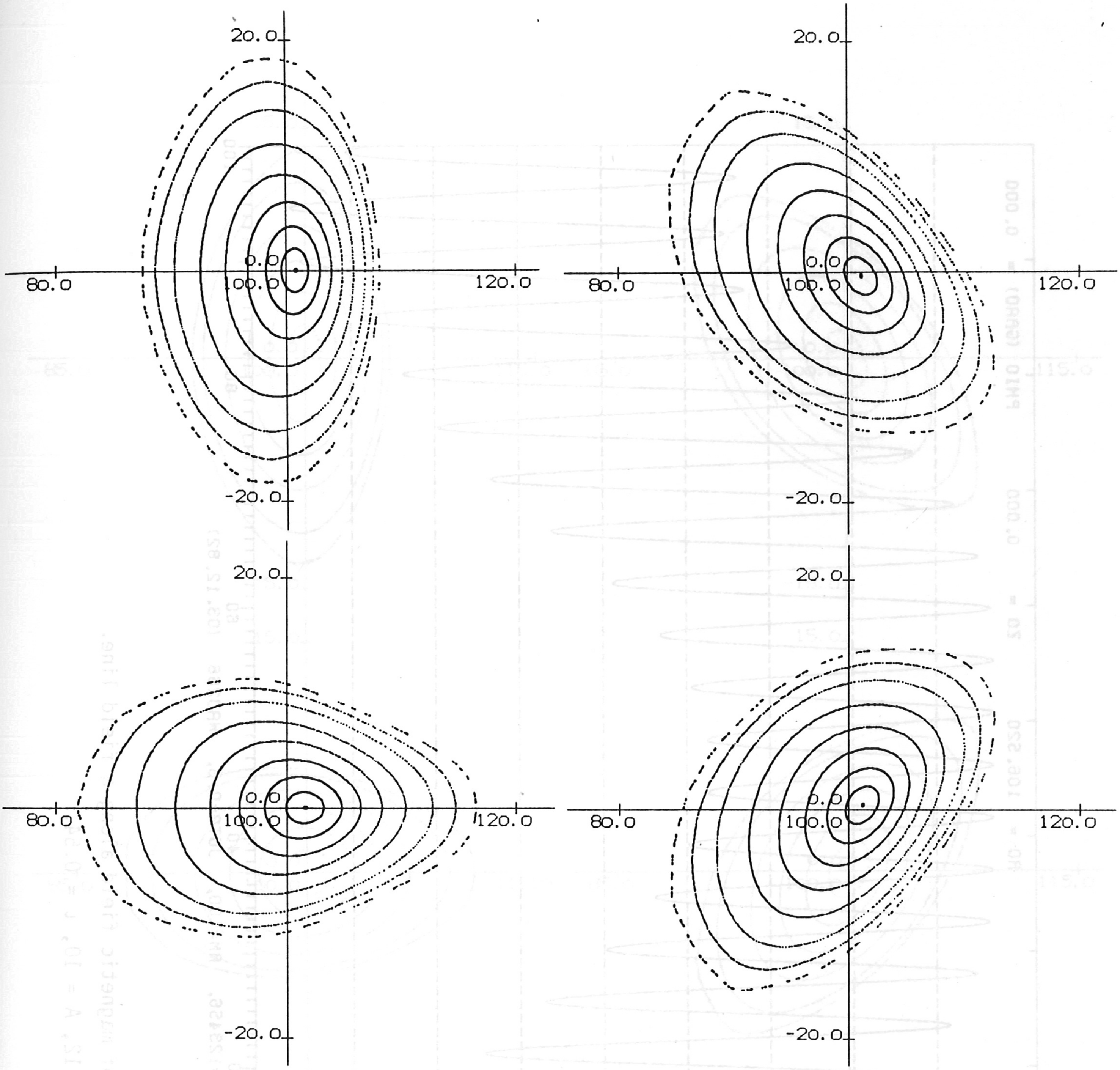

Fig.76: Cross sections of magnetic surfaces.
ATF-1, N = 12 (Table III).

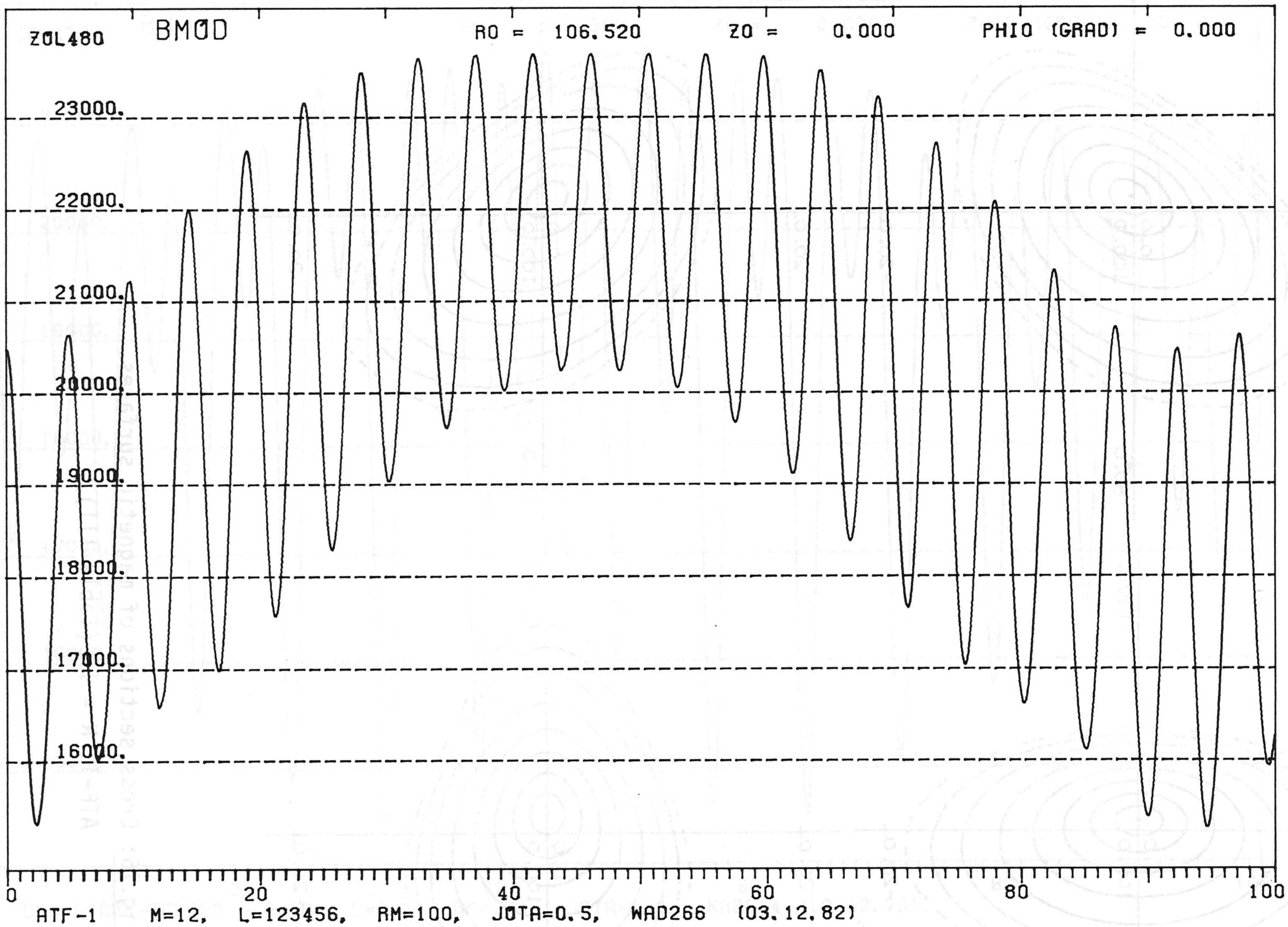

Fig.77: Magnitude of magnetic field along a field line.
ATF-1, N = 12, A = 10, $\iota = 0.54$.

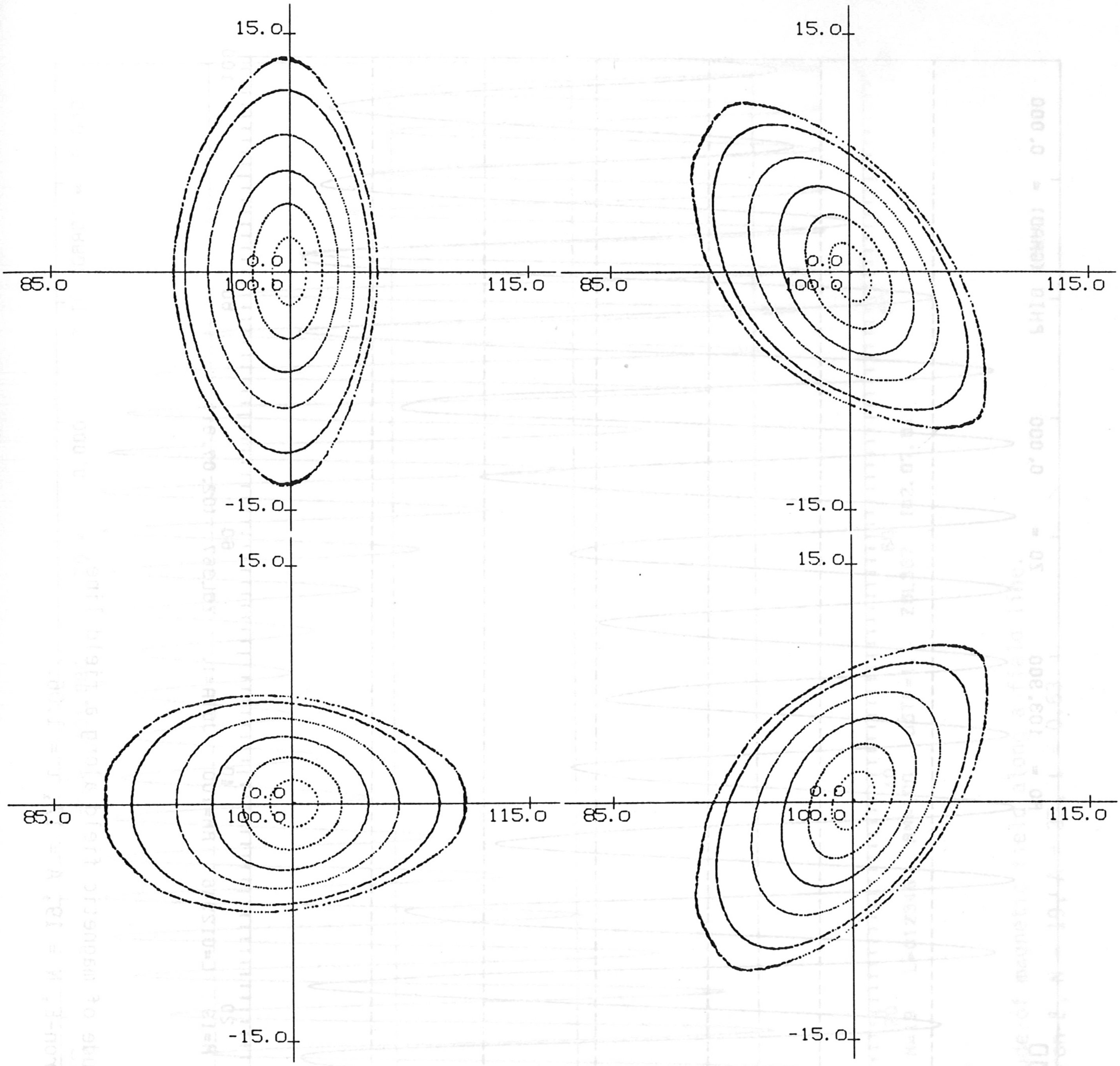

Fig.78: Cross sections of magnetic surfaces.
Heliotron-E, N = 19 (Table III).

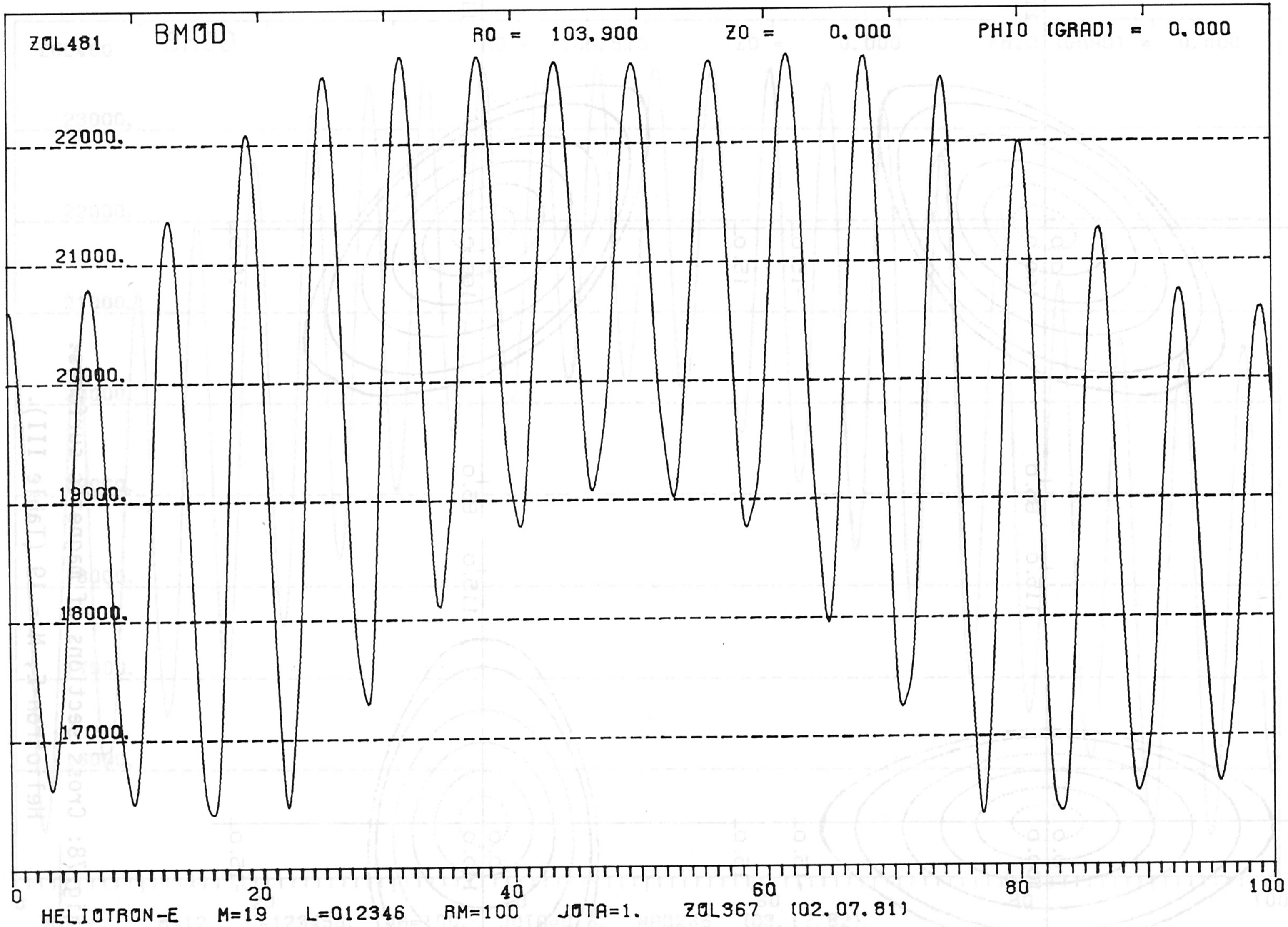

Fig.79: Magnitude of magnetic field along a field line.
Heliotron-E, N = 19, A = 17, ι = 1.06.

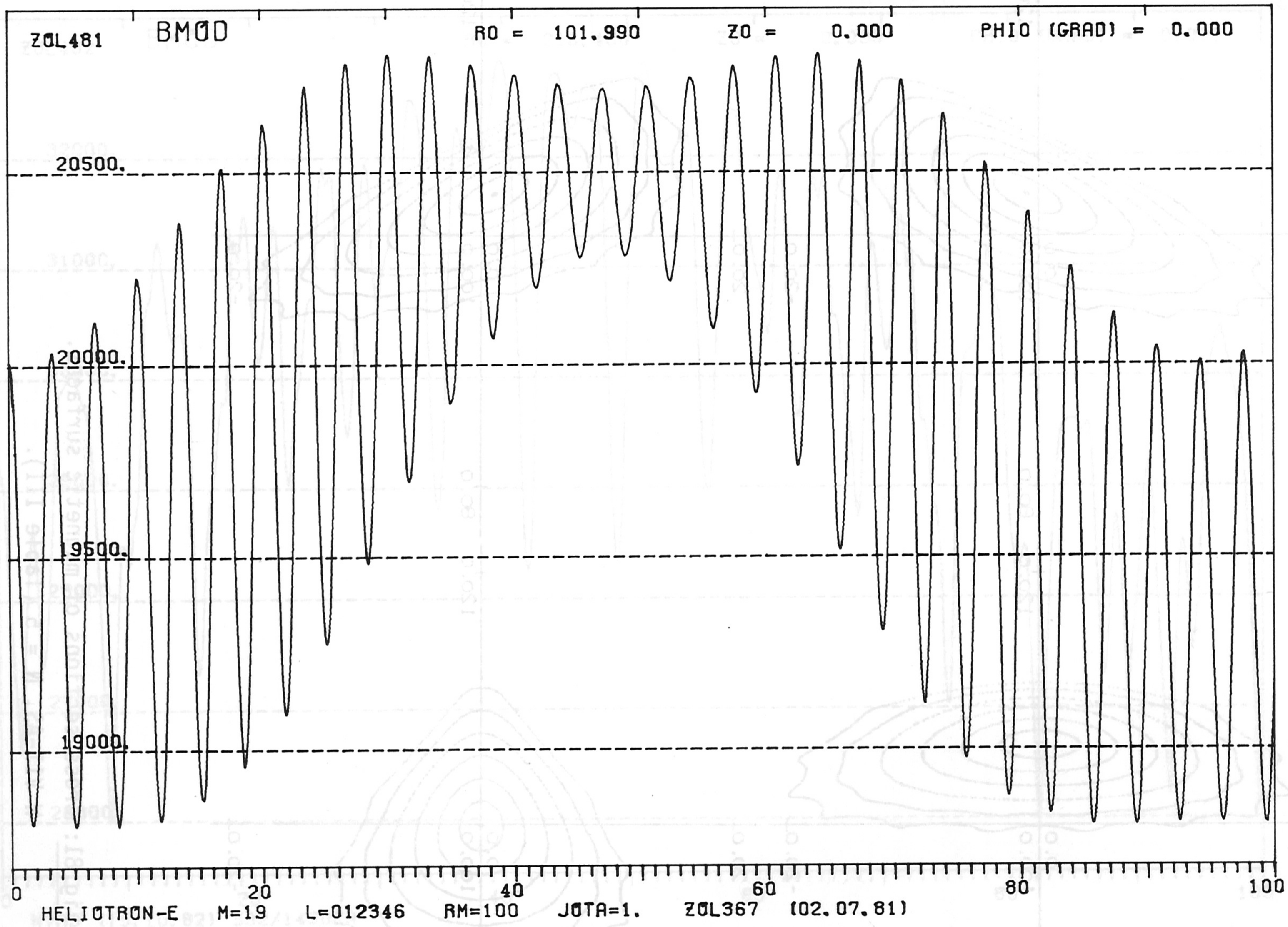

Fig.80: Magnitude of magnetic field along a field line.
Heliotron-E, N = 19, A = 33, ι = 0.63.

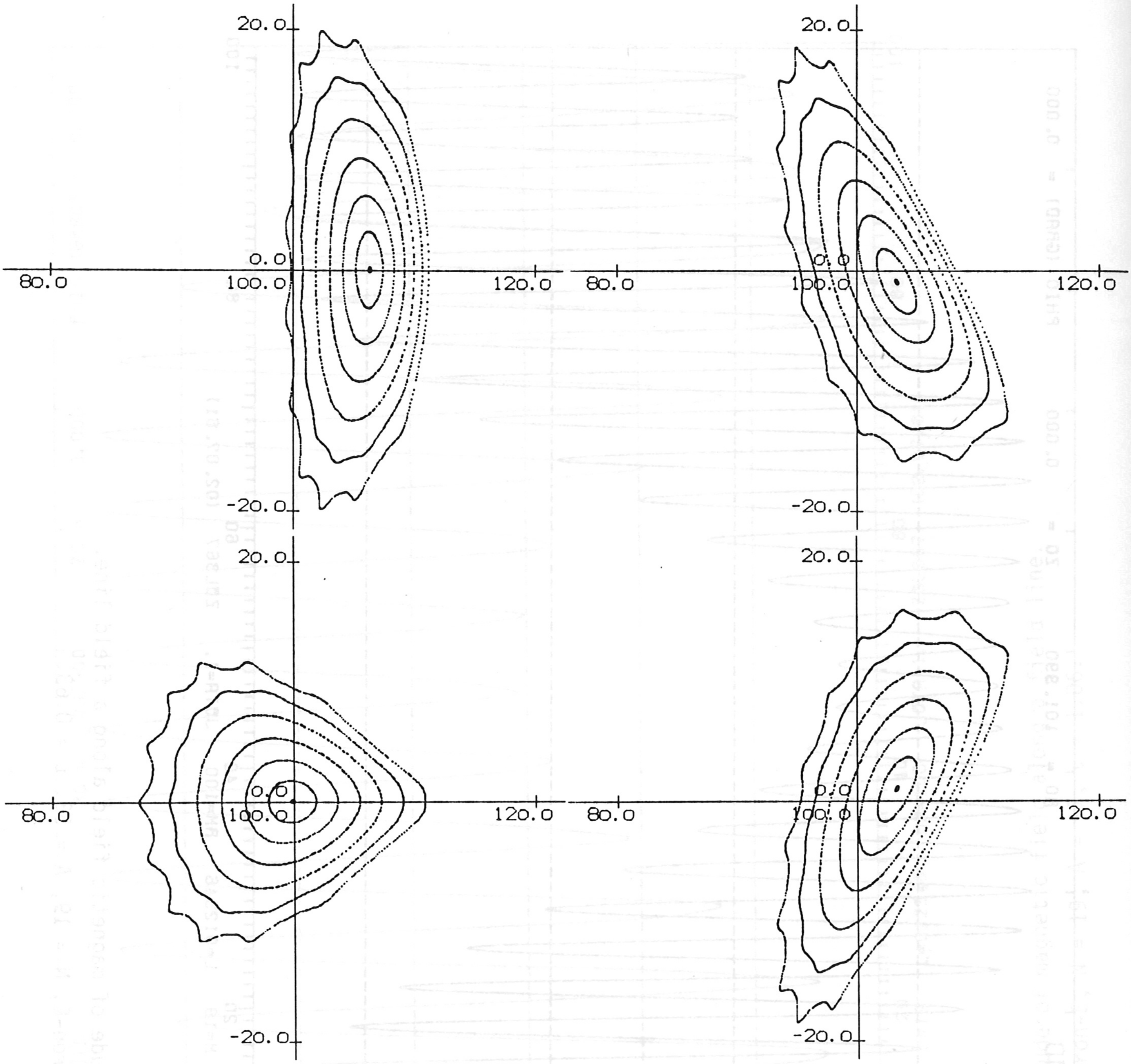

Fig.81: Cross sections of magnetic surfaces. W VII-AS, N = 5 (Table III).

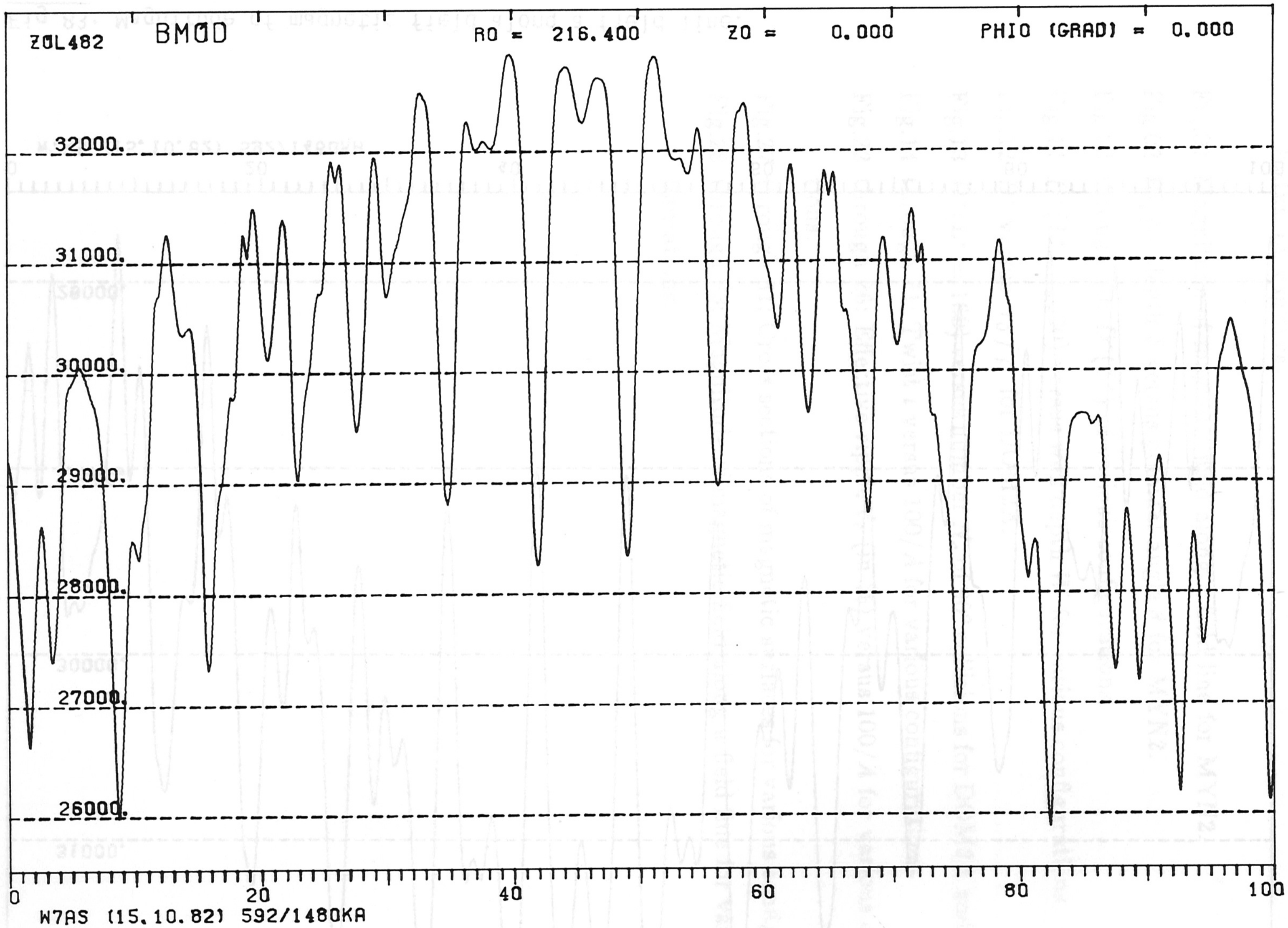

Fig.82: Magnitude of magnetic field along a field line.
W VII-AS, N = 5, A = 12, ι = 0.39.

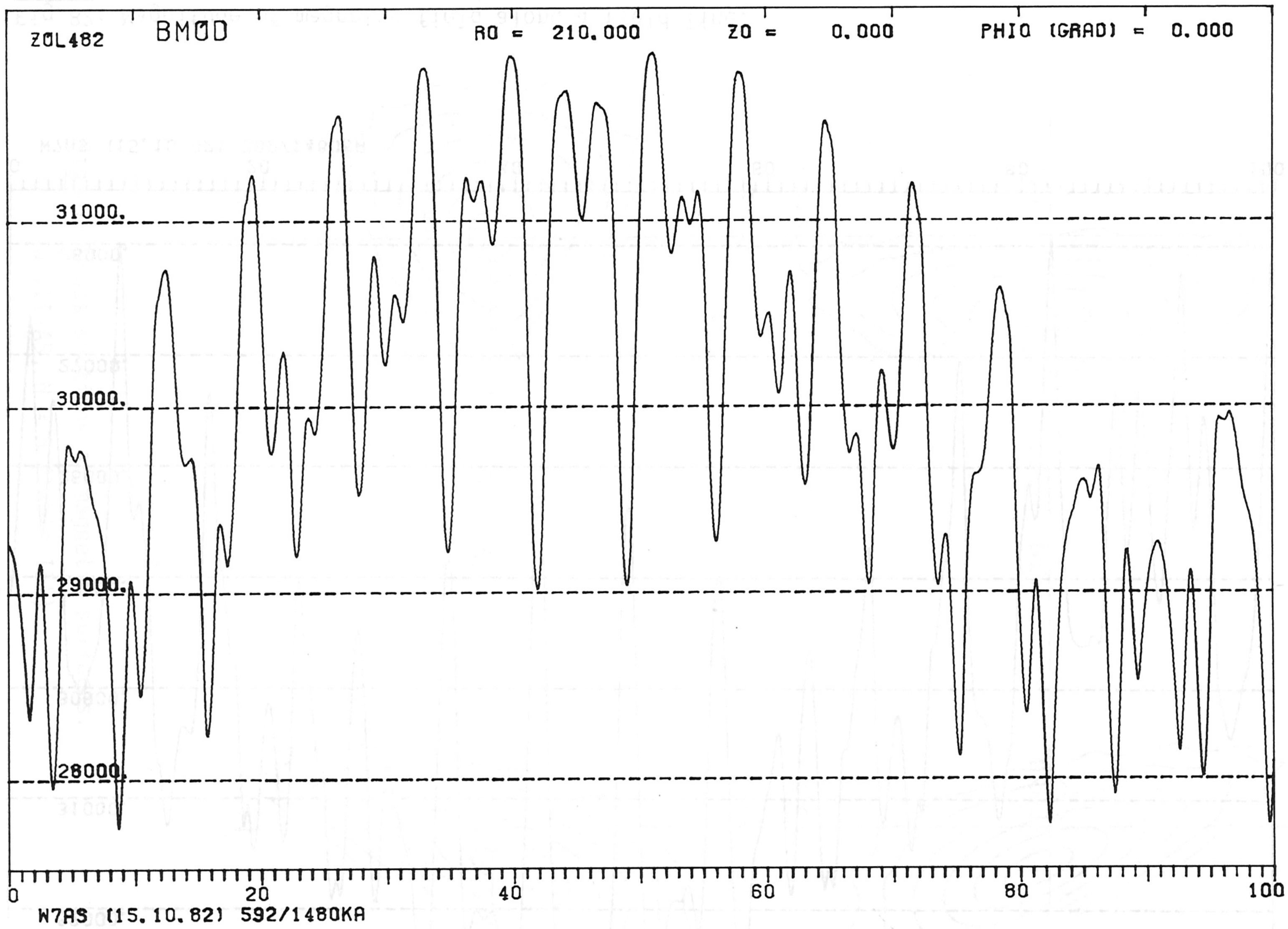

Fig.83: Magnitude of magnetic field along a field line.
W VII-AS, N = 5, A = 20, ι = 0.39.

Index of Figures.

Cross Reference of Figures.

Configuration	Figure Numbers
DOM19	6, 16, 22, 43, 44
DOM19A	16, 45, 46
DOM2A	3, 4, 5, 6, 11, 12, 13, 14, 22, 27, 28
DOM2B	4, 14, 29, 30
DOM2C	4, 14, 31, 32
DOM2D	5, 14, 33, 34
DOM2E	5, 14, 35, 36
DOM25	6, 9, 11, 13, 15, 22, 37, 38
DOM25A	15, 39, 40
DOM25B	15, 41, 42
DOM3	17, 47, 48, 49
DOM3A	17, 50, 51, 52
DOM3B	17, 53, 54, 55
ASC742	8, 18, 23, 56, 57
CHU2	8, 18, 23, 58, 59
MYN2	1, 2, 8, 18, 23, 60, 61
WAD384	7, 19, 24, 62, 63
WAD409	11, 20, 25, 64, 65
WAD421	9, 11, 20, 25, 66, 67, 68
WAD428A	7, 19, 24, 69, 70
WAD454	9, 11, 20, 25, 71, 72, 73
WAD514	7, 19, 24, 74, 75
ATF-1	10, 11, 21, 26, 76, 77
Heliotron-E	10, 11, 21, 26, 78, 79, 80
W VII-AS	10, 11, 21, 26, 81, 82, 83